UNIVERSITY OF CALIFORNIA
RIVERSIDE

Synthesis, Characterization and Electrocatalytic Performance of Bulk Transition Metal Borides

A Dissertation submitted in partial satisfaction
of the requirements for the degree of

Doctor of Philosophy

in

Chemical and Environmental Engineering

by

Hyounmyung Park

September 2019

Dissertation Committee:
Dr. Boniface P. T. Fokwa, Chairperson
Dr. Juchen Guo
Dr. Ruoxue Yan

The Dissertation of Hyounmyung Park is approved:

_____

_____

_____

Committee Chairperson

University of California, Riverside

ACKNOWLEDGEMENTS

First and foremost, I would like to express my sincere gratitude to my advisor, Dr. Boniface Fokwa. He welcomed me into his group with open arms. Thank you for your continuous support, encouragement and advice during my Ph.D. studies at University of California, Riverside. His kind and careful guidance and mentorship helped me enormously improving my Ph.D. research. Whenever I was down about my research progress or stuck at a bottleneck, he would encourage and motivate me to move forward. I would not have been able to complete this dissertation without his help and support.

I would like to thank my Ph.D committee members, Dr. Juchen Guo and Dr. Ruoxue Yan for taking the time to consider this work. This dissertation could be improved by their meaningful comment and constructive feedback based on their expertise. I really appreciate their help.

I would love to sincerely thank my lovely wife, Bo Kyung Ko. Since we had our adorable daughter, Jiyoo Park, she not only supported my studies but also took care of our baby. I feel very lucky to have such a beautiful and wonderful wife for my life. Every time when I had difficulty during my research, she consoled me and gave me the energy to overcome my burdens. Without her support, my Ph.D. absolutely could not have been possible. Thank you, and I love you with all my heart. I would also like to thank to my two babies: Jiyoo and Jio. Jiyoo was my big motivator with her sole presence, and Jio is our newest addition to the family and will be delivered soon. I am excited to meet you and thank you for coming to me and my wife.

Finally, I would like to thank my group members, past and present - especially Pritam Shankhari and Jan Scheifers. We were lab mates from the beginning and spent lots of time setting up the lab together from installation to repair of our instruments. Without their help, I would not have been able to complete my Ph.D. study. I sincerely wish them good luck for their future career and life endeavors.

COPYRIGHT ACKNOWLEDGEMENTS

DFT calculation was conducted by Dr. Yuemei Zhang.

ABSTRACT OF THE DISSERTATION

Synthesis, Characterization and Electrocatalytic Performance of Bulk Transition Metal Borides

by

Hyounmyung Park

Doctor of Philosophy, Graduate Program in Chemical and Environmental Engineering
University of California, Riverside, September 2019
Dr. Boniface P. T. Fokwa, Chairperson

Hydrogen is considered a promising alternative to carbon-based fuels as it is a clean, renewable and abundant energy source. In recent years, hydrogen evolution reaction (HER) via electrochemical water splitting has received a great deal of attention as a clean and efficient technique to produce hydrogen. A few precious metals such as platinum (Pt) have exhibited state-of-the-art electrocatalytic activity for HER with much low overpotential, but their high cost and lack of abundance limit their application industrially. Thus, HER electrocatalysts that are both highly active and economical are in high demand in order to reduce the overpotential while maintaining low cost.

Recently, transition metal borides (TMBs) have been considered as potential alternatives to noble metals as HER electrocatalysts due to their abundance, low cost and excellent activity and stability for HER. Chapter 2 discusses synthesis of four binary bulk molybdenum borides (Mo_2B, α-MoB, β-MoB and α-MoB_2) by arc-melting. HER activity measured for all four phases in acidic condition increased with the amount of boron. In

Chapter 3, tin flux synthesis of β-MoB_2, which has the same boron content as α-MoB_2 but different structure, is discussed. Two different boron layers, flat (graphene-like) and puckered (phosphorene-like) boron layers, were found in β-MoB_2. the two boron layers showed significantly different HER activity, which was supported by the Gibbs free energy calculations of H-adsorption. In Chapter 4, tungsten-based boride HER electrocatalyst was studied experimentally and theoretically for the first time. Tungsten could be successfully substituted (up to 30 at.%) for molybdenum in α-MoB_2. The resulting α-$Mo_{1-x}W_xB_2$ presented better HER activity than binary phases of both WB_2 and MoB_2. DFT calculation revealed that graphene-like boron layer was the most active and that tungsten promoted hydrogen generation by facilitating bonding between hydrogen atoms. In addition, importance of working electrode preparation method was investigated. General drop-casting method worked well for nanosized particles, but it was not suitable for bulk samples. New method (i.e. grinding and polishing arc-melting sample to disc shape) has been devised, which led to better HER performance.

In Chapter 5, chromium-based boride HER electrocatalyst was investigated for the first time. Chromium-molybdenum diborides ($Cr_{1-x}Mo_xB_2$ (x = 0, 0.25, 0.4, 0.5, 0.6, 0.75), AlB_2-type) were successfully synthesized using solid solution synthesis. $Cr_{1-x}Mo_xB_2$ catalysts exhibited much higher HER activity than binary phases of CrB_2 and MoB_2. Among Cr-Mo-B electrocatalysts, $Cr_{0.4}Mo_{0.6}B_2$ presented the highest HER activity and even outperformed Pt/C HER activity at high current density (about 500 mA/cm^2).

Table of Contents

List of Figures

List of Tables

Chapter 1.

Introduction

1.1. Introduction

In recent years, there has been an increasing demand on renewable energy as an alternative to fossil fuels due to the depletion of fossil fuels as well as the environmental consequences such as global warming and climate change. [1-2] Hydrogen has been considered as one of the most promising alternatives to fossil fuels because it is clean, renewable and has a high energy density. [3-5]

Coal gasification is a low-cost method that produces plenty of hydrogen. However, this method emits CO_2 as a by-product, which is a major cause of global warming. [6] The most advanced green method to produce hydrogen is the electrochemical water splitting into hydrogen and oxygen. [7-9] Electrochemical water splitting includes two half-reactions: hydrogen evolution reaction (HER: $4H^+ + 4e^- \rightarrow 2H_2$) at the cathode and oxygen evolution reaction (OER: $2H_2O \rightarrow O_2 + 4H^+ + 4e^-$) at the anode. However, water splitting is not a favorable process due to its thermodynamic barrier. [10-11] Therefore, it is essential to develop electrocatalysts that can effectively facilitate the sluggish kinetic process for HER and OER. [12-13] Up to now, platinum group metals and noble metal oxides (e.g. RuO_2, IrO_2) are considered as state-of-the-art HER and OER electrocatalyst, respectively. Unfortunately, the low abundance and high cost of these precious metals limit their large-scale application. [14-15] Therefore, highly active and economical non-noble-metal electrocatalysts with low overpotential, high current density, and long-term stability must be developed. Recently, tremendous efforts have been made to discovering noble metal-free HER electrocatalysts

with low cost and high activity. Transition metal compounds, including phosphides[16-18], nitrides[19-21], sulfides[22-23] and carbides[24-26] have been studied to exhibit outstanding HER electrocatalytic activity and stability.

While the aforementioned materials have been investigated extensively until now, transition metal borides (TMBs) such as Mo-B (bulk, nanoscale)[27-31], FeB_2 (nanoscale)[32], VB_2 (nanoscale)[33], Co-B (amorphous)[34], Ni-B (amorphous)[35], Co-Ni-B (amorphous)[36], and MoAlB (bulk)[37] have attracted considerable attention recently, due to their low cost, excellent electrocatalytic HER activity and stability in both acidic and basic solution. However, despite the superb electrocatalytic properties, this class of TMB materials is rarely studied as counterparts to other transition metal compounds mainly due to high temperature and difficult synthesis, especially if crystallinity is required. Thus, most studies on TMBs electrocatalysts have focused on amorphous phases. [38-39]

In this work, crystalline binary and ternary phases of transition metal borides were synthesized and characterized for their structures and electrocatalytic properties.

1.2. Hydrogen evolution reaction (HER)

As shown in **Figure 1.1**, the water electrolysis system generally has three components: an electrolyte, a cathode and an anode. When external voltage is applied to the electrode, the hydrogen ions move toward the cathode, while the hydroxide ions move towards the anode. Finally, water molecules decompose into hydrogen and oxygen. Therefore, the water splitting reaction can be divided into two half-reactions: oxygen evolution reaction (OER) and hydrogen evolution reaction (HER). [40]

HER is a multi-step cathodic reaction taking place on the surface of electrode. Generally accepted HER mechanisms in acid and alkaline media are presented in **Figure 1.1b and c**: [41]

1) Volmer reaction (electrochemical hydrogen adsorption)

$H^+ + e^- \rightarrow H_{ads}$ (acid)

$H_2O + e^- \rightarrow H_{ads} + OH^-$ (alkaline)

followed by

2) Tafel reaction (chemical desorption)

$2H_{ads} \rightarrow H_2$ (both acid and alkaline)

or

3) Heyrovsky reaction (electrochemical desorption)

$H_{ads} + H^+ + e^- \rightarrow H_2$ (acid)

$H_{ads} + H_2O + e^- \rightarrow H_2 + OH^-$ (alkaline)

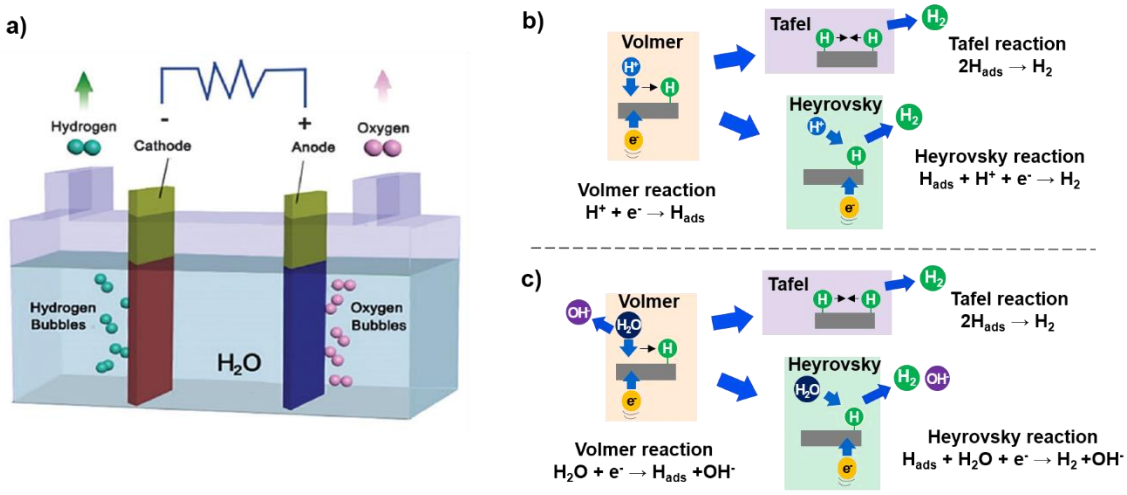

Figure 1.1. a) general water electrolysis system, HER mechanism in b) acid and c) alkaline solution. [40]

The Tafel slope is normally utilized to determine the possible HER reaction pathway and the rate-determining step (RDS), and it can be calculated by linear portion of fitted Tafel equation ($\eta = b \cdot log\, j + a$, where b is the Tafel slope, η is overpotential, j is current density). In general, the Tafel slopes of Volmer, Heyrovsky and Tafel reaction are 120, 40, and 30 mV/dec. at room temperature, respectively. [42]

The Gibbs free energy for hydrogen adsorption (ΔG_H) is widely used as a descriptor for a hydrogen-evolving material. If ΔG_H is largely negative ($\Delta G_H < 0$), the H_{ads} is bound strongly with the electrode surface, easily facilitating the initial Volmer reaction, but the subsequent Tafel or Heyrovsky reaction is difficult. If ΔG_H is largely positive ($\Delta G_H > 0$), on the other hand, H_{ads} has a weak interaction with the electrode surface, leading to a slow Volmer reaction that limits the overall turnover rate. Therefore, ΔG_H should be about zero: not too weak to be able to activate the reactant, and not too strong to be able to desorb the products. For example, Pt, known as the best HER catalyst, has approximately zero ΔG_H (**Figure 1.2**). Thus, non-noble metal HER catalyst should have an appropriate surface property with showing near zero ΔG_H. [40]

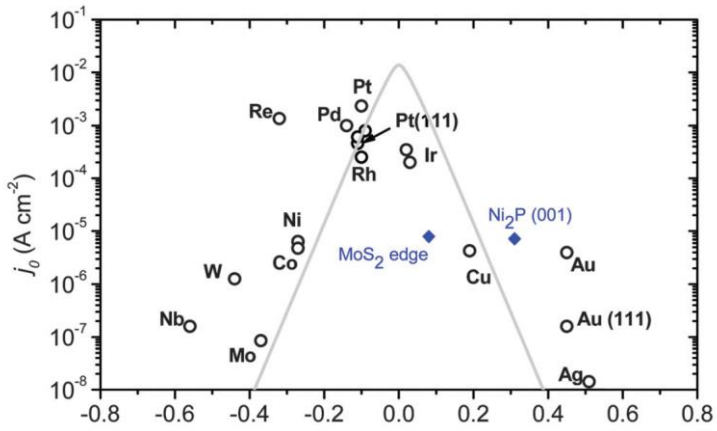

Figure 1.2. A volcano plot of experimentally measured exchange current density as a function of the DFT-calculated Gibbs free energy of adsorbed atomic hydrogen.[42]

Thermodynamic voltage of water splitting is 1.23 V at 25 ℃ and 1 atm regardless of electrolyte; it is temperature-dependent andS can be reduced by increasing electrolyte temperature. However, voltage higher than the thermodynamic voltage should be applied to conduct electrochemical water splitting due to the excess potential (overpotential, η). The overpotential is needed to overcome the intrinsic activation barriers present on both anode (η_a) and cathode (η_c), as well as other resistances (η_{other}), such as solution resistance and contact resistance. Thus, the operational voltage (E_{op}) for water splitting can be described as: [9, 40]

$$E_{op} = 1.23\,V + \eta_a + \eta_c + \eta_{other}$$

E_{op} could be decreased by reduction of overpotential to make the water electrolysis reaction energy efficient. Indeed, η_{other} can be reduced by optimizing the design of the electrolytic cell, whereas η_a and η_c should be minimized by highly active and efficient oxygen and hydrogen evolution reaction electrocatalyst, respectively. [40]

Therefore, developing of non-noble metal HER catalyst is desirable to improve energy efficiency and make the overall water splitting more economical.

1.3. Transition metal borides

Transition metal borides (TMBs) constitute a very large group of compounds composed of boron and metallic elements. TMBs can be classified in two groups; metal-rich and boron-rich borides. If the boron to metal ratio is 2:1 or higher than that, the phase is called boron-rich and if it is less, then it is called metal-rich boride.

Typical physical properties of borides are high melting points, high hardness, low thermal conductivities.[43-45] In addition to those properties, borides have chemical inertness, magnetic, electrical and catalytic properties. [46]

TMBs have many types of crystal structure for different metal to boron ratios. Metal-rich borides have composition of M_4B, M_3B (e.g., Re_3B), M_5B_2, M_7B_3, M_2B (e.g., Cr_2B, Mo_2B and W_2B) structures where boron atoms do not form any boron network. The dumbbell shaped isolated boron pairs are observed in in M_5B_3 (e.g., Cr_5B_3) and M_3B_2 (e.g., Nb_3B_2 and V_3B_2). As boron content increases, one-dimensional boron chains are formed. The zigzag chains (MB; e.g., MoB, WB, CrB and NbB) and double chains (M_3B_4; e.g., Ta_3B_4, Nb_3B_4, and V_3B_4) are observed. [47]

In the boron-rich metal borides with M:B $\approx$ 2, hexagonally ordered boron layers are formed. Those boron structure contain two types of boron layers: a flat graphene- and a corrugated phosphorene-like boron layer. α-MoB_2, CrB_2, NbB_2, and VB_2 have only flat

graphene-like boron layers and β-MoB_2 and β-WB_2 show both flat- and corrugated- boron layer. In ReB_2, all the boron layers are corrugated. [47-48]

The boron atoms exhibit various arrangement such as 1D chains to 2D sheets to 3D networks (**Figure 1.3**) and TMBs can have diverse properties based on different crystal structure. [49] For example, permanent magnets ($Nd_2Fe_{14}B$)[50], superconductors (MgB_2)[51-52], hard and high-temperature materials (TiB_2, ZrB_2)[48].

Recently, TMBs have attracted attention and been studied as electrocatalyst for HER due to their low cost, excellent stability in both acidic and basic solution.

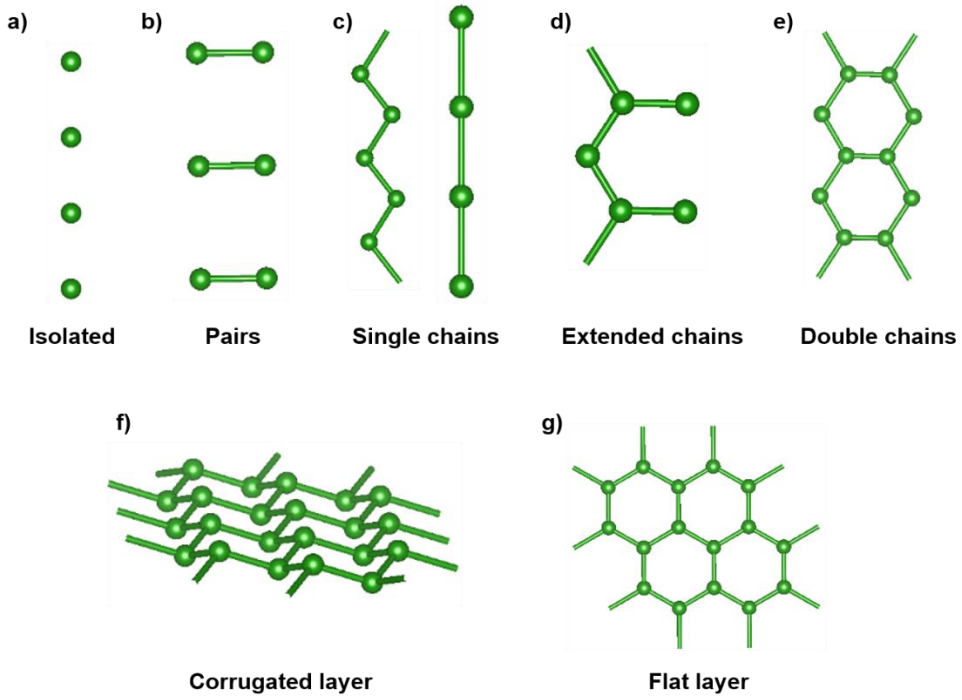

Figure 1.3. Different boron atom structures in TMBs: a) isolated boron atoms, b) pairs of boron atoms, c) single chains, d) extended chains, e) double chains, f) corrugated layer, g) flat layer.[48]

1.4. Synthesis method

Refractory compounds (e.g. transition metals carbides and borides) exhibit outstanding physical, chemical and mechanical properties. They are characterized by high melting points, corrosion resistance, hardness and stability of their electro-physical and mechanical properties in a wide temperature range. Therefore, it is necessary to synthesize single phases with low impurity content.

Arc melting

For producing polycrystalline TMBs, arc melting is an appropriate and widely used method in solid state chemistry for high temperature experiments. Very high temperature higher than 3000 ℃ is generated in a few seconds through electric arcs and the energy is directly heating the reactants. It is an efficient, practical and powerful synthesis technique when high temperatures are required for metallic substances.

Today, several laboratory-scale commercial arc-melting furnaces are available. All these instruments have water-cooled copper crucible for samples. The furnaces are operated with a tungsten electrode under argon atmosphere, and the Schlenk line (vacuum-argon gas) is equipped. Since most metals would react with oxygen in the arc, the purity of the argon gas in the sample chamber is important. The setup of an arc-melting furnace is shown in **Figure 1.4a**. Before melting, the sample chamber is evacuated and re-filled with purified argon. The power supply is connected to tungsten electrode and the power can be controlled by a foot pedal during the melting process. During the reaction, the chamber is flushed with

argon gas. The gas discharge is started by applying voltage between two electrodes forms a plasma, in which the argon atoms are partially ionized. [47]

High frequency induction furnace

The induction furnace can heat the conductive materials by electromagnetic induction without any contact. This method enables the synthesis of air sensitive materials in a vacuum or inert atmosphere. Induction melting is energy-efficient and easily controllable process and this technique allows to heat up tons in various metal industry. [53-54] A high-frequency alternating current is flowing through the copper coils surrounding the metallic samples. An eddy current is generated within the metallic samples and the materials resistance leads to Joule heating. In addition, the set point temperature can be controlled by the frequency. If the frequency of the alternating current increases, the applied power to furnace will increase as well. [47, 55] This technique is especially useful for growing single crystals such as Sc_{66}, Zr_{12}, and ReB_{12}.[48]

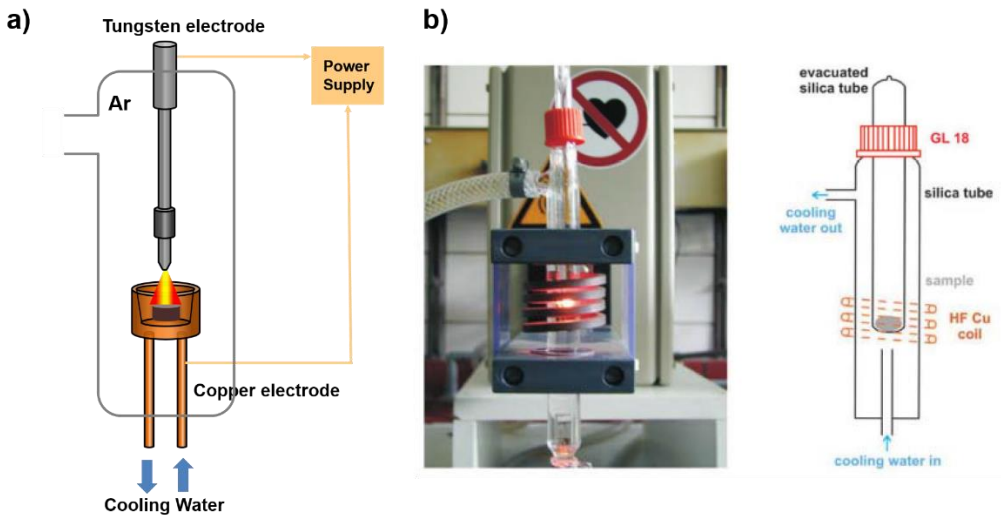

Figure 1.4. Scheme of a) laboratory-scale arc melting furnace and b) induction furnace. [55]

Metal-flux assisted synthesis

The metal flux method is an outstanding preparative technique for synthesis of new intermetallic materials and large single crystal can be grown by this method. [55] The molten metal flux can facilitate diffusion of the elements. [56] The metal as media should have the following properties: 1) the metal should form a flux at moderate temperature and have a large difference between its melting point and boiling point temperature, 2) it should be possible to separate from final products by mechanical removal or chemical dissolution, 3) it should not form stable binary compounds with any of reactants. Tin, aluminum, copper , gallium and cobalt are commonly used as flux metal in synthesis of TMBs. [57]

References

1. Chow, J.; Kopp, R. J.; Portney, P. R., *Science* **2003,** *302*, 1528.
2. Roger, I.; Shipman, M. A.; Symes, M. D., *Nature Reviews Chemistry* **2017,** *1*, 0003.
3. Turner, J. A., *Science* **2004,** *305*, 972.
4. Bonaccorso, F.; Colombo, L.; Yu, G.; Stoller, M.; Tozzini, V.; Ferrari, A. C.; Ruoff, R. S.; Pellegrini, V., *Science* **2015,** *347*, 1246501.
5. Xie, Z.; He, P.; Du, L.; Dong, F.; Dai, K.; Zhang, T., *Electrochim. Acta* **2013,** *88*, 390.
6. Edwards, P. P.; Kuznetsov, V. L.; David, W. I.; Brandon, N. P., *Energy policy* **2008,** *36*, 4356.
7. McCrory, C. C.; Jung, S.; Ferrer, I. M.; Chatman, S. M.; Peters, J. C.; Jaramillo, T. F., *J. Am. Chem. Soc.* **2015,** *137*, 4347.
8. Lewis, N. S.; Nocera, D. G., *Prog. Nat. Acad. Sci.* **2006,** *103*, 15729.
9. Cook, T. R.; Dogutan, D. K.; Reece, S. Y.; Surendranath, Y.; Teets, T. S.; Nocera, D. G., *Chem. Rev.* **2010,** *110*, 6474.
10. Li, X.; Han, G.-Q.; Liu, Y.-R.; Dong, B.; Shang, X.; Hu, W.-H.; Chai, Y.-M.; Liu, Y.-Q.; Liu, C.-G., *Electrochim. Acta* **2016,** *205*, 77.
11. Louie, M. W.; Bell, A. T., *J. Am. Chem. Soc.* **2013,** *135*, 12329.
12. Huang, T.; Chen, Y.; Lee, J. M., *Small* **2017,** *13*, 1702753.
13. Long, X.; Li, J.; Xiao, S.; Yan, K.; Wang, Z.; Chen, H.; Yang, S., *Angew. Chem. Int. Ed.* **2014,** *53*, 7584.
14. Park, S.; Shao, Y.; Liu, J.; Wang, Y., *Energy Environ. Sci.* **2012,** *5*, 9331.
15. Feng, J.; Lv, F.; Zhang, W.; Li, P.; Wang, K.; Yang, C.; Wang, B.; Yang, Y.; Zhou, J.; Lin, F., *Adv. Mater.* **2017,** *29*, 1703798.
16. Xiao, X.; Tao, L.; Li, M.; Lv, X.; Huang, D.; Jiang, X.; Pan, H.; Wang, M.; Shen, Y., *Chem. Sci.* **2018,** *9*, 1970.
17. Zhang, R.; Wang, X.; Yu, S.; Wen, T.; Zhu, X.; Yang, F.; Sun, X.; Wang, X.; Hu, W., *Adv. Mater.* **2017,** *29*, 1605502.
18. Wang, X.; Kolen'ko, Y. V.; Bao, X. Q.; Kovnir, K.; Liu, L., *Angew. Chem. Int. Ed.* **2015,** *54*, 8188.
19. Chen, W. F.; Muckerman, J. T.; Fujita, E., *Chem. Commun.* **2013,** *49*, 8896.
20. Chen, W. F.; Sasaki, K.; Ma, C.; Frenkel, A. I.; Marinkovic, N.; Muckerman, J. T.; Zhu, Y.; Adzic, R. R., *Angew. Chem. Int. Ed.* **2012,** *51*, 6131.
21. Yan, H.; Tian, C.; Wang, L.; Wu, A.; Meng, M.; Zhao, L.; Fu, H., *Angew. Chem. Int. Ed.* **2015,** *54*, 6325.
22. Jaramillo, T. F.; Jørgensen, K. P.; Bonde, J.; Nielsen, J. H.; Horch, S.; Chorkendorff, I., *Science* **2007,** *317*, 100.
23. Wang, D.-Y.; Gong, M.; Chou, H. L.; Pan, C.-J.; Chen, H. A.; Wu, Y.; Lin, M. C.; Guan, M.; Yang, J.; Chen, C. W., *J. Am. Chem. Soc.* **2015,** *137*, 1587.
24. Michalsky, R.; Zhang, Y. J.; Peterson, A. A., *ACS Catal.* **2014,** *4*, 1274.
25. Liao, L.; Wang, S.; Xiao, J.; Bian, X.; Zhang, Y.; Scanlon, M. D.; Hu, X.; Tang, Y.; Liu, B.; Girault, H. H., *Energy Environ. Sci.* **2014,** *7*, 387.

26. Ma, F. X.; Wu, H. B.; Xia, B. Y.; Xu, C. Y.; Lou, X. W., *Angew. Chem. Int. Ed.* **2015,** *54*, 15395.
27. Vrubel, H.; Hu, X., *Angew. Chem. Int. Ed.* **2012,** *51*, 12703.
28. Park, H.; Encinas, A.; Scheifers, J. P.; Zhang, Y.; Fokwa, B., *Angew. Chem. Int. Ed.* **2017,** *56*, 5575.
29. Park, H.; Zhang, Y.; Scheifers, J. P.; Jothi, P. R.; Encinas, A.; Fokwa, B. P., *J. Am. Chem. Soc.* **2017,** *139*, 12915.
30. Jothi, P. R.; Zhang, Y.; Scheifers, J. P.; Park, H.; Fokwa, B. P., *Sustainable Energy Fuels* **2017,** *1*, 1928.
31. Chen, Y.; Yu, G.; Chen, W.; Liu, Y.; Li, G.-D.; Zhu, P.; Tao, Q.; Li, Q.; Liu, J.; Shen, X., *J. Am. Chem. Soc.* **2017,** *139*, 12370.
32. Li, H.; Wen, P.; Li, Q.; Dun, C.; Xing, J.; Lu, C.; Adhikari, S.; Jiang, L.; Carroll, D. L.; Geyer, S. M., *Adv. Energy Mater.* **2017,** *7*, 1700513.
33. Jothi, P. R.; Zhang, Y.; Yubuta, K.; Culver, D.; Conley, M. P.; Fokwa, B. P., *ACS Appl. Energy Mater.* **2019,** *2*, 176.
34. Gupta, S.; Patel, N.; Miotello, A.; Kothari, D., *J. Power Sources* **2015,** *279*, 620.
35. Los, P.; Lasia, A., *J. Electroanal. Chem.* **1992,** *333*, 115.
36. Xu, N.; Cao, G.; Chen, Z.; Kang, Q.; Dai, H.; Wang, P., *J. Mater. Chem. A* **2017,** *5*, 12379.
37. Alameda, L. T.; Holder, C. F.; Fenton, J. L.; Schaak, R. E., *Chem. Mater.* **2017,** *29*, 8953.
38. Skrabalak, S. E.; Suslick, K. S., *Chem. Mater.* **2006,** *18*, 3103.
39. Pei, Y.; Zhou, G.; Luan, N.; Zong, B.; Qiao, M.; Tao, F. F., *Chem. Soc. Rev.* **2012,** *41*, 8140.
40. Zou, X.; Zhang, Y., *Chem. Soc. Rev.* **2015,** *44*, 5148.
41. Zheng, Y.; Jiao, Y.; Jaroniec, M.; Qiao, S. Z., *Angew. Chem. Int. Ed.* **2015,** *54*, 52.
42. Morales-Guio, C. G.; Stern, L. A.; Hu, X., *Chem. Soc. Rev.* **2014,** *43*, 6555.
43. Sen, S.; Ozbek, I.; Sen, U.; Bindal, C., *Surf. Coat. Technol.* **2001,** *135*, 173.
44. Yan, H.-y.; Qun, W.; Chang, S.-m.; Ping, G., *Transactions of Nonferrous Metals Society of China* **2011,** *21*, 1627.
45. Albert, B.; Hillebrecht, H., *Angew. Chem. Int. Ed.* **2009,** *48*, 8640.
46. Ndassa, I. M.; Gillessen, M.; Fokwa, B. P., *Solid State Sciences* **2013,** *17*, 14.
47. Kayhan, M. Transition Metal Borides: Synthesis, Characterization and Superconducting Properties. Technische Universität, 2013.
48. Akopov, G.; Yeung, M. T.; Kaner, R. B., *Adv. Mater.* **2017,** *29*, 1604506.
49. Iyer, A. K.; Zhang, Y.; Scheifers, J. P.; Fokwa, B. P., *J. Solid State Chem.* **2019,** *270*, 618.
50. Givord, D.; Li, H.; De La Bâthie, R. P., *Solid state communications* **1984,** *51*, 857.
51. Xu, M.; Kitazawa, H.; Takano, Y.; Ye, J.; Nishida, K.; Abe, H.; Matsushita, A.; Tsujii, N.; Kido, G., *Appl. Phys. Lett.* **2001,** *79*, 2779.
52. Nagamatsu, J.; Nakagawa, N.; Muranaka, T.; Zenitani, Y.; Akimitsu, J., *nature* **2001,** *410*, 63.

53. Nayan, N.; Murty, S. N.; Jha, A. K.; Pant, B.; Sharma, S.; George, K. M.; Sastry, G., *Materials Science and Engineering: A* **2013,** *576*, 21.
54. Fan, Z.-G.; Li, C.-y., *J. Alloys Compd.* **2007,** *436*, 178.
55. Pöttgen, R.; Johrendt, D., *Intermetallics: synthesis, structure, function*. Walter de Gruyter GmbH & Co KG: 2014.
56. Benbow, E. M.; Latturner, S. E., *J. Solid State Chem.* **2006,** *179*, 3989.
57. Kanatzidis, M. G.; Pöttgen, R.; Jeitschko, W., *Angew. Chem. Int. Ed.* **2005,** *44*, 6996.

Chapter 2

Boron-Dependency of Molybdenum Boride Electrocatalysts for the Hydrogen Evolution Reaction

2.1. Introduction

Since environmental problems and climate change became a strong public concern, interest in eco-friendly, renewable energy sources has dramatically increased. Hydrogen has emerged as one of the prospective counterplans to fossil fuels.[1-2]

In recent years, hydrogen production by water electrolysis has received a great deal of attention. Water electrolysis uses electricity to split water into hydrogen (hydrogen evolution reaction) and oxygen (oxygen evolution reaction), and thus it is a promising method to produce hydrogen from renewable resources.[3-5] Currently, noble metals such as platinum are the most active electrocatalysts for hydrogen evolution reaction (HER) due to the low overpotential and small Tafel slope. However, their high price and lack of abundance prevents their practical application. Therefore, the discovery of non-noble metal HER electrocatalysts is necessary to develop a large-scale hydrogen production and solve environmental and energy issues.[6-11]

In the last few years, molybdenum-based materials[12-22], such as molybdenum disulfide [12-14], molybdenum carbide[15-18] and molybdenum phosphides[19-22], have been extensively investigated as low-cost alternative electrocatalysts for the HER. Recently, molybdenum carbides of different compositions were reported to have excellent catalytic properties for the HER.[17] This study confirmed β-Mo_2C as best metal carbide HER catalyst and showed

a structure-dependence for the three monocarbide modifications. Metal borides can be alternative electrocatalysts because they have high melting points and are stable both in acid and base solutions.[23-24] In fact, Hu *et al.* found recently that the commercially available polycrystalline molybdenum boride (MoB) is another excellent low-cost HER catalyst both in acidic (pH = 0) and basic (pH = 14) solutions.[16] Borides have not attracted as much attention as the above-mentioned materials mainly because of the difficulty encountered during their synthesis[23-24], for example the commercially available α modification (space group $I4_1/amd$) of MoB is still contaminated by the β modification (space group *Cmcm*).[16] However, the low amount of the β-MoB impurity seems not to have affected the excellent HER activity of α-MoB much, but it also raises the question of the unknown HER activity of β-MoB.

Herein, we report on the synthesis and the first electrocatalytic study of several molybdenum borides (Mo_2B, α-MoB, β-MoB and α-MoB_2), the HER activity of which increases with increasing boron content.

2.2. Experimental section

Synthesis method

Powders of molybdenum (Mo) and boron (B) were weighted in the specified ratios (total mass 0.3 g) and pressed into pellets. The pellets were arc-melted in a water-cooled copper crucible (first electrode) under argon atmosphere with a tungsten tip as second electrode. The argon was purified over silica gel, molecular sieves, and titanium sponge (950K). We controlled the current and repeated arc melting depending on the samples to ensure

homogeneity and purity. We were able to synthesize almost single-phase materials according to the following procedures.

1. Mo_2B

   The pellet was arc-melted at 40 A in the first step until homogeneous melting occurred. Then, the current was reduced to 10 A and the melting process was repeated 5 times to ensure homogeneity.

2. α-MoB

   First, the pellet was arc-melted with a current of 60 A applied, then the current was reduced to 10 A. The arc-melting procedure was repeated 5 times with 10 A.

3. β-MoB

   In order to synthesize β-MoB, 3 % excess of boron was used. The pellet was arc-melted three times at 40 A.

4. α-MoB_2

   The starting composition was 1:1.7. The pellet was arc-melted at 40 A and the procedure was repeated 5 times.

Powder X-ray diffraction (PXRD)

Powder X-ray diffraction patterns of polycrystalline samples were recorded using a Rigaku Miniflex-600. The operating conditions were 40 kV and 15 mA generating Cu K_α radiation (λ=1.543 Å). The recorded powder X-ray diffractograms were refined by means of the Rietveld method (full-matrix least-squares refinement) as implemented in the FULLPROF program suite.

XPS, SEM and EDX

X-ray photoelectron spectroscopy (XPS) was carried out by using a Kratos AXIS ULTRA ^{DLD} XPS system equipped with an A1 Kα monochromated X-ray source and a 165 mm mean radius electron energy hemispherical analyzer.

The compositions and particle sizes were analyzed by Scanning Electron Microscopy (SEM) and quantitative Energy Dispersive X-ray Spectroscopy (EDX), respectively, on a ultra-high resolution low-energy system of the type Nova NanoSEM450 equipped with an 50mm^2 X-Max50 SD EDX detector.

BET surface area

The BET surface area was determined by nitrogen sorption isotherm at 77 K using volumetric adsorption system (ASAP 2020, Micromeritics Inc., USA). All of the samples were heated at 120 ^{o}C for 4 hours to remove the adsorbed moisture and clean the surface.

Electrochemical characterization

A three-electrode system was used to measure electrochemical properties. The reference electrode was a saturated calomel electrode (SCE) and the counter electrode was a platinum wire. The working electrodes were prepared as follows: a mixture of 20 mg of the respective manually ground Mo boride powder with 200 µl DI water, 1000 µl IPA and 20 µl nafion was sonicated for 20 min to obtain homogenous suspension, which was sprayed

on a carbon sheet (2x2 cm^2). The carbon sheet with sample was dried overnight in an oven at 50 ^oC. The weight gain is about 0.2-0.3 mg/cm^2.

Linear sweep voltammetry (LSV) and cyclic voltammetry (CV) were carried out on a VSP multipotentiostat/galvanostat (Bio-Logic VSP, France) using a three-electrode system in 0.5 M H_2SO_4 solution at room temperature. The LSV and CV experiments were performed within -1.0 to 0 V at a scan rate of 1 mV/s and 100 mV/s, respectively. All potentials are reported with respect to the reversible hydrogen electrode (RHE) according to the follow conversion:

$$\mathrm{RHE} = \mathrm{SCE} + 0.242 + 0.059 \times \mathrm{pH}$$

iR-drop by solution resistance and parasitic resistance was corrected using the following equation: $E_{iR\text{-corrected}} = E_{\mathrm{RHE}} - iR_{\Omega}$, where iR_{Ω} is *iR*-drop and E_{RHE} is the potential *vs.* reversible hydrogen electrode. The Tafel slopes of all samples were corrected for the *iR*-drop.

The electrochemically active surface area of the samples can be estimated from cyclic voltammetry (CV) measured at various scan rates. [14, 25] The CV measurements were carried out in the region of 0.1 – 0.2 V vs. RHE. The double layer capacitance (C_{dl}) was estimated by plotting the ΔJ (J_a-J_c) at 0.15 V vs. RHE against the scan rate.

2.3. Results and discussion

Polycrystalline powder samples of these materials have been synthesized by several arc-melting procedures. In brief, high purity molybdenum and boron elements were weighed in appropriate stoichiometric ratios (total mass 0.3 g) and pressed into pellets. The pellets were arc-melted in an arc furnace chamber under argon atmosphere, however

choosing the appropriate arc-melting conditions (e.g. applied current) turned out to be essential for the successful synthesis of these phases. The products were analyzed by powder X-ray diffraction (PXRD), semi-quantitative energy dispersive X-ray spectroscopy (EDX), and X-ray photoelectron spectroscopy (XPS). **Figure 2.1** shows the X-ray diffraction patterns of all four molybdenum-boride products, while the Rietveld refinements data are given in **Figure 2.2** and **Table 2.1**. All phases could be obtained with weight percentage of ca. 90%, with impurity phases of Mo and other binary borides (**Table 2.1**). Therefore, Mo and amorphous boron were also characterized for their HER-activity.

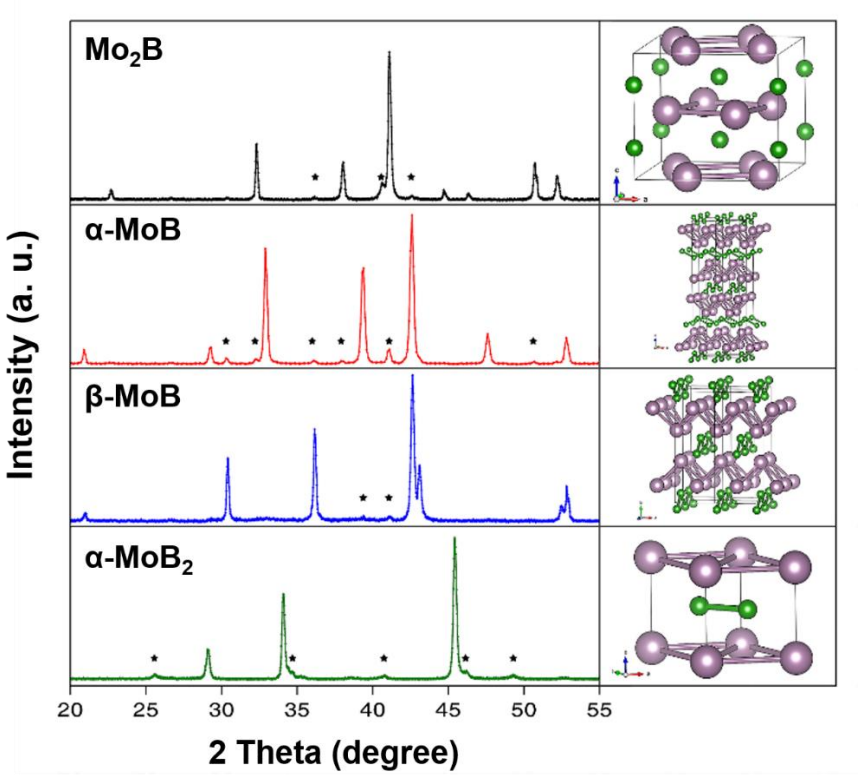

Figure 2.1. (left) X-ray powder diffraction patterns and (right) crystal structures of Mo_2B, α-MoB, β-MoB and α-MoB_2. Peaks of impurity phases are indicated (*).

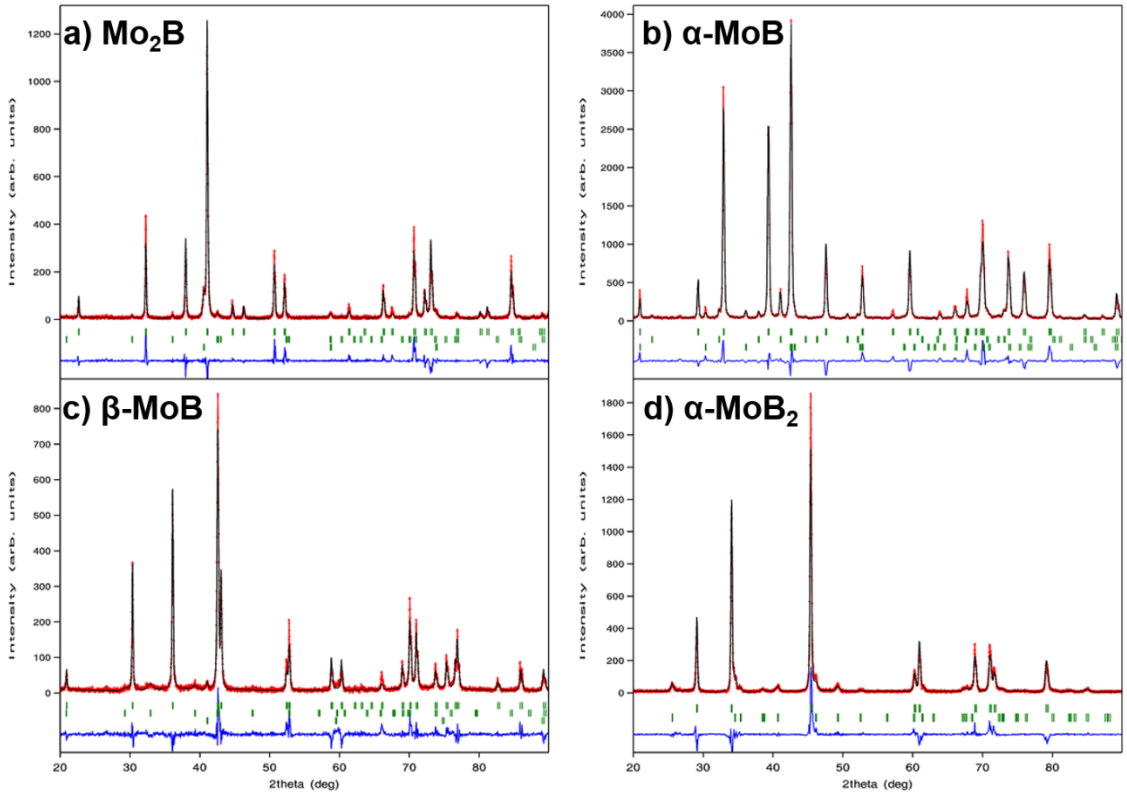

Figure 2.2. Refined powder X-ray diffraction data: a) Mo_2B, b) α-MoB, c) β-MoB and d) α- MoB_2 showing the data points (red), the calculated profile (black), the difference plot (blue) and the reflection positions (green).

Table 2.1. Crystallographic information for the studied molybdenum borides. Reported lattice parameters are given in brackets. [26-28]

Phase	Mo_2B
Crystal system	Tetragonal
Space group	*I*4/*mcm*
a [Å]	5.5463(5)-[5.5430]
c [Å]	4.7374(5)-[4.7350]
V [Å^3]	145.73(2)-[145.48]
Calc. density [g/cm^3]	9.239
Impurity 1 (Mo) [wt.-%]	8.3(6)
Impurity 2 (β-MoB) [wt.-%]	2.7(3)
Phase	α-MoB
Crystal system	Tetragonal
Space group	$I4_1/amd$
a [Å]	3.1019(6) – [3.1050]
c [Å]	16.967(6) – [16.9700]
V [Å^3]	163.25(6) – [163.61]
Calc. density [g/cm^3]	8.687
Impurity 1 (Mo_2B) [wt.-%]	5.2(5)
Impurity 2 (β-MoB) [wt.-%]	4(1)
Phase	β-MoB
Crystal system	Orthorhombic
Space group	*Cmcm*
a [Å]	3.1375(4)-[3.1418]
b [Å]	8.483(1)-[8.4961]
c [Å]	3.0691(4)-[3.0721]
V [Å^3]	81.68(2)-[82.0]
Calc. density [g/cm^3]	8.638
Impurity 1 (α-MoB) [wt.-%]	8.0(5)
Impurity 2 (Mo) [wt.-%]	3(2)
Phase	α-MoB_2
Crystal system	Hexagonal
Space group	*P*6/*mmm*
a [Å]	3.0387(6) – [3.0049]
c [Å]	3.0694(8) – [3.1726]
V [Å^3]	24.545(9) – [24.81]
Calc. density [g/cm^3]	7.954
Impurity (Mo_2B_{5-x}) [wt.-%]	12.9(5)

Quantitative EDX analysis (using Mo_2B as standard and applying point measurement) were carried out on pressed polycrystalline samples, the results of which confirmed the expected metal to boron molar ratio from each composition (**Figure 2.3**). Per scanning electron microscopy (SEM) analysis, all analyzed bulk phases have similar but irregular particle shapes and their size distributions range from 1μm up to 15 μm (**Figure 2.4**). The fact that our synthesized α-MoB sample has larger average particle size than the commercially available sample (1 - 3 μm)[16] indicates that it may also have lower catalytic activity. However, it was important for this type of study that all synthesized compounds have comparable particle sizes, to safely compare their HER activity. Because the HER activity is also related to the crystal structure, it is important to understand the differences between the structures. The four metal borides all have high symmetry structures: Orthorhombic β-MoB, tetragonal Mo_2B and α-MoB, and hexagonal α-MoB_2 (**Figure 2.1, right**). If these crystal structures are related to their boron substructures some similarities but also clear differences emerge: In fact, with increasing boron content the B-B connectivity increases from 0D (isolated boron atoms in Mo_2B) to 1D (zig zag boron chains in α-MoB and β-MoB) and to 2D (graphene-like boron layers in α-MoB_2).

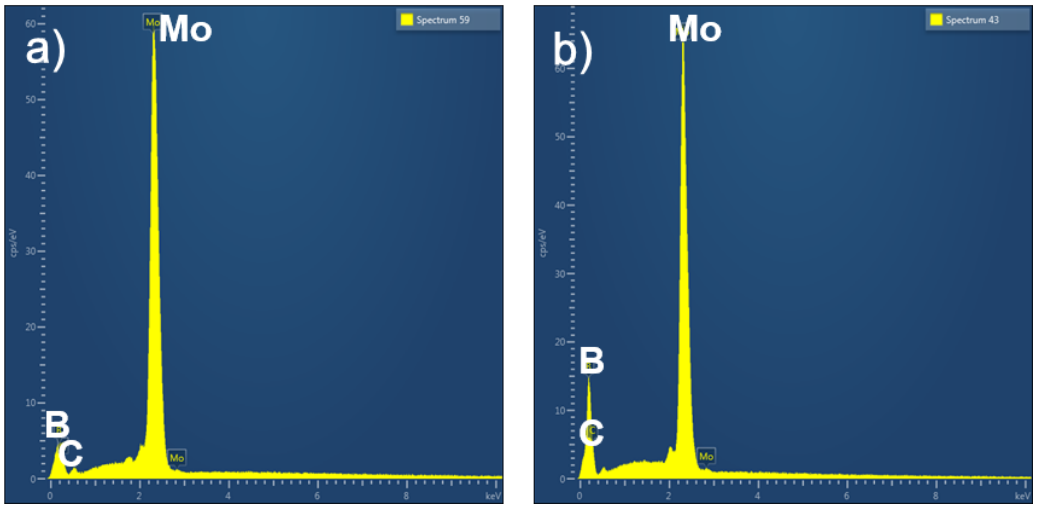

Figure 2.3. EDX spectra of a) Mo_2B and b) α-MoB_2. The carbon peak is due to the carbon tape.

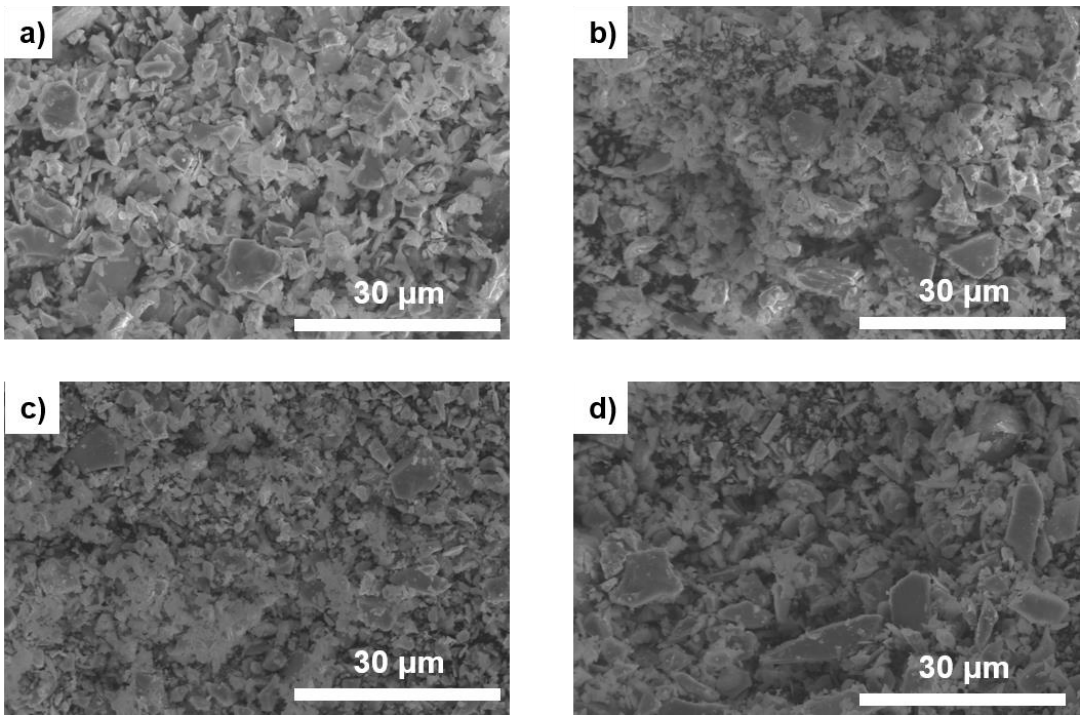

Figure 2.4. SEM images of a) Mo_2B, b) α-MoB c) β-MoB, d) α-MoB_2.

Figure 2.5 shows the electrocatalytic activity of the four molybdenum borides measured in a 0.5 M H_2SO_4 solution at a scan rate of 1 mV/s. The working electrode was prepared by spraying a sonicated sample (0.2 - 0.3 mg/cm^2) onto a carbon sheet. The HER activity for samples of Pt on carbon (Pt/C), molybdenum, amorphous boron and carbon sheet are also listed in **Figure 2.5** for comparison. The polarization curves indicate that Pt/C has the highest catalytic activity as expected, while the carbon sheet is not active. Molybdenum and amorphous boron have poor activity, but molybdenum is more active than boron (**Figure 2.5**). However, among the borides, the Mo-rich compound (Mo_2B) has the lowest HER activity. Upon increasing the amount of boron, the HER activity greatly increases for α-MoB, then it further slightly increases for β-MoB and finally it also slightly increases for α-MoB_2. These results show a boron-dependency of these borides for the HER activity. Similar findings were reported recently in two phosphide systems: It was found that a higher degree of phosphorization results in better HER performance in the order Mo, Mo_3P and MoP[19], while investigations of nanocrystals of nickel phosphide phases show that a higher phosphorus content leads to high HER activity in the order $Ni_{12}P_5$ (29 at.% P), Ni_2P (33 at.% P) and Ni_5P_4 (44 at.% P)[29]. However, it was also shown recently that the Mo-rich β-Mo_2C is more active than all MoC modifications, even though one modification (γ-MoC) was reported to have similar activity as β-Mo_2C.[17] These results suggest that a general trend is impossible to predict because several other factors (beside the composition), such as structure, particle size, morphology, nature of active sites, influence the HER activity. Therefore, each system should be studied independently to find, not only the best catalyst within the system, but also the factors influencing its catalytic

activity. In the here studied system, there is a clear boron-dependence of these materials for the HER activity, which means that boron may play a significant role in the active sites of these materials. However, the change in crystal structures should also be taken onto account, but even the crystal structures are influenced by the boron content as seen above. Computational and spectroscopic investigations (active sites studies) are needed to understand their HER activity.

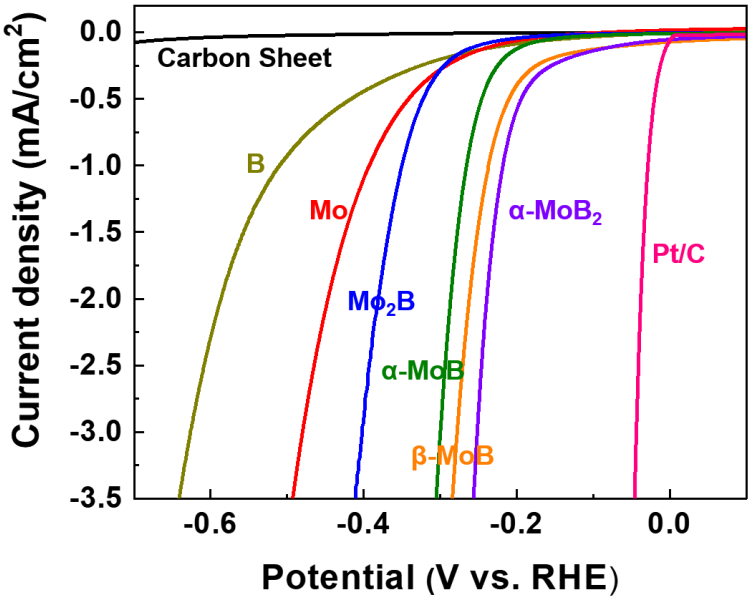

Figure 2.5. Polarization curves for amorphous B, Mo, Mo_2B, α-MoB, β-MoB and α-MoB_2 measured in 0.5 M H_2SO_4. *IR*-drop was corrected.

The Tafel analysis is commonly used to probe the HER mechanism through estimation of the rate-determining step (RDS). In general, three reactions are used as RDS of the HER in acidic solutions, namely the Volmer reaction (with Tafel slope of ~120 mV/decade), the Heyrovsky reaction (Tafel slope of ~40 mV/decade) and the Tafel reaction (Tafel slope of

~30 mV/decade).[30-32] However, it is important to note that this method is strongly particle size dependent, thus different mechanisms may be obtained for the same material if it has different particle sizes. For example, it was recently shown that the commercial Mo_2C has a twice larger Tafel slope (~100 mV/decade) than the synthesized Mo_2C (50 mV/decade) because of the larger average particle size in the commercial sample.[33] For the same reason, our synthesized α-MoB (1 - 10 μm) has a larger Tafel slope (76 mV/decade, see **Figure 2.6**) than the commercial sample with smaller particles (1 - 3 μm, 55 mV/decade).[16] A nice consequence of this analysis is that similar Tafel slopes to that of α-MoB can be expected for α-MoB_2 and β-MoB, because all have similar particle sizes and similar HER activities. Indeed, values of 75 and 84 mV/decade (see **Figure 2.6**) are found for α-MoB_2 and β-MoB, respectively. Like commercial α-MoB, it is difficult to determine the RDS using Tafel analysis in the current systems, because the measured Tafel slopes are far from the above-given limiting slopes. Also, it is very probable that the Volmer step is very quick. Although the above size-dependent analysis corroborates well with previously reported cases, it is important to point out, that the here reported materials have large particle sizes (μm) and irregular shapes. Therefore, other factors such as sample porosity, different crystal orientations or/and different surface terminations (e.g. B, Mo, or both) will surely play a greater role on the rate determining step.

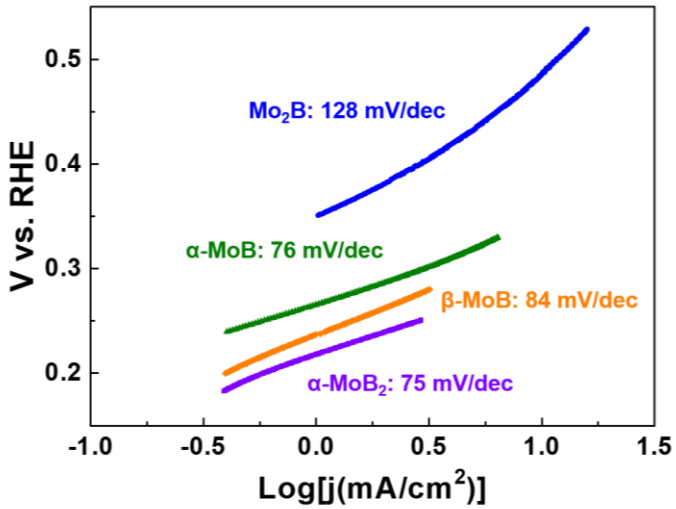

Figure 2.6. The corresponding Tafel plots of Mo_2B, α-MoB, β-MoB and α-MoB_2. Scan rate was 1mV/s. *IR*-drop was corrected.

The BET (Brunauer, Emmett and Teller) surface area of all catalysts was measured. As expected for microcrystalline and nonporous samples (see isotherms given as **Figure 2.7**), the surface area is small (3.97 - 15.27 m^2/g). The BET adsorption isotherms of all four phases are similar as expected, and their shapes correspond to those found for non-porous materials. The only conclusion that can be drawn from these data is that the more HER active of the two MoB modifications also has the greater surface area. However, the fact that one of the smallest surface area is found for the most active material α-MoB_2, while the least active material (Mo_2B) has the second highest surface area indicates that the HER activity difference in these bulk materials is more influenced by other factors (such as the nature of the active site) than the total surface area. However, increasing the surface area through nanomaterials synthesis would expose more active sites and affect the HER activity.

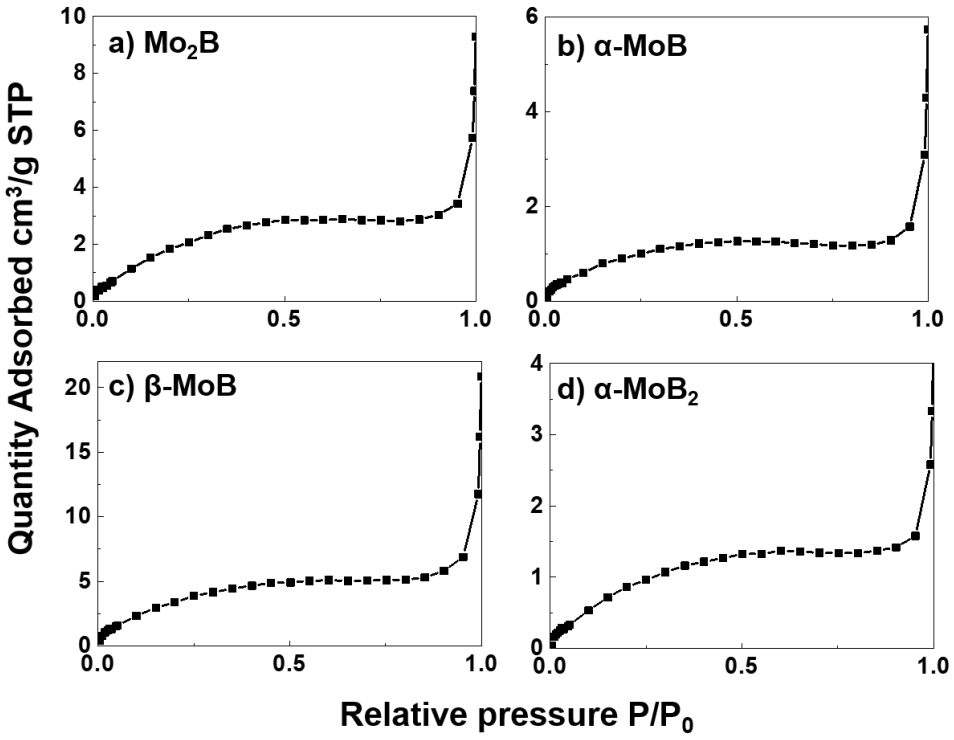

Figure 2.7. BET adsorption isotherm of a) Mo_2B (9.09 m^2/g), b) α-MoB (3.97 m^2/g) and c) β-MoB (15.27 m^2/g) and d) α-MoB_2 (4.23 m^2/g).

The double layer capacitance (C_{dl}) is linearly proportional to the effective surface area because the double layer charging current, i_c, is proportional to both the scan rate, ν, and the electrochemically active surface area of the electrode, A_{echem}.[34]

$$i_c \propto \nu \times A_{echem}$$

It is difficult to determine the exact active surface area due to unknown capacitive behavior of the Mo-B electrodes, but one can estimate the relative active surface area.

To get an estimation of the active sites, we have estimated the double layer capacitance (C_{dl}) which is proportional to the electrochemically active surface area. The results are

summarized in **Figure 2.8a-e**. The estimated double layer capacitances are 4.01, 5.94, 6.12 and 10.10 x 10^{-2} $\mu F/cm^2$ for Mo_2B, α-MoB, β-MoB and α-MoB_2, respectively.

α-MoB_2 has the highest double layer capacitance and thus more effective active sites, because C_{dl} is proportional to the electrochemically active surface area. The larger activity of the active sites is ultimately responsible for its HER activity being the highest among our samples. They show that the estimated electrochemically active surface area increases with increasing boron content from Mo_2B to α-MoB_2.

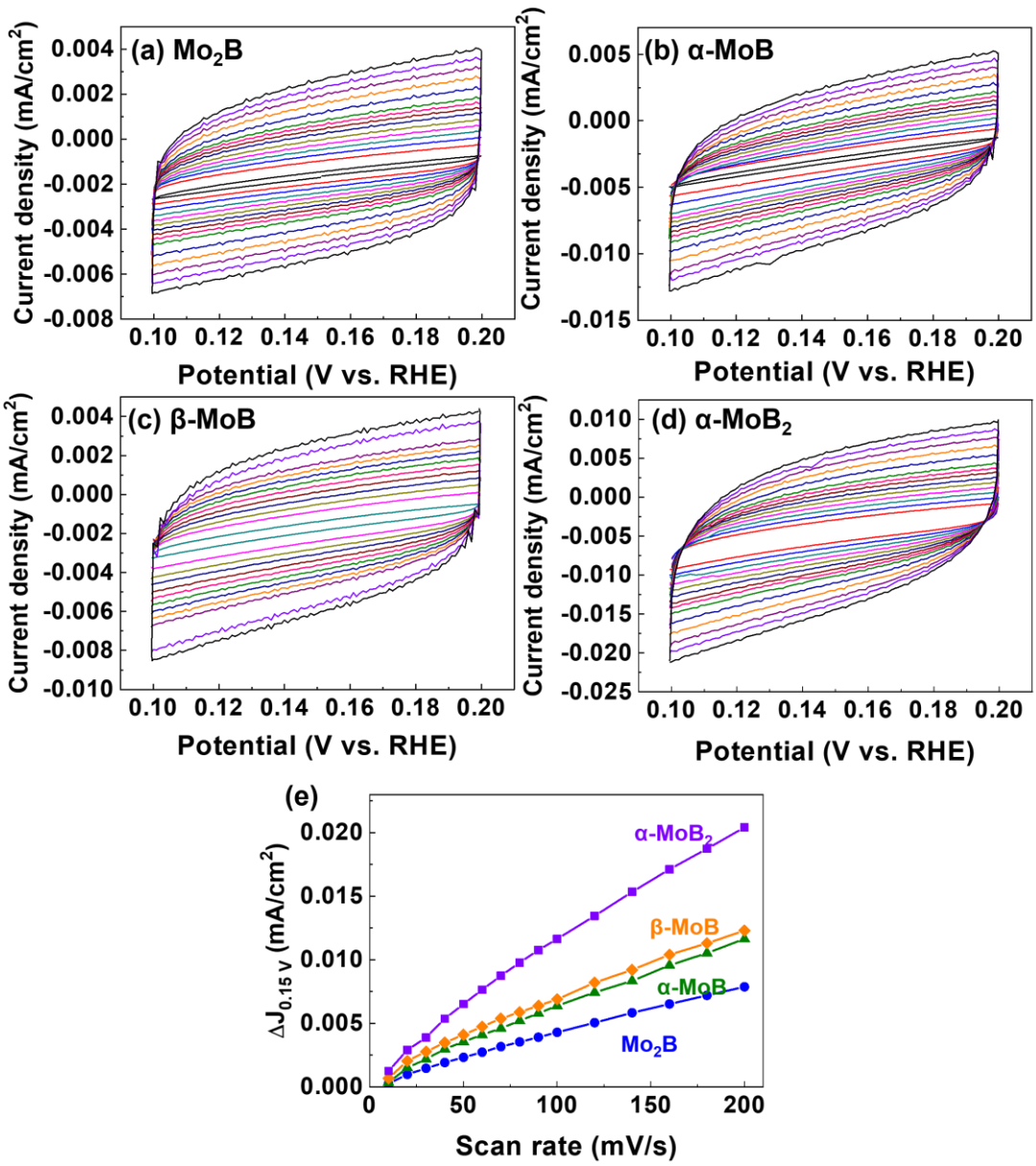

Figure 2.8. Cyclic voltammetry curves of a) Mo_2B, b) α-MoB and c) β-MoB and d) α-MoB_2. e) The difference current density ΔJ (J_a-J_c) at 1.5 V vs. RHE plotted against the scan rate is fitted to a linear regression to estimate C_{dl}.

To probe the purity and electronic structure of all four molybdenum boride phases, Mo 3d core level XPS spectra were collected before activation (**Figure 2.9**). 1s core level spectra of B, O and C are given as supporting information (**Figure 2.10**). The surface of commercial α-MoB was shown to be heavily contaminated by MoO_3 and MoO_2 before activation, but these oxides nearly all disappeared after activation.[16] In our freshly prepared samples, the oxide signals are smaller while the signals attributed to the borides are much larger, indicating that the surfaces of the freshly prepared samples are less contaminated by the oxides (MoO_3, MoO_2 and Mo_2O_3). Intensity fitting suggests that the surfaces of α-MoB and β-MoB are more contaminated than those of Mo_2B and α-MoB_2, also in accordance with higher intensities of the peaks attributed to the borides (at ca. 232 and ca. 228 eV) in the latter two cases. These peaks also correspond to those attributed to Mo^0 in earlier studies on carbides and phosphides phases.[16-17, 21, 29] The peak area of the B (1s) spectra increases with increasing boron content (**Figure 2.10a, b, c**) from Mo_2B to α-MoB_2, thus confirming the above-mentioned PXRD and EDX results.

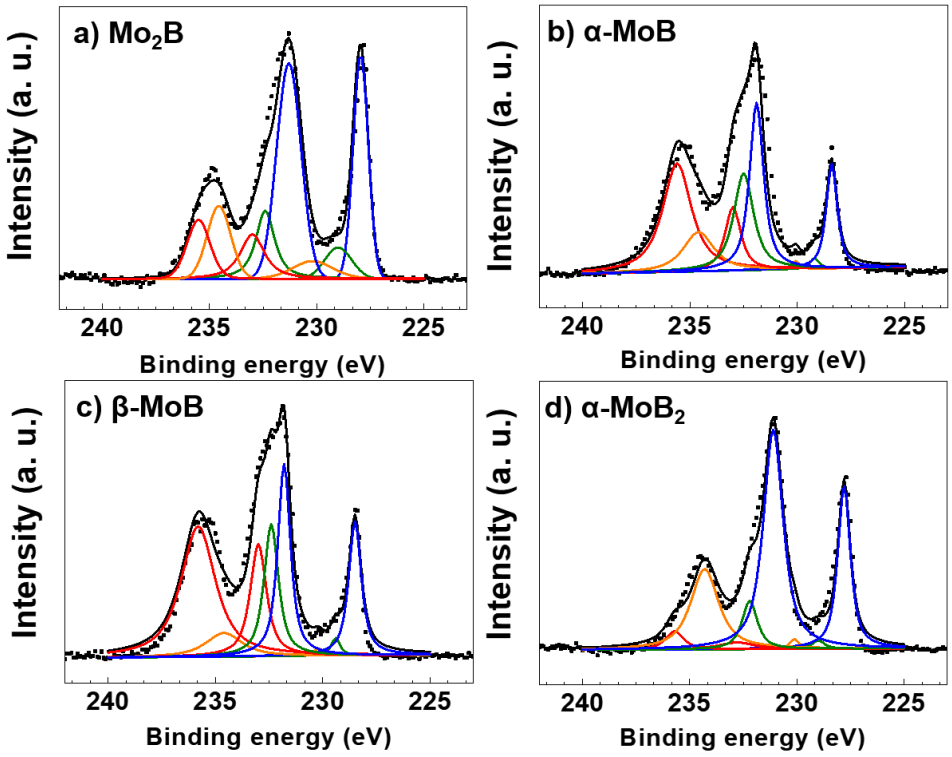

Figure 2.9. XPS Mo spectra of a) Mo_2B, b) α-MoB, c) β-MoB and d) α-MoB_2. Experimental data (black squares), fitting peaks (black curves), MoO_3 (red curves), MoO_2 (orange curves), Mo_2O_3 (green curves) and Mo peaks from the respective molybdenum borides (blue curves).

Table 2.2. XPS parameters (peak position and full width at half maximum (FWHM)) on four phases of molybdenum borides. [16-17]

Phase	Species	Peak position (eV)	FWHM (eV)
Mo_2B	Mo^0	227.9, 231.3	0.83, 1.34
	Mo^{3+}	229.0, 232.4	1.5, 1.0
	Mo^{4+}	230.0, 234.5	2.22, 1.3
	Mo^{6+}	233.0, 235.5	1.35, 1.27
α-MoB	Mo^0	228.4, 231.9	0.61, 0.78
	Mo^{3+}	229.2, 232.5	0.5, 1.1
	Mo^{4+}	230.1, 234.6	0.5, 1.7
	Mo^{6+}	233.0, 235.6	0.88, 1.6
β-MoB	Mo^0	228.5, 231.8	0.7, 0.7
	Mo^{3+}	229.4, 232.4	0.5, 0.8
	Mo^{4+}	230.2, 234.6	0.5, 2
	Mo^{6+}	233.0, 235.8	0.9, 1.9
α-MoB_2	Mo^0	227.8, 231.1	0.7, 1.1
	Mo^{3+}	229.0, 232.8	0.7, 2
	Mo^{4+}	230.1, 234.3	0.5, 1.55
	Mo^{6+}	232.2, 235.7	0.85, 1

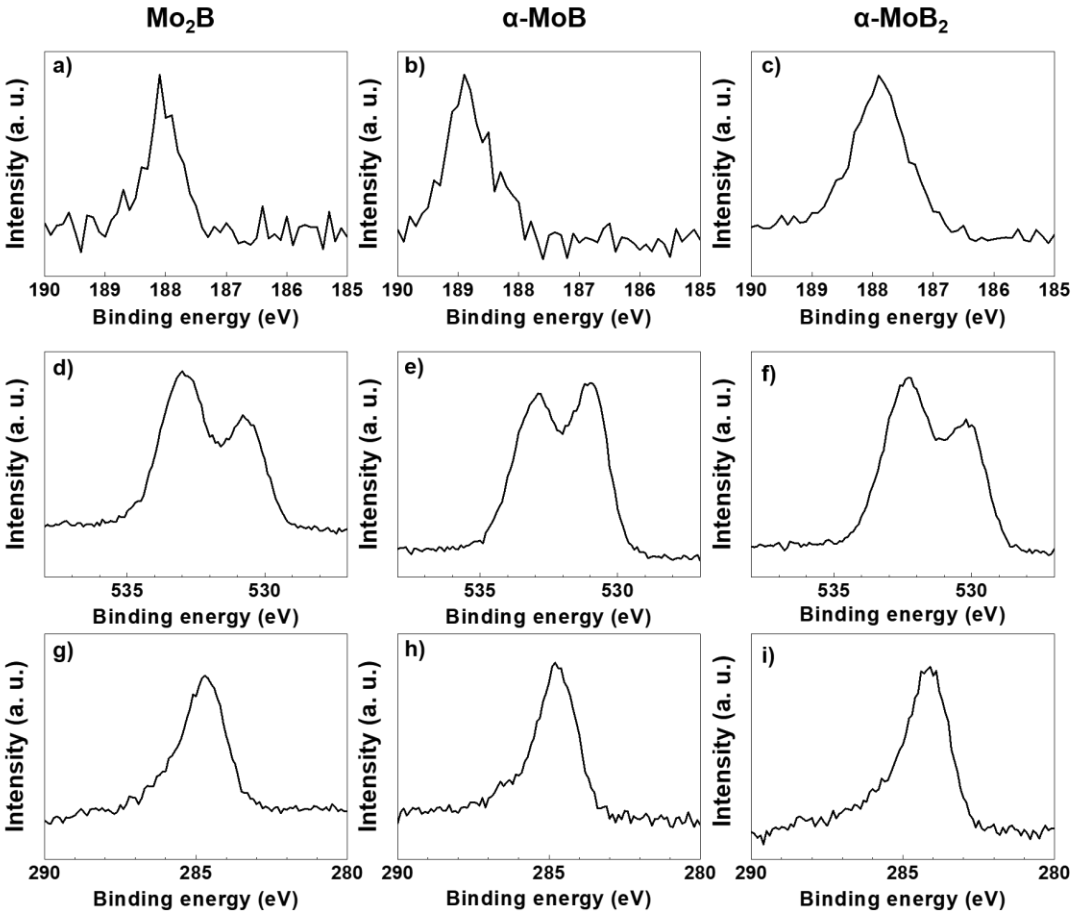

Figure 2.10. B(1s) XPS spectra for a) Mo_2B, b) α-MoB and c) MoB_2. O(1s) XPS spectra for d) Mo_2B, e) α-MoB and f) α-MoB_2. C(1s) XPS spectra for g) Mo_2B, h) α-MoB and i) α-MoB_2

The long-term stability of the two best HER catalysts (α-MoB_2 and β-MoB) was evaluated in acidic solution by cyclic voltammetry (CV) for 1000 cycles (**Figure 2.11**). After 1000 cycles, the two catalysts still performed as well as during the initial cycle, confirming the general stability of borides in acids, which was also found for the commercial α-MoB HER catalyst.[16]

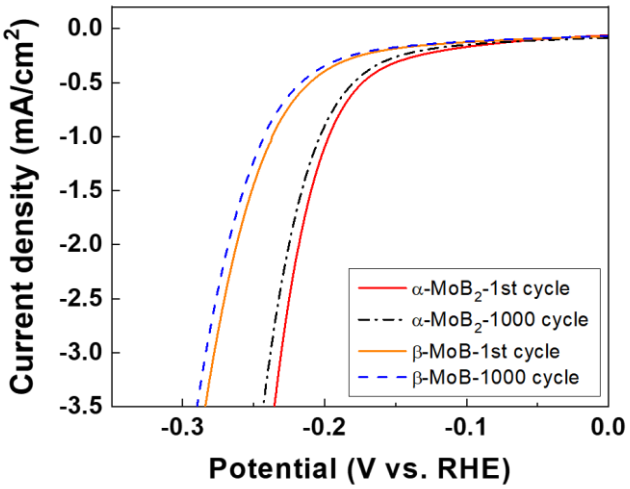

Figure 2.11. Stability measurements (cyclic voltammetry) of β-MoB and α-MoB_2 for the first and the 1000th cycle in 0.5 M H_2SO_4. Scan rate was 100 mV/s. *IR*-drop was corrected.

2.4. Conclusion

In conclusion, three binary polycrystalline molybdenum borides have been successfully synthesized and tested as HER electrocatalysts and analyzed by XPS for the first time. While β-MoB and α-MoB_2 have similarly high HER activity as the reported α-MoB[16], the Mo-rich Mo_2B shows the lowest activity. β-MoB and α-MoB_2 show the highest activity and stability in acidic solution for any boride studied to date. Even though the HER activity of these borides is already very good, the irregular shape and large size of the particles studied implies that their catalytic performances can be further increased if these materials could be studied at the nanoscale. The recent advances in the synthesis of borides nanomaterials[35-36] suggest that a bright future awaits this exciting class of materials as HER electrocatalysts.

References

1. Turner, J. A., *Science* **2004,** *305*, 972.
2. Walter, M. G.; Warren, E. L.; McKone, J. R.; Boettcher, S. W.; Mi, Q.; Santori, E. A.; Lewis, N. S., *Chem. Rev.* **2010,** *110*, 6446.
3. Merki, D.; Hu, X., *Energy Environ. Sci.* **2011,** *4*, 3878.
4. Zeng, M.; Li, Y., *J. Mater. Chem. A* **2015,** *3*, 14942.
5. Morales-Guio, C. G.; Stern, L. A.; Hu, X., *Chem. Soc. Rev.* **2014,** *43*, 6555.
6. Karunadasa, H. I.; Chang, C. J.; Long, J. R., *Nature* **2010,** *464*, 1329.
7. Wang, M.; Chen, L.; Sun, L., *Energy Environ. Sci.* **2012,** *5*, 6763.
8. Faber, M. S.; Jin, S., *Energy Environ. Sci.* **2014,** *7*, 3519.
9. Zou, X.; Zhang, Y., *Chem. Soc. Rev.* **2015,** *44*, 5148.
10. Zhou, W.; Jia, J.; Lu, J.; Yang, L.; Hou, D.; Li, G.; Chen, S., *Nano Energy* **2016,** *28*, 29.
11. Miao, J.; Xiao, F.-X.; Yang, H. B.; Khoo, S. Y.; Chen, J.; Fan, Z.; Hsu, Y.-Y.; Chen, H. M.; Zhang, H.; Liu, B., *Science advances* **2015,** *1*, e1500259.
12. Laursen, A. B.; Kegnæs, S.; Dahl, S.; Chorkendorff, I., *Energy Environ. Sci.* **2012,** *5*, 5577.
13. Kibsgaard, J.; Chen, Z.; Reinecke, B. N.; Jaramillo, T. F., *Nat. Mater.* **2012,** *11*, 963.
14. Lukowski, M. A.; Daniel, A. S.; Meng, F.; Forticaux, A.; Li, L.; Jin, S., *J. Am. Chem. Soc.* **2013,** *135*, 10274.
15. Chen, W.-F.; Wang, C.-H.; Sasaki, K.; Marinkovic, N.; Xu, W.; Muckerman, J.; Zhu, Y.; Adzic, R., *Energy Environ. Sci.* **2013,** *6*, 943.
16. Vrubel, H.; Hu, X., *Angew. Chem. Int. Ed.* **2012,** *51*, 12703.
17. Wan, C.; Regmi, Y. N.; Leonard, B. M., *Angew. Chem. Int. Ed.* **2014,** *53*, 6407.
18. Fan, M.; Chen, H.; Wu, Y.; Feng, L.-L.; Liu, Y.; Li, G.-D.; Zou, X., *J. Mater. Chem. A* **2015,** *3*, 16320.
19. Xiao, P.; Sk, M. A.; Thia, L.; Ge, X.; Lim, R. J.; Wang, J.-Y.; Lim, K. H.; Wang, X., *Energy Environ. Sci.* **2014,** *7*, 2624.
20. Xing, Z.; Liu, Q.; Asiri, A. M.; Sun, X., *Adv. Mater.* **2014,** *26*, 5702.
21. McEnaney, J. M.; Crompton, J. C.; Callejas, J. F.; Popczun, E. J.; Biacchi, A. J.; Lewis, N. S.; Schaak, R. E., *Chem. Mater.* **2014,** *26*, 4826.
22. Yang, J.; Zhang, F.; Wang, X.; He, D.; Wu, G.; Yang, Q.; Hong, X.; Wu, Y.; Li, Y., *Angew. Chem. Int. Ed.* **2016,** *55*, 12854.
23. Albert, B.; Hillebrecht, H., *Angew. Chem. Int. Ed.* **2009,** *48*, 8640.
24. Fokwa, B. P., *Encyclopedia of Inorganic and Bioinorganic chemistry* **2011**, 1.
25. Xie, J.; Zhang, J.; Li, S.; Grote, F.; Zhang, X.; Zhang, H.; Wang, R.; Lei, Y.; Pan, B.; Xie, Y., *J. Am. Chem. Soc.* **2013,** *135*, 17881.
26. Ade, M.; Hillebrecht, H., *Inorg. Chem.* **2015,** *54*, 6122.
27. Kiessling, R.; Wetterholm, A.; Sillén, L. G.; Linnasalmi, A.; Laukkanen, P., *Acta Chem. Scand* **1947,** *1*, 893.
28. Klesnar, H.; Aselage, T.; Morosin, B.; Kwei, G., *J. Alloys Compd.* **1996,** *241*, 180.

29. Pan, Y.; Liu, Y.; Zhao, J.; Yang, K.; Liang, J.; Liu, D.; Hu, W.; Liu, D.; Liu, Y.; Liu, C., *J. Mater. Chem. A* **2015,** *3*, 1656.
30. Li, Y.; Wang, H.; Xie, L.; Liang, Y.; Hong, G.; Dai, H., *J. Am. Chem. Soc.* **2011,** *133*, 7296.
31. Ji, S.; Yang, Z.; Zhang, C.; Liu, Z.; Tjiu, W. W.; Phang, I. Y.; Zhang, Z.; Pan, J.; Liu, T., *Electrochim. Acta* **2013,** *109*, 269.
32. Tang, Y. J.; Gao, M. R.; Liu, C. H.; Li, S. L.; Jiang, H. L.; Lan, Y. Q.; Han, M.; Yu, S. H., *Angew. Chem. Int. Ed.* **2015,** *54*, 12928.
33. Ma, L.; Ting, L. R. L.; Molinari, V.; Giordano, C.; Yeo, B. S., *J. Mater. Chem. A* **2015,** *3*, 8361.
34. Benck, J. D.; Chen, Z.; Kuritzky, L. Y.; Forman, A. J.; Jaramillo, T. F., *ACS Catal.* **2012,** *2*, 1916.
35. Portehault, D.; Devi, S.; Beaunier, P.; Gervais, C.; Giordano, C.; Sanchez, C.; Antonietti, M., *Angew. Chem. Int. Ed.* **2011,** *50*, 3262.
36. Gouget, G.; Beaunier, P.; Portehault, D.; Sanchez, C., *Faraday Discuss.* **2016,** *191*, 511.

Chapter 3

Graphene- and Phosphorene-like Boron Layers with Contrasting Activities in Highly Active β-MoB_2 for Hydrogen Evolution

3.1. Introduction

Hydrogen has been considered as the most promising, sustainable, clean and renewable energy carrier.[1-2] Hydrogen can be produced from the electrochemical water splitting through the hydrogen evolution reaction (HER). This method is highly attractive because it is efficient, clean and sustainable for large scale hydrogen production.[3] Among the metals, noble metals such as platinum are the best HER catalysts because they have an overpotential close to zero volts, but low abundance and high cost of these materials limit their large-scale application.[4-7] Thus, the development of low-cost, high-performance non-noble-metal catalysts to replace the precious metals is important and necessary to make hydrogen a cost-effective energy carrier.

Recently, electrocatalysts based on earth-abundant elements such as sulfides,[8-9] nitrides,[10-11] phosphides,[12-13] carbides,[14-15] borides,[16-20] were shown to have a high HER catalytic activity. In addition, non-metallic carbon materials have also shown HER catalytic activity.[21] Among these alternatives, molybdenum based materials such as molybdenum disulfide (MoS_2)[8], molybdenum phosphide (MoP)[12], molybdenum carbide (MoC)[22] and molybdenum boride (MoB)[16-17] have received a great deal of attention due to their low cost and high activity. To further enhance the HER activity, nanoscale[23-24,] and porous Mo-based[25] materials have been studied. However, there are only a few studies on the HER

activity of Mo-based borides.[16-17] The main challenge for this class of materials, even at the microscale, is their single-phase synthesis. For example, the commercially available α-MoB is still contaminated by β-MoB.[16] The fact that they are already highly active in the bulk accelerates the discovery of HER active borides. Another advantage of metal boride is their stability in acidic and basic solutions. Thus, extensive HER activity investigations for this large group of compounds are particularly promising. Using arc-melting procedures, high purity (> 95 wt.%, weight percent) of the binary bulk molybdenum borides Mo_2B, α-MoB, β-MoB and α-MoB_2 could recently be synthesized. The high purity allowed the study of their HER activity, which turned out to increase with increasing boron content in the order Mo_2B, α-MoB, β-MoB and α-MoB_2.[17] One potentially interesting phase, β-MoB_2 (with the same boron content as α-MoB_2), could not be synthesized with sufficient purity by this method. In this work, we have achieved the first single-phase synthesis in the Mo-B system using the tin flux method, and it has enabled the discovery of one of the highly active bulk borides to date, β-MoB_2.

3.2. Experimental section

Synthesis method

Molybdenum (Mo), boron (B) and tin (Sn) were weighted in the ratio 2:5:10 (total mass 3 g) and pressed into a pellet. The pellet was sealed in quartz tube under vacuum. The quartz tube was transferred into a box furnace and heated to 1100 °C in 11 h. The temperature was kept constant for 72 h. Then, the furnace was cooled down to 200 °C at a cooling rate of

50 °C/h then naturally to room temperature. The sample was removed from the quartz tube and dispensed into conc. HCl solution for 2 days. Thereafter it was washed with deionized (DI) water and ethanol. Finally, the obtained product was dried at room temperature.

This new synthesis procedure has greatly simplified the preparation of single-phase samples if compared with the recent method: In fact, in the previous synthesis by Albert et al. (*Z. Anorg. Allg. Chem.* **2007,** *633*, 2626.) they heated an elemental mixture (2Mo:4B) in quartz ampoules at 1100 °C in Ar atmosphere for 14 days, followed by intermediate grinding and re-pelleting. Then, they heated the resulting sample again at 1300 °C in Ta crucible in flowing Ar for 3 days.

Powder X-ray diffraction (PXRD)

Powder X-ray diffraction patterns of the sample was recorded using a Rigaku Miniflex-600 and operating condition were 40 kV and 15 mA generating Cu K_α radiation (λ=1.5418 Å). The recorded powder X-ray diffractogram was refined by means of the Rietveld method (full-matrix least-squares refinement) as implemented in the FULLPROF program suite.

XPS, SEM and EDX

X-ray photoelectron spectroscopy (XPS) was carried out using a Kratos AXIS ULTRA ^{DLD} XPS system equipped with an A1 Kα monochromated X-ray source and a 165 mm mean radius hemispherical electron energy analyzer.

The compositions and particle sizes of the synthesized material was analyzed by using scanning electron microscopy (SEM) and energy dispersive X-ray spectroscopy (EDS), on the ultra-high-resolution low-energy system Nova NanoSEM450 equipped with a 50mm^2 X-Max50 SD EDX detector.

BET surface area

The BET surface area was determined by the nitrogen adsorption isotherm at 77 K using a volumetric adsorption system (ASAP 2020, Micromeritics Inc., USA). The sample was heated to 120 ^{o}C for 4 hours to remove the adsorbed moisture and clean the surface before the measurement.

Electrochemical characterization

The electrochemical measurements were carried out VSP multipotentiostat/galvanostat (Bio-Logic VSP, France) using a three-electrode system in 0.5 M H_2SO_4 solution at room temperature. A saturated calomel electrode (SCE) was used as reference electrode and a graphite rod was used as counter electrode. The working electrodes were prepared as follows: 10 mg of Mo_2B_5 powder was dispersed in 200 µl DI water, 1000 µl IPA and 20 µl Nafion solution. Then, the solution was sprayed on a carbon sheet (2×2 cm^2). The sprayed carbon sheet was dried overnight at 50 °C in an oven. The catalyst loading was about 0.6-0.7 mg/cm^2.

The activity of the hydrogen evolution reaction was tested using linear sweep voltammetry (LSV) within -1.0 to 0 V at scan rate 1 mV/s and the electrochemical stability of the catalyst

was tested by cyclic voltammetry (CV) at scan rate 100 mV/s for 2000 cycles. The potentials were calibrated to the reversible hydrogen electrode (RHE), $E_{RHE} = E_{SCE} + 0.242$ V + 0.059pH. An *iR*-drop (iR_Ω) correction was applied using the following equation:

$$E_{iR\text{-corrected}} = E_{RHE} - iR_\Omega$$

The electrochemically active surface area of the sample was estimated from CV measurements at various scan rates (40, 60, 80 mV/s, etc.). The CV measurements were carried out in the region of 0.1 – 0.2 V vs. RHE. The double layer capacitance was estimated by plotting the ΔJ (J_a-J_c) at 0.15 V vs. RHE against the scan rate.

Electrochemical impedance spectroscopy (EIS) was performed at different overpotentials (η=0 and 200 mV) in the frequency range of 100 kHz to 100 mHz under the amplitude of 10 mV.

Computational details

Density functional theory (DFT) calculations were applied to evaluate the hydrogen (H)-surface binding energy ΔE_H on Mo-, flat and puckered B-terminated Mo_2B_4. The calculated β-MoB_2 surfaces correspond to the layers perpendicular to the [001] direction. Two Mo-surfaces are considered here, one is on top of the flat B layer (Mo1 surface) while the other one is on top of the puckered B layer (Mo2 surface). Total energy calculations were performed using the projector augmented wave (PAW) method of Blöchl[26-27] coded in the Vienna ab initio simulation package (VASP).[28] All VASP calculations employed the generalized gradient approximation (GGA) with exchange and correlation treated by the Perdew-Burke-Enzerhoff (PBE) and revised PBE (revPBE) functional, respectively, for

structure relaxation and single energy calculations.[29-30] The convergence threshold for structural relaxation was set to be 0.02 eV/Å in force. The cutoff energy for the plane wave calculations was set to 500 eV and the Brillouin zone integrations were carried out using a $9 \times 9 \times 1$ k-point mesh for all the surfaces. (2×2) surface supercells were constructed by cleaving the bulk β-MoB_2 structure along (001) surface into two dimensional (2D) slabs with a vacuum of ~20 Å between slabs to avoid inter-slab interactions. The resulting 2D slab contains three flat B layers, three puckered B layers and six Mo layers, with four Mo and eight B atoms in each Mo and B layer, respectively. The hydrogen coverage (H coverage) on each surface was calculated by dividing the number of H atoms adsorbed on the surface by the number of Mo atoms (or half the number of B atoms) in a single layer. Gibbs free energy (ΔG_H) for H adsorption was calculated using the equation $\Delta G_H = \Delta E_H + \Delta E_{ZPE} - T\Delta S$, where ΔE_H is the H-surface binding energy, ΔE_{ZPE} is the zero-point energy difference between adsorbed H and free H_2 (ΔE_{ZPE} is usually very small, from 0.01 eV to 0.05 eV, hence neglected here).[7-8] $T\Delta S$ is obtained by $T\Delta S \approx -1/2\ TS^0(H_2)$, where $S^0(H_2) = 130.7\ J \cdot mol^{-1}K^{-1}$ is the entropy of H_2 in the gas phase at standard conditions.[9] ΔE_H, which is the binding energy of H on the surface, can be calculated from the equation $\Delta E_H = E[\text{surface} + n\text{H}] - E[\text{surface} + (n-1)\text{H}] - 1/2\ E[H_2]$, where $E[H_2]$ is the total energy of a gas phase H_2 molecule, $E[\text{surface} + n\text{H}]$ and $E[\text{surface} + (n-1)\text{H}]$ represent the total energy of n and $(n-1)$ hydrogen atoms adsorbed on the surface, respectively.

3.3. Results and discussion

The chemical composition and structure of β-MoB_2 (known since 1947 as "Mo_2B_{5-x}", see phase diagram, **Figure 3.1a**)[31] were revised ten years ago using neutron and synchrotron data,[32] and later (2013) confirmed by theoretical calculations.[33] Its structure contains two types of boron layers; a flat graphene-like layer and a corrugated layer (like the recently discovered phosphorene layer)[25] build of cyclohexane-like arm-chair motifs. Furthermore, the B-layers alternate with Mo-layers along the [001] direction (**Figure 3.1c**). This structural arrangement is similar to that of the highly HER active α-MoB_2, the only difference being the absence of the corrugated B-layer in α-MoB_2.

Recently, the two modifications of α-MoB and β-MoB were found to have similar HER activity in the bulk, which could have been expected because the boron subunits (zigzag chains) are the same, the difference being just their orientations.[17] This finding indicates that the structure-activity relationship concept may apply to these borides. Consequently, this would suggest that β-MoB_2 may also have a significantly high activity because of its structural similarity with highly active bulk α-MoB_2. However, the presence of puckered B-layers complicates a reliable activity prediction by the structure-activity relationship (as made in the MoB case). Thus, theoretical calculations will be key to understand the catalytic behavior and contribution of the different boron layers to the HER activity of this new candidate material for HER.

The synthesis of bulk β-MoB_2 has been a great challenge that was addressed over several decades.[34] The most recent procedure by Albert *et al.*[32] illustrates quite well the tenuous process towards high quality samples. They heated an elemental mixture (2Mo:4B) in

quartz ampoules at 1100 ℃ in Ar atmosphere for 14 days, followed by intermediate grinding and re-pelleting. Then, they heated the resulting sample again at 1300 ℃ in Ta crucible in flowing Ar for 3 days. [32] Using a Sn flux, we have now synthesized single-phase samples of β-MoB_2 in a single step at 1100 ℃. We take advantage of the fact that the molten metal flux (Sn melts at 232 ℃) facilitates diffusion of the elements in the molten mixture and that Sn does not form any stable binary boride. In addition, Sn can be easily removed afterwards by dissolving it in hydrochloric acid. This method has been used very effectively to prepare several classes of materials including borides, carbides and intermetallics, just to name a few.[35,36] The other advantage of tin flux synthesis is that smaller particles are obtained without grinding compared to samples obtained by arc melting.

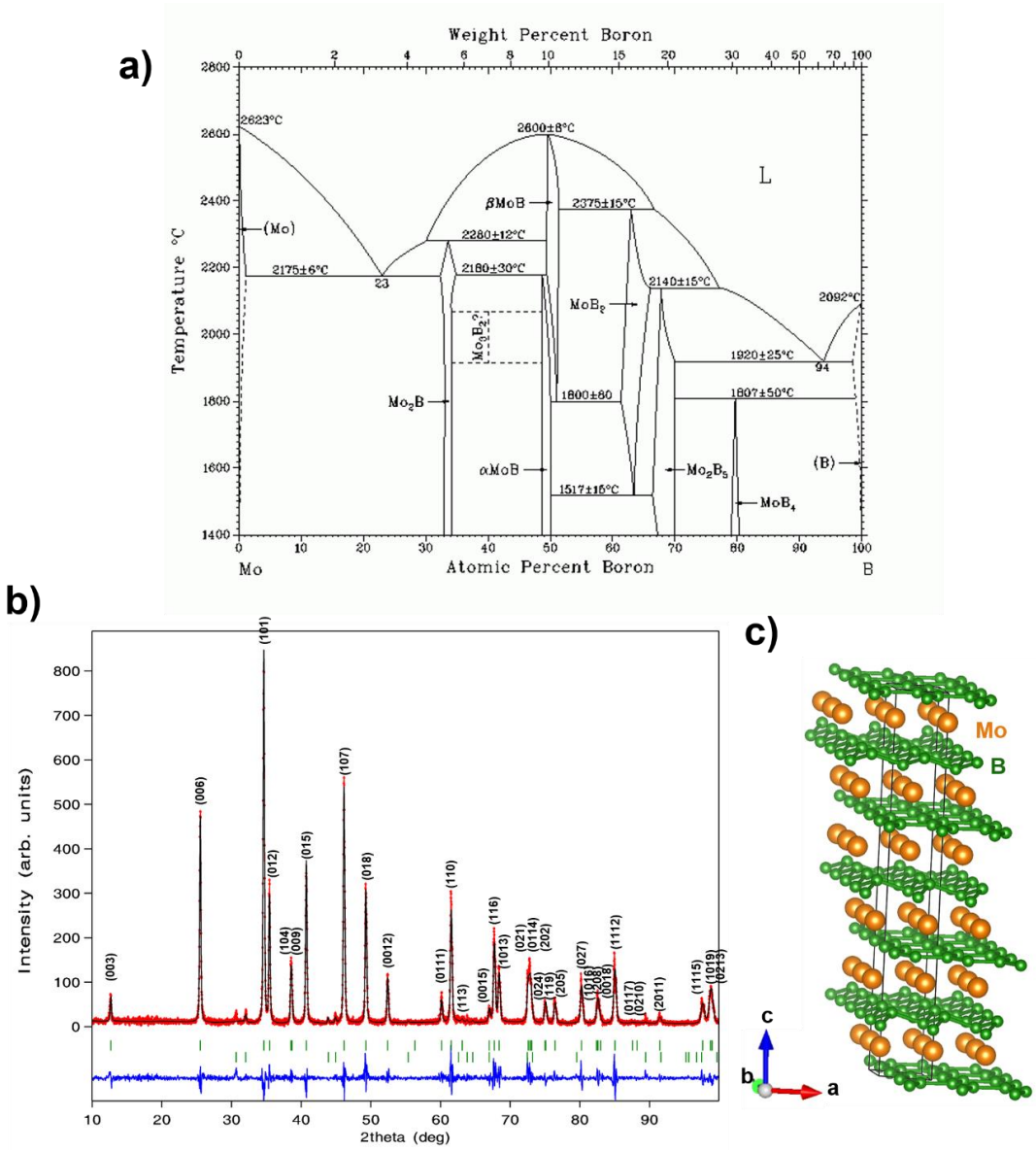

Figure 3.1. a) Binary phase diagram of the molybdenum-boron system, [37] b) Refined powder X-ray diffraction data of β-MoB_2 showing the measured (red) and calculated (black) intensities, the difference plot (blue) and the reflection positions (green, β-MoB_2: top and Sn: bottom). The crystallographic lattice planes are also shown. c) Crystal structure of β-MoB_2 showing two types of boron layers alternating along [001].

Table 3.1. Crystallographic information for the studied molybdenum boride, Mo_2B_4. Reported lattice parameters are given in square brackets.[38]

Phase	β-MoB_2
Crystal system	Trigonal
Space group	*R-3mH*
a [Å]	3.012(3)-[3.010]
c [Å]	20.932(3)-[20.926]
V [$Å^3$]	164.41(2)-[164.19]
Calc. density [g/cm^3]	7.229
Impurity phase (wt.-%)	Sn (0.8)

The morphology of β-MoB_2, analyzed by SEM, indicates irregular particle shapes and a broad size distribution ranging from 1 to 10 μm (**Figure 3.2a**). EDS semi-quantitative analysis (**Figure 3.2b**) confirmed the presence of Mo and B as well as the undissolved Sn impurity (0.8 %). The measured Brunauer–Emmett–Teller (BET) surface area (**Figure 3.3**) of 20.45 m^2/g is about 5 times larger than for bulk α-MoB_2 obtained by arc melting (4.23 m^2/g),[17] probably due to the smaller average particle size of the β-MoB_2 sample.

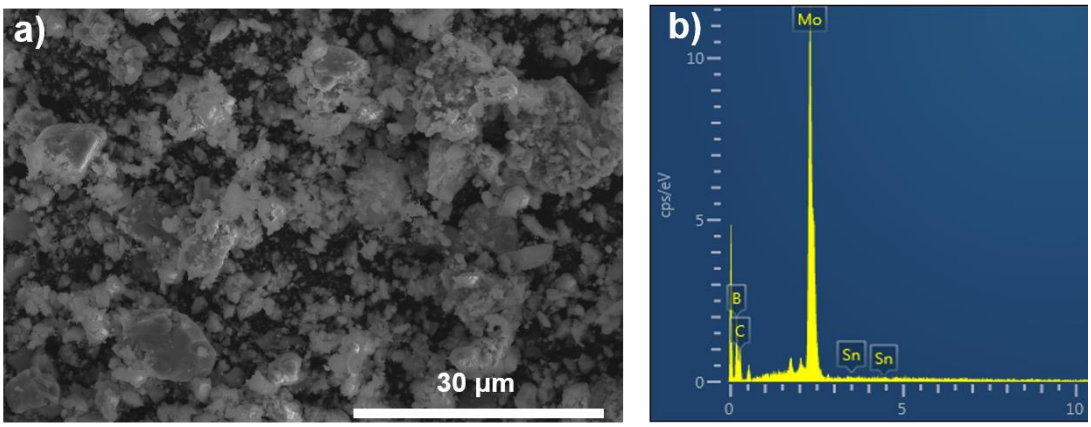

Figure 3.2. a) SEM image of β-MoB_2 and b) EDS spectra of β-MoB_2. The carbon peak is from carbon tape. C is from carbon paste support and Sn is from undissolved tin.

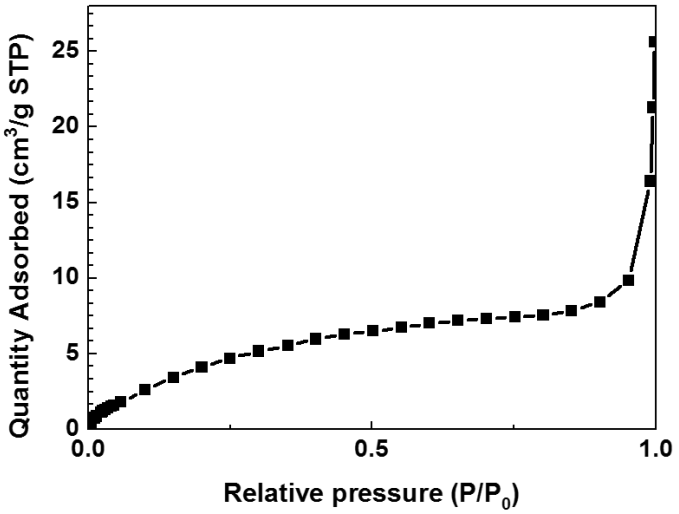

Figure 3.3. BET adsorption isotherm of β-MoB_2 (20.45 m^2/g).

Figure 3.4a, b displays the Mo 3d and B 1s core level XPS spectra of the β-MoB_2 surface indicating four different oxidation states of molybdenum (Mo^0, Mo^{3+}, Mo^{4+} and Mo^{6+}), and two for boron (B^0 and B^{3+}). The fitted peak positions (**Table 3.2**) and a full survey XPS spectrum (**Figure 3.4c**) are given in the SI**.** The high oxidized Mo- and B-species belong to minor oxides impurities (MoO_3, MoO_2, Mo_2O_3 and B_2O_3) usually found on the surface of materials when exposed to air. In previous XPS studies on binary molybdenum borides, it was shown that the freshly prepared materials are less contaminated by oxides, indicating that oxidation occurs as the samples are exposed to air. [17] Similarly, in our freshly prepared β-MoB_2 sample, the oxide peaks are smaller than those found in commercial α-MoB. [16] The presence of an oxide layer has been found on the surfaces of many molybdenum-based materials, but they do not affect their HER activity, because those oxides are dissolved during the first operation cycle in acidic media.[16]

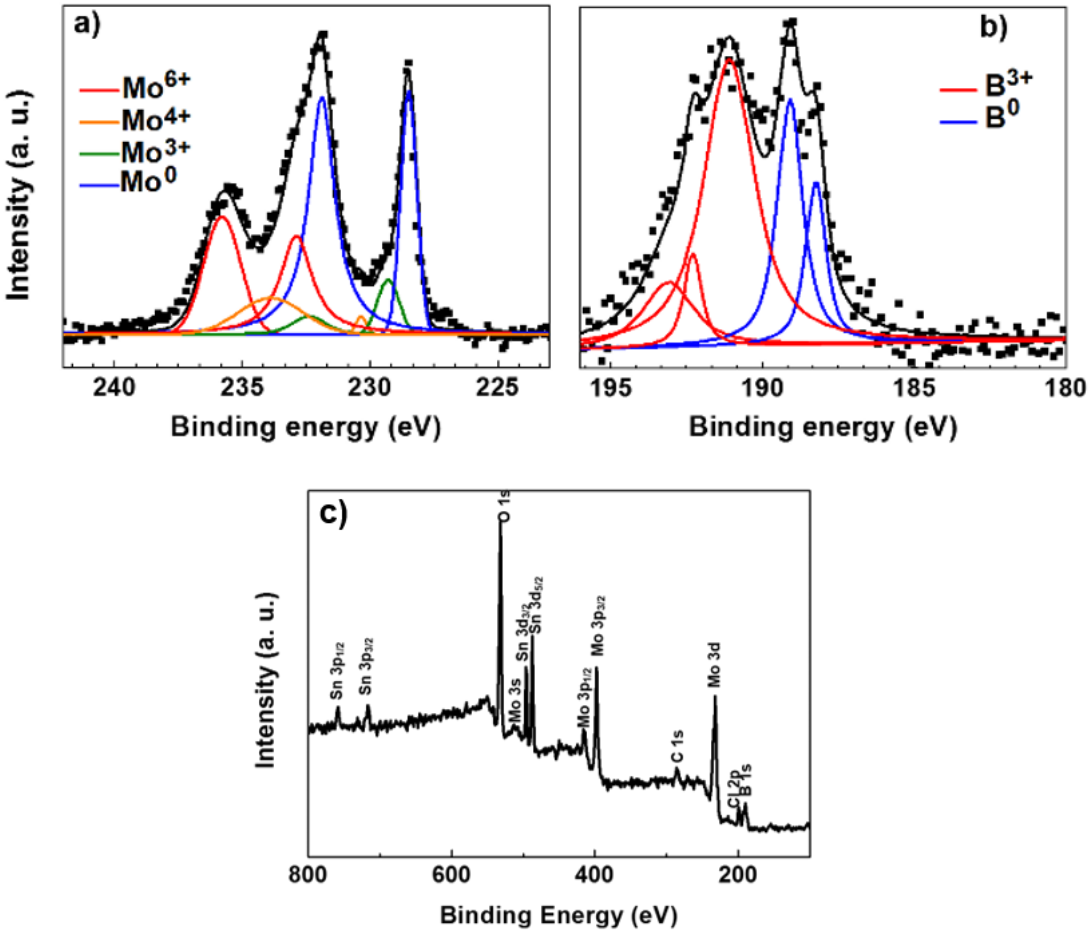

Figure 3.4. XPS spectra of β-MoB_2: Mo 3d a) and B 1s b). Experimental data (■), fitting peaks (black line). (left) MoO_3 (red), MoO_2 (orange), Mo_2O_3 (green) and Mo peaks from the molybdenum boride (blue); (a) B_2O_3 (red) and B (blue) peaks from the molybdenum boride. c) Survey XPS spectrum of β-MoB_2

Table 3.2. XPS parameters (peak position and full width at half maximum (FWHM)) for Mo 3d and B 1s of β-MoB_2.[16, 22]

Phase	Species	Peak position (eV)	FWHM (eV)
β-MoB_2	Mo^0	228.5, 231.9	0.75, 1.25
	Mo^{3+}	229.3, 232.4	1, 1.61
	Mo^{4+}	230.36, 233.9	0.5, 3
	Mo^{6+}	232.9, 235.8	1.5, 1.7
	B^0	188.2, 189.1	0.8, 1
	B^{3+}	191.1, 192.3, 193.1	2, 0.7, 1

The electrochemical activities of β-MoB_2, Pt on carbon (Pt/C), carbon sheet, molybdenum and amorphous boron were measured using a three-electrode system in a 0.5 M H_2SO_4 solution at a scan rate of 1 mV/s under IR drop compensation (**Figure 3.5a**). The polarization curves indicate that the carbon sheet exhibits no activity, while Pt/C shows the highest activity, as expected, with an overpotential value similar to that reported in the literature, while molybdenum is more active than amorphous boron, but both have poor HER activities. The overpotential (270 mV at 3.5 mA/cm^2 current density) of β-MoB_2 is comparable to that of the best bulk molybdenum boride found so far at similar loading, α-MoB_2 (260 mV at 3.5 mA/cm^2 current density).[17] At first sight, this result seems logical, because the two phases have the same composition, but the 5-times larger surface area of β-MoB_2 must be considered in the final evaluation of its catalytic activity, as found recently for the two modifications of MoB.[17] However, the crystal structures of α-MoB and β-MoB

are very similar as they contain the same type of boron and molybdenum substructures (just different orientations), thus they are expected to have similar active sites. On the contrary, the crystal structures of α-MoB_2 and β-MoB_2 have one key difference: While α-MoB_2 contains only graphene-like boron layers, β-MoB_2 contains an additional puckered (phosphorene-like) boron layer. Therefore, there is a possibility to have different active sites for these two structures.

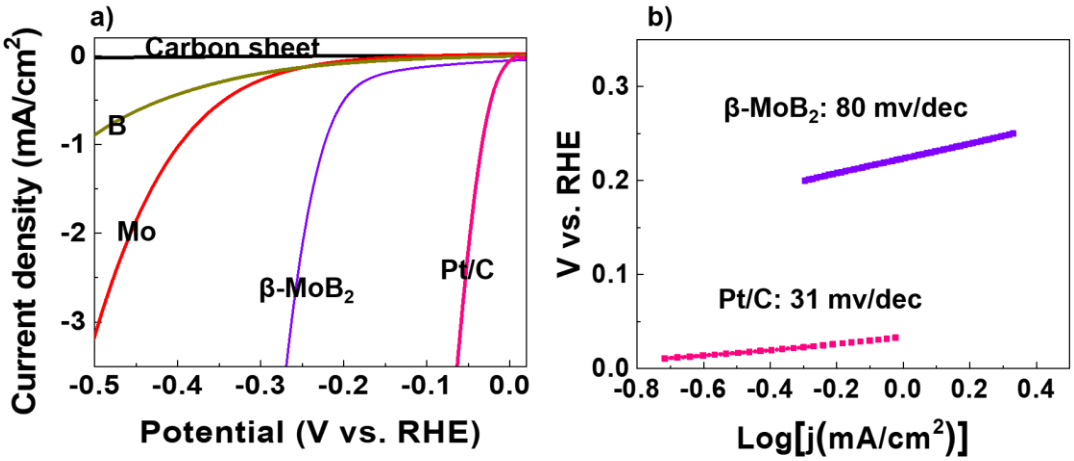

Figure 3.5. a) Polarization curves for amorphous B, Mo, β-MoB_2 and Pt/C in 0.5 M H_2SO_4. b) The corresponding Tafel plot of β-MoB_2 and Pt/C. Scan rate is 1 mV/s.

The electrochemically active surface area (ECSA) was estimated by the double layer capacitance measurement through cyclic voltammetry (CV) at various scan rates (between 0.1 and 0.2 V vs. RHE, **Figure 3.6a, b**). [39-40] The obtained double layer capacitance of bulk β-MoB_2 (156 μF/cm^2) is significantly larger than that of bulk α-MoB_2 (101 μF/cm^2). However, as shown above, the overpotential obtained for β-MoB_2 is comparable to that of MoB_2. The fact that β-MoB_2 has a 5-times larger surface area than α-MoB_2 shows that it has less active sites per unit surface area than α-MoB_2, which indicates that the different

boron layers found in the β-MoB_2 structure may have different activities. Indeed, our density functional theory (DFT) calculations suggest that the graphene-like boron layer is by far more active than the phosphorene-like boron layer.

Figure 3.6c shows the electrochemical impedance spectra of β-MoB_2 performed at an overpotential of 0 and 200 mV vs. RHE. The electrochemical cell can be generally analyzed using an Randles circuit model (inset **Figure 3.6c bottom right**).[24] R_s is the solution resistance, C_{dl} is the double layer capacitance and R_{ct} is the charge transfer resistance. R_s and R_{ct} are usually calculated from a Nyquist plot. At η = 200 mV, we can observe well defined semicircle (inset **Figure 3.6c top right**) and we can calculate R_s (6.27) and Rct (45.98) at η = 200 mV.

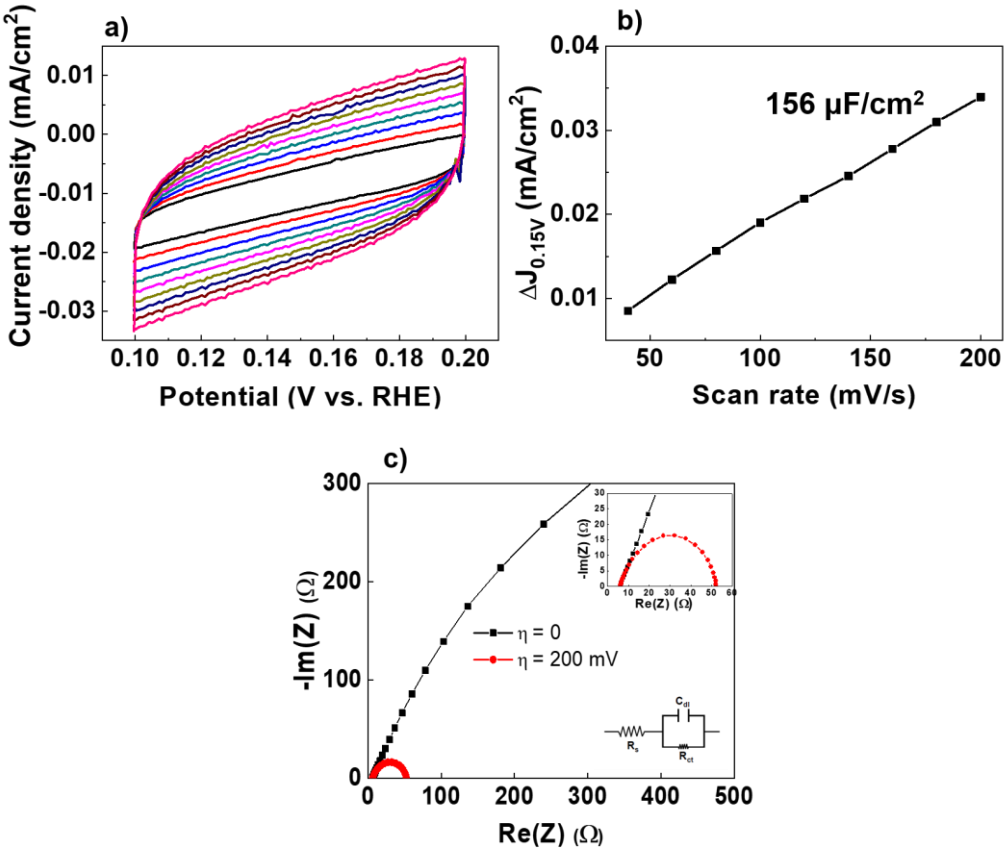

Figure 3.6. a) Cyclic voltammetry curves of β-MoB_2. b) The difference current density ΔJ (J_a-J_c) at 1.5 V vs. RHE plotted against the scan rate is fitted to a linear regression to estimate C_{dl}. c) Electrochemical impedance spectra of β-MoB_2 at different overpotential in 0.5 M H2SO4 (Rs (6.27) and Rct (45.98) at η = 200 mV).

The HER mechanism of β-MoB_2 was probed by the Tafel analysis (**Figure 3.5b**). In acidic solution, three reactions are considered as the rate determining step (RDS); the Volmer reaction (Tafel slope of ~120 mV/dec), the Heyrovsky reaction (Tafel slope of ~40 mV/dec) and the Tafel reaction (Tafel slope of ~30 mV/dec).[41-44] As **Figure 3.5b** shows, the obtained Tafel slope for Pt/C is ~31 mV/dec, indicating that the RDS for Pt/C is the Tafel reaction, which is consistent with previous studies.[12, 41] The Tafel slope of β-MoB_2 (80 mV/dec) does not match exactly any of the ideal Tafel slopes, but it is close to that

found for α-MoB_2 (75 mV/dec). Like all other molybdenum borides studied until now, it is difficult to determine the RDS using the Tafel analysis in the current system. This finding suggests that the HER mechanism may be more complex for this class of active bulk materials than for nanoscale materials and Pt/C.[45-46]

Stability is also a key factor for a good HER catalyst. To evaluate stability, we have performed CV experiments in acid solution (**Figure 3.7**). After 2000 cycles, the activity of β-MoB_2 is nearly as good as initial, indicating that the synthesized β-MoB_2 sample has good stability in acidic solution.

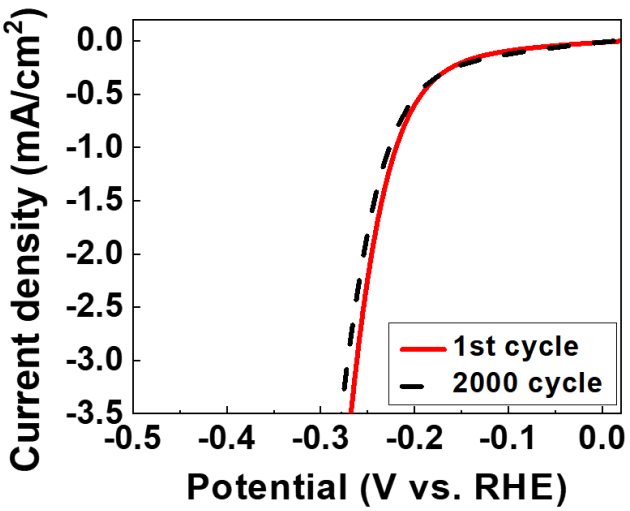

Figure 3.7. Stability measurements of β-MoB_2 after 2000 cycles in 0.5 M H_2SO_4. Scan rate is 100 mV/s.

To investigate the above-suggested different activities of the two boron layers present in the structure of β-MoB_2, we have calculated the Gibbs free energy (ΔG_H) for H adsorption on different surfaces (including molybdenum surfaces) by DFT calculations. The calculated β-MoB_2 surfaces correspond to the layers perpendicular to the [001] direction (**Figure 3.1c**). Because we have a polycrystalline sample, we expect all facets found in XRD (**Figure 3.1b**) to be present, including the B- and Mo-layers ({00n} planes with n = 3, 6, ...). ΔG_H is commonly used and widely accepted as a descriptor of the HER activity.[12, 47-50] An optimal HER activity can be achieved at a ΔG_H value close to zero, and under this condition the overall reaction of both H adsorption and H_2 desorption has the maximum rate. [47] The bonding energy of H on the surface (ΔE_H) and ΔG_H were calculated for four different surfaces (Mo1-, Mo2-, flat B- and puckered B-terminated surfaces) at 25% H coverage to determine the preferred adsorption sites on each surface (see section III and **Table 3.3** in the SI for more details). Three types of adsorption sites were considered: on top (T) of a Mo or B atom, on a Mo−Mo or B−B bridge site (Bg) and on a hollow (Ho) site. There are two top sites (T1: on top of the outer boron, and T2: on top of the inner boron) for the puckered phosphorene-like B surface (see SI, **Figure 3.8**). As shown in **Table 3.3** for 25% H coverage, the Ho site of the Mo1 surface, the Bg site of the Mo2 and flat B surfaces, and one of the top (T1) sites of the puckered B surface are the most preferred adsorption sites, because of their high surface binding energy. H binds much stronger on the puckered B layer (−0.81 and −1.14 eV on the Bg and T1 sites, respectively) than on the flat B layer (−0.53 and −0.42 eV on the Bg and T site, respectively). However, this strong binding also makes the puckered B layer less active for the HER than the flat B layer. In

fact, the ΔE_H value obtained for the flat B layer is close to that calculated for Pt (111), hinting at the possible strong activity of this site. The two Mo layers also bind with H, but not as strongly as the puckered B layer, an indication of moderate catalytic activity. In addition, ΔG_H was examined at different H coverages for the preferred adsorption sites of all Mo- and B-terminated surfaces. The ΔG_H values obtained for different H coverages for the two Mo and two B layers are listed in the **Table 3.4** and plotted in **Figure 3.9a**. ΔG_H increases as H coverage increases on both the Bg and T sites of the flat B layer and reaches zero at around 50% H coverage for both sites. Therefore, both the Bg and T sites of the flat B layer should be very active for HER. Beside the fact that the puckered B layer binds strongly with H at 25% H coverage, the variation of ΔG_H with increasing H coverage up to 100% never leads to a ΔG_H value of 0, indicating that the puckered B layer performs very poorly for the HER. ΔG_H for the two Mo surfaces (**Figure 3.9a**), behaves similarly to that of the puckered T1 site of the B layer, indicating similar activity. The ΔG_H diagram plotted at 50% coverage **(Figure 3.9b**) indicates that the graphene-like B layers are the most active, followed by the molybdenum layers and lastly the phosphorene-like B layers. This theoretical result confirms and even extends the experimental finding that β-MoB_2 has less active sites per surface area than α-MoB_2, because 50% of the highly active flat graphene-like B layers have been traded for the less active puckered phosphorene-like layers, thus reducing its HER activity. Nevertheless, β-MoB_2 has compensated its lack of active sites by a 5-times increase of its surface area achieved through the Sn-flux synthetic method.

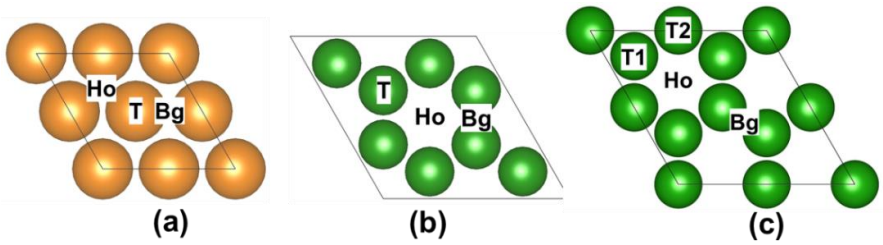

Figure 3.8. H adsorption site on (a) Mo1 and Mo2 surface, (b) flat B surface, (c) puckered B surface. T, Bg and Ho represents the top, the bridge and the hollow sites, respectively. Mo and B atoms are indicated by orange and green spheres, respectively. There are two top sites for the puckered B layer: the one on top of the outer B (T1) and the one on top of the inner B (T2).

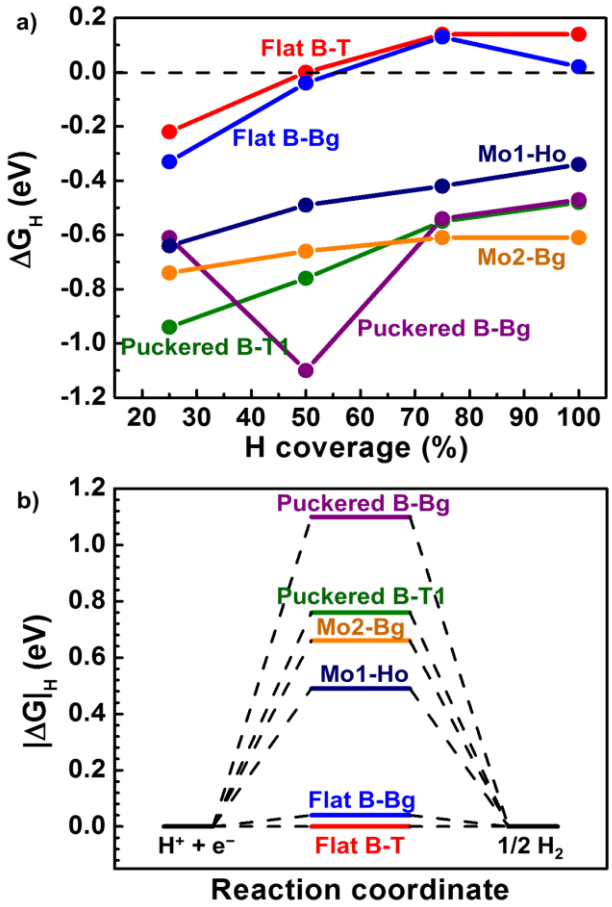

Figure 3.9. a) The Gibbs free energy (ΔG_H) for H adsorption on different surfaces plotted as a function of hydrogen coverage. b) Calculated free-energy diagram for HER over different surfaces at 50% H coverage.

Table 3.3. Calculated binding energy (ΔE_H) and Gibbs free energy (ΔG_H) of single H (**25% H coverage**) adsorption on Mo1-, Mo2-, flat and puckered B-terminated β-MoB_2 surfaces. The β-MoB_2 surfaces correspond to the layers perpendicular to the [001] direction. Values on Pt (111) surface are calculated for comparison.

Binding site	**Top (T)**		**Bridge (Bg)**		**Hollow (Ho)**	
	ΔE_H (eV)	**ΔG_H (eV)**	**ΔE_H (eV)**	**ΔG_H (eV)**	**ΔE_H (eV)**	**ΔG_H (eV)**
Mo1	−0.29	−0.09	−0.71	−0.51	−0.84	−0.64
Mo2	+0.37	+0.57	−0.94	−0.74	−0.76	−0.56
Flat B	−0.42	−0.22	−0.53	−0.33	+1.36	+1.56
Puckered B	−1.14 (T1)	−0.94 (T1)	−0.81	−0.61	+0.68	+0.88
	+0.15 (T2)	+0.35 (T2)				
Pt (111)	−0.41	−0.21	−0.32	−0.12	−0.33	−0.13

Table 3.4. Calculated Gibbs free energy (ΔG_H) of H adsorption on different surfaces: Bridge (Bg) and top (T) sites of the flat and puckered B-terminated β-MoB_2 surfaces, as well as Mo1 and Mo2 surfaces at different H coverages. The β-MoB_2 surfaces correspond to the layers perpendicular to the [001] direction. Bold values indicate the ΔG_H window enclosing $\Delta G_H = 0$.

H coverage	Gibbs free energy (ΔG_H) / eV					
	Flat B (Bg)	Flat B (T)	Puckered B (Bg)	Puckered B (T1)	Mo1 (Ho)	Mo2 (Bg)
25%	−0.33	−0.22	−0.61	−0.94	−0.64	−0.74
50%	**−0.04**	**0.00**	−1.10	−0.76	−0.49	−0.66
75%	**+0.13**	+0.14	−0.54	−0.55	−0.42	−0.61
100%	+0.02	+0.14	−0.47	−0.48	−0.34	−0.61

3.4. Conclusion

In conclusion, single-phase bulk β-MoB_2 has been successfully synthesized by the tin flux method for the first time. Electrochemical characterizations show that this phase is among the best bulk HER catalysts in acidic conditions and it also shows excellent stability. As found by DFT free energy calculations, the active sites in the graphene-like B layer contribute to the high HER activity, in contrast to the phosphorene-like B layer which is found to be far less active, while the Mo layers are moderately active.

References

1. Turner, J. A., *Science* **2004,** *305*, 972.
2. Lewis, N. S.; Nocera, D. G., *Prog. Nat. Acad. Sci.* **2006,** *103*, 15729.
3. Wang, J.; Cui, W.; Liu, Q.; Xing, Z.; Asiri, A. M.; Sun, X., *Adv. Mater.* **2016,** *28*, 215.
4. Morales-Guio, C. G.; Stern, L.-A.; Hu, X., *Chem. Soc. Rev.* **2014,** *43*, 6555.
5. Kibler, L. A., *ChemPhysChem* **2006,** *7*, 985.
6. Subbaraman, R.; Tripkovic, D.; Strmcnik, D.; Chang, K. C.; Uchimura, M.; Paulikas, A. P.; Stamenkovic, V.; Markovic, N. M., *Science* **2011,** *334*, 1256.
7. Vesborg, P. C.; Jaramillo, T. F., *Rsc Advances* **2012,** *2*, 7933.
8. Hinnemann, B.; Moses, P. G.; Bonde, J.; Jørgensen, K. P.; Nielsen, J. H.; Horch, S.; Chorkendorff, I.; Nørskov, J. K., *J. Am. Chem. Soc.* **2005,** *127*, 5308.
9. Jaramillo, T. F.; Jørgensen, K. P.; Bonde, J.; Nielsen, J. H.; Horch, S.; Chorkendorff, I., *Science* **2007,** *317*, 100.
10. Chen, W. F.; Muckerman, J. T.; Fujita, E., *Chem. Commun.* **2013,** *49*, 8896.
11. Chen, W. F.; Sasaki, K.; Ma, C.; Frenkel, A. I.; Marinkovic, N.; Muckerman, J. T.; Zhu, Y.; Adzic, R. R., *Angew. Chem. Int. Ed.* **2012,** *51*, 6131.
12. Xiao, P.; Sk, M. A.; Thia, L.; Ge, X.; Lim, R. J.; Wang, J.-Y.; Lim, K. H.; Wang, X., *Energy Environ. Sci.* **2014,** *7*, 2624.
13. Huang, Z.; Chen, Z.; Chen, Z.; Lv, C.; Humphrey, M. G.; Zhang, C., *Nano Energy* **2014,** *9*, 373.
14. Michalsky, R.; Zhang, Y. J.; Peterson, A. A., *ACS Catal.* **2014,** *4*, 1274.
15. Liao, L.; Wang, S.; Xiao, J.; Bian, X.; Zhang, Y.; Scanlon, M. D.; Hu, X.; Tang, Y.; Liu, B.; Girault, H. H., *Energy Environ. Sci.* **2014,** *7*, 387.
16. Vrubel, H.; Hu, X., *Angew. Chem. Int. Ed.* **2012,** *51*, 12703.
17. Park, H.; Encinas, A.; Scheifers, J. P.; Zhang, Y.; Fokwa, B., *Angew. Chem. Int. Ed.* **2017,** *56*, 5575.
18. Gupta, S.; Patel, N.; Miotello, A.; Kothari, D., *J. Power Sources* **2015,** *279*, 620.
19. Xu, N.; Cao, G.; Chen, Z.; Kang, Q.; Dai, H.; Wang, P., *J. Mater. Chem. A* **2017,** *5*, 12379.
20. Sitler, S. J.; Raja, K. S.; Charit, I., *J. Electrochem. Soc.* **2016,** *163*, H1069.
21. Das, R. K.; Wang, Y.; Vasilyeva, S. V.; Donoghue, E.; Pucher, I.; Kamenov, G.; Cheng, H.-P.; Rinzler, A. G., *ACS nano* **2014,** *8*, 8447.
22. Wan, C.; Regmi, Y. N.; Leonard, B. M., *Angew. Chem. Int. Ed.* **2014,** *53*, 6407.
23. Tang, C.; Sun, A.; Xu, Y.; Wu, Z.; Wang, D., *J. Power Sources* **2015,** *296*, 18.
24. Chen, Z.; Cummins, D.; Reinecke, B. N.; Clark, E.; Sunkara, M. K.; Jaramillo, T. F., *Nano Lett.* **2011,** *11*, 4168.
25. Wu, H. B.; Xia, B. Y.; Yu, L.; Yu, X.-Y.; Lou, X. W. D., *Nat. Commun.* **2015,** *6*.
26. Blöchl, P. E., *Physical review B* **1994,** *50*, 17953.
27. Kresse, G.; Joubert, D., *Physical Review B* **1999,** *59*, 1758.
28. Kresse, G.; Furthmüller, J., *Physical review B* **1996,** *54*, 11169.
29. Perdew, J. P.; Burke, K.; Ernzerhof, M., *Phys. Rev. Lett.* **1996,** *77*, 3865.
30. Hammer, B.; Hansen, L. B.; Nørskov, J. K., *Physical Review B* **1999,** *59*, 7413.

31. Kiessling, R.; Wetterholm, A.; Sillén, L. G.; Linnasalmi, A.; Laukkanen, P., *Acta Chem. Scand* **1947,** *1*, 893.
32. Frotscher, M.; Klein, W.; Bauer, J.; Fang, C. M.; Halet, J. F.; Senyshyn, A.; Baehtz, C.; Albert, B., *Z. Anorg. Allg. Chem.* **2007,** *633*, 2626.
33. Hayami, W.; Momozawa, A.; Otani, S., *Inorg. Chem.* **2013,** *52*, 7573.
34. Klesnar, H.; Aselage, T.; Morosin, B.; Kwei, G., *J. Alloys Compd.* **1996,** *241*, 180.
35. Benbow, E. M.; Latturner, S. E., *J. Solid State Chem.* **2006,** *179*, 3989.
36. Kanatzidis, M. G.; Pöttgen, R.; Jeitschko, W., *Angew. Chem. Int. Ed.* **2005,** *44*, 6996.
37. Brewer, L., *International Atomic Energy Authority* **1980**, 714.
38. Shein, I.; Shein, K.; Ivanovskii, A., *Physica B Condens Matter* **2007,** *387*, 184.
39. Xie, J.; Zhang, J.; Li, S.; Grote, F.; Zhang, X.; Zhang, H.; Wang, R.; Lei, Y.; Pan, B.; Xie, Y., *J. Am. Chem. Soc.* **2013,** *135*, 17881.
40. Lukowski, M. A.; Daniel, A. S.; Meng, F.; Forticaux, A.; Li, L.; Jin, S., *J. Am. Chem. Soc.* **2013,** *135*, 10274.
41. Li, Y.; Wang, H.; Xie, L.; Liang, Y.; Hong, G.; Dai, H., *J. Am. Chem. Soc.* **2011,** *133*, 7296.
42. Ji, S.; Yang, Z.; Zhang, C.; Liu, Z.; Tjiu, W. W.; Phang, I. Y.; Zhang, Z.; Pan, J.; Liu, T., *Electrochim. Acta* **2013,** *109*, 269.
43. Tang, Y. J.; Gao, M. R.; Liu, C. H.; Li, S. L.; Jiang, H. L.; Lan, Y. Q.; Han, M.; Yu, S. H., *Angew. Chem. Int. Ed.* **2015,** *54*, 12928.
44. Chung, D. Y.; Park, S. K.; Chung, Y. H.; Yu, S. H.; Lim, D. H.; Jung, N.; Ham, H. C.; Park, H. Y.; Piao, Y.; Yoo, S. J., *Nanoscale* **2014,** *6*, 2131.
45. Kibsgaard, J.; Chen, Z.; Reinecke, B. N.; Jaramillo, T. F., *Nat. Mater.* **2012,** *11*, 963.
46. Huang, Y.; Gong, Q.; Song, X.; Feng, K.; Nie, K.; Zhao, F.; Wang, Y.; Zeng, M.; Zhong, J.; Li, Y., *ACS nano* **2016,** *10*, 11337.
47. Zheng, Y.; Jiao, Y.; Jaroniec, M.; Qiao, S. Z., *Angew. Chem. Int. Ed.* **2015,** *54*, 52.
48. Skffllason, E.; Tripkovic, V.; Björçrketun, M., *J. Phys. Chem. C* **2010,** *114*, 18182.
49. Tang, Q.; Jiang, D.-e., *ACS Catal.* **2016,** *6*, 4953.
50. Atkins, P. W., *Physical chemistry 3rd ed.* Freeman and Company: New York: 1985.

Chapter 4

Designing highly active high current density HER electrocatalysts: Graphene-like boron layer and tungsten as key ingredients in metal diborides

4.1. Introduction

Electrochemical water splitting has emerged as a clean and efficient technology to produce hydrogen through the hydrogen evolution reaction (HER). [1-2] Up to the present, noble metals such as platinum are considered as state-of-the-art electrocatalyst for HER. Unfortunately, their limited abundance and high cost significantly hinder their large-scale production. [3-5] Therefore, it is urgent to develop cost-effective, highly active and earth-abundant non-noble-metal HER catalysts that can be substitutes of precious metals. [6-7] In the past few years, non-noble-metal-based electrocatalysts such as phosphides[7-8], sulfides[9-10], nitrides[11-12], carbides[13-14] and metal alloys[15-16] were shown to have outstanding electrocatalytic performance. Among these materials, transition metal borides such as Mo-B (bulk, nanoscale)[17-21], FeB_2 (nanoscale)[22], Co-B (amorphous)[23], Co-Ni-B (amorphous)[24], Ni-B (amorphous)[25], Mo_3B (film)[26], MoAlB (bulk)[27], VB_2 (nanoscale)[28] have drawn considerable attention recently due to their low cost and excellent electrocatalytic activity and stability both in acidic and basic solutions. Among these borides, those containing the flat graphene-like boron layer such as α-MoB_2, FeB_2 and VB_2 have the highest HER activity. The importance of the flatness of the boron layer was studied in β-MoB_2 [19], a modification of α-MoB_2 which shows a mixture of flat (graphene-like) and puckered (phosphorene-like) boron layers. According to DFT free energy calculations the graphene-

like boron layer is greatly HER active whereas the phosphorene-like boron layer has far less activity, indicating that α-MoB_2 would be more active than β-MoB_2. Indeed, experiments concluded that α-MoB_2 was the most efficient catalyst (see also results below). If compared to molybdenum, tungsten-based materials have been far less studied even though the two elements have very similar chemistries and properties. For example, tungsten disulfide[29-30], carbides[31-32] and phosphides[33-34] all exhibit similar or better HER activity as their molybdenum counterparts. However, no tungsten-based borides have been studied so far. α-MoB_2 (AlB_2-type) is the best Mo-based boride HER catalyst, thus its W-based counterpart would be a great target as HER catalyst. AlB_2-type WB_2 has been reported once by Woods et al. in 1966. [35] Otani et al. reexamined this phase and found out that AlB_2-type WB_2 became minimally stable with some boron defects added and they suggested that AlB_2-type WB_2 may not exist. [36] Actually, two modifications of WB_2 are stable but they contain both flat and puckered boron layers, α-WB_2 (β-MoB_2-type, space group *R*-3*mH*, **Figure 4.1a**), and β-WB_2 (space group $P6_3/mmc$, **Figure 4.1c**), indicating that tungsten maybe unfavorable for the stability of the flat boron layers. However, the combination of tungsten and flat boron layer in a phase would have the potential to create the best HER electrocatalyst boride to date.

Herein, we report on the experimental and theoretical investigations of the HER activities of β-WB_2 and α-$Mo_{1-x}W_xB_2$ for the first time. Our results reveal a great synergy between Mo and W toward creating an excellent HER catalyst which works extraordinary well at high current density in acid.

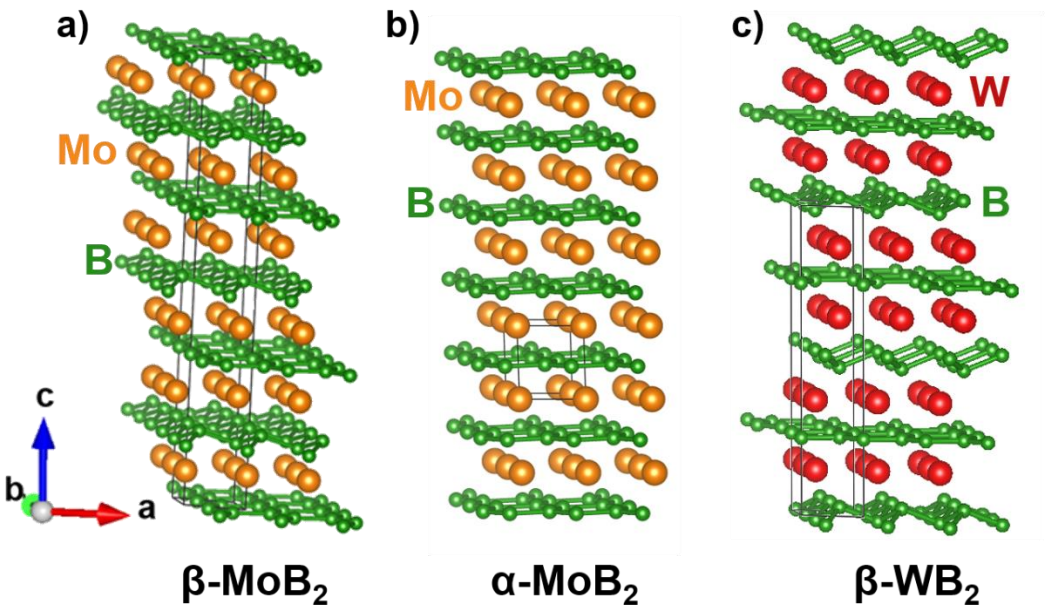

Figure 4.1. Crystal structures of a) β-MoB_2, b) α-MoB_2 and c) β-WB_2 (right) with unit cells represented in gray.

4.2. Experimental section

Synthesis method

α-MoB_2, $Mo_{1-x}W_xB_2$ (x = 0.1, 0.2, 0.3, 0.35, 0.4, 0.45) and β-WB_2

Powders of molybdenum (Mo), boron (B) and tungsten (W) were weighted in appropriate stoichiometric ratios (total mass 0.3 g) and pressed into pellets. The pellets were arc-melted in a water-cooled copper crucible (first electrode) under argon atmosphere by using a tungsten tip as second electrode. The pellet was arc-melted at 60 A in the first step until homogeneous melting occurred. Then, the current was reduced to 40 A and the melting process was repeated 5 times to ensure homogeneity.

β-MoB_2

Powder sample from tin flux synthesis which is reported in our previous paper was pressed into pellets. [19] The pressed sample was arc-melted at 30 A and the procedure was repeated 3 times.

Mo, B and W

Powders of molybdenum (Mo), boron (B) and tungsten (W) were weighted and pressed into pellets ratios (total mass 0.3 g). The pellets were arc-melted at 40 A and the procedure was repeated 3 times

Powder X-ray diffraction (PXRD)

Powder X-ray diffraction patterns of the samples were recorded using a Rigaku Miniflex-600 and operating condition were 40 kV and 15 mA generating Cu K_α radiation (λ=1.5418 Å). The recorded powder X-ray diffractograms were refined by means of the Rietveld method (full-matrix least-squares refinement) as implemented in the FULLPROF program suite.

XPS, SEM and EDX, Mapping

X-ray photoelectron spectroscopy (XPS) was conducted using a Kratos AXIS ULTRA ^{DLD} XPS system equipped with an A1 Kα monochromated X-ray source and a 165 mm mean radius hemispherical electron energy analyzer.

The surface morphology and mapping of the synthesized material were obtained by using scanning electron microscopy (SEM) and energy dispersive X-ray spectroscopy (EDS),

respectively, on a ultra-high-resolution low-energy system Nova NanoSEM450 equipped with a 50mm^2 X-Max50 SD EDX detector.

Electrochemical characterization

The electrochemical catalytic measurements were performed with VSP electrochemical workstation (Bio-Logic VSP, France) in standard three-electrode system using saturated calomel electrode (SCE) as the reference electrode and graphite rod as the counter electrode in 0.5 M H_2SO_4 solution at room temperature.

The working electrodes were prepared as follows: arc-melted samples were put into epoxy glue and dried for 2 days. Top and bottom of the dried samples were grinded using grinder (South Bay Technology). Grinded samples (disk shape) were attached on copper sheet using a conductive silver paste. The exposed surface of copper sheet was covered with epoxy glue, leaving only the top surface exposed (see below).

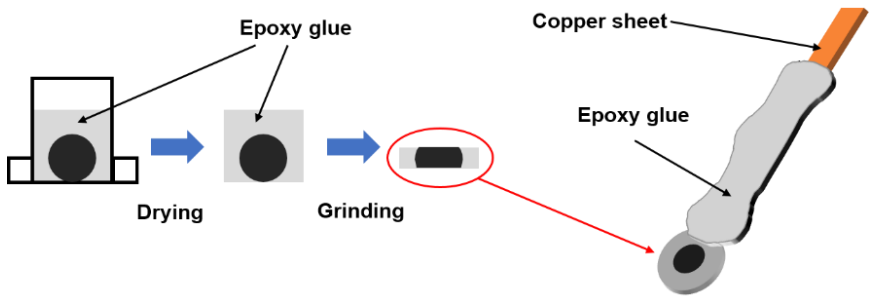

Scheme 4.1. Schematic representation of working electrode preparation.

For the Pt/C electrode, 1 mg of Pt/C powder (20 %) was sonicated in 95 µl IPA and 5 µl Nafion solution. Then, the 7.5 µl of solution was dropwise on a carbon cloth (0.5×0.5 cm^2).

The carbon cloth was dried for 5 h at 50 °C in an oven (the catalyst loading: ~0.3 mg/cm^2). The dried carbon cloth was attached on copper sheet using conductive silver paste and the exposed surface of copper sheet was covered with epoxy adhesive and dried overnight at room temperature.

The polarization curves were collected from linear sweep voltammetry (LSV) within -1.0 to 0 V at scan rate 5 mV/s and the electrochemical stability of the catalyst was measured by cyclic voltammetry (CV) at scan rate 100 mV/s for 5000 cycles.

All the potentials were calibrated to the reversible hydrogen electrode (RHE), $E_{RHE} = E_{SCE} + 0.242\ V + 0.059 \times pH$ and an *iR*-drop (iR_Ω) correction was applied.

The electrochemically active surface area of the sample was estimated from CV measurements at various scan rates (40 -200 mV/s). The CV measurements were carried out in the region of 0.1 – 0.2 V vs. RHE. The double layer capacitance was estimated by plotting the ΔJ (J_a-J_c) at 0.15 V vs. RHE against the scan rate.

Electrochemical impedance spectroscopy (EIS) was performed at overpotentials (η = 200 mV) in the frequency range of 500 kHz to 1 Hz under the amplitude of 10 mV.

Computational details

Density functional theory (DFT) calculations were applied to evaluate the H-surface binding energy ΔE_H on W1-, W2-, flat B- and puckered B-terminated {001} surfaces in β-WB_2, as wells as B- and Mo/W-terminated {001}, mixed Mo/B and Mo/W/B {110} surfaces in α-$Mo_{0.75}W_{0.25}B_2$. Total energy calculations were performed using the projector augmented wave (PAW) method of Blöchl [37-38] coded in the Vienna ab initio simulation

package (VASP). [39] All VASP calculations employed the generalized gradient approximation (GGA) with exchange and correlation treated by the Perdew-Burke-Enzerhoff (PBE) and revised PBE (revPBE) functionals, respectively, for structure relaxation and single energy calculations. [40-41] The convergence threshold for structural relaxation was set to be 0.02 eV/Å in force. The cutoff energy for the plane wave calculations was set to 500 eV and the Brillouin zone integrations were carried out using a $9 \times 9 \times 2$, $9 \times 9 \times 3$ and $7 \times 11 \times 3$ k-point mesh for β-WB_2 {001}, α-$Mo_{0.75}W_{0.25}B_2$ {001} and {110} surfaces, respectively. The surfaces were constructed by cleaving the bulk β-WB_2 and α-$Mo_{0.75}W_{0.25}B_2$ structures into two dimensional (2D) slabs (surface supercells) by choosing the right surface and enough vacuum (more than 13 Å) between slabs to avoid inter-slab interactions. The resulting β-WB_2 2D surface supercell contains five B layers and four W layers for B-terminated surfaces, while four B layers and five W layers for W-terminated surfaces. Each W and B layer has four W and eight B atoms, respectively. The $Mo_{0.75}W_{0.25}B_2$ {001} surface supercell has four metal (M) layers and four B layers, with three Mo and one W in each M layer and eight B in each B layer. Finally, the $Mo_{0.75}W_{0.25}B_2$ {110} supercell hold six [MB_2] layers with alternating [MoB_2] and [($Mo_{0.5}W_{0.5}B_2$] layers. The [MoB_2] layer has four Mo and eight B atoms, while the [($Mo_{0.5}W_{0.5}B_2$] layer contains two Mo, two W and eight B atoms. The hydrogen coverage (H coverage) on each surface was calculated by dividing the number of H atoms adsorbed on the surface by the number of metal atoms (or half the number of B atoms) in a single layer.

Gibbs free energy (ΔG_H) for H adsorption was calculated using the equation $\Delta G_H = \Delta E_H + \Delta E_{ZPE} - T\Delta S$, where ΔE_H is the H-surface binding energy, ΔE_{ZPE} is the zero-point energy

difference between adsorbed H and free H_2 (ΔE_{ZPE} is usually very small, from 0.01 eV to 0.05 eV, hence neglected here).[42-43] $T\Delta S$ is obtained by $T\Delta S \approx -1/2\ TS^0(H_2)$, where $S^0(H_2)$ = 130.7 $J \cdot mol^{-1}K^{-1}$ is the entropy of H_2 in the gas phase at standard conditions.[44] ΔE_H, which is the binding energy of H on the surface, can be calculated from the equation $\Delta E_H = E[\text{surface} + n\text{H}] - E[\text{surface} + (n-1)\text{H}] - 1/2\ E[H_2]$, where $E[H_2]$ is the total energy of a gas phase H_2 molecule, E[surface + nH] and E[surface + (n−1)H] represent the total energy of n and (n−1) hydrogen atoms adsorbed on the surface, respectively.

4.3. Results and discussion

Figure 4.2a depicts the Rietveld refinement plot of the X-ray power diffraction (XRD) pattern of α-$Mo_{0.7}W_{0.3}B_2$ (AlB_2-type) and **Figure** 4.**3** shows the XRD patterns of other phases: α-MoB_2, $Mo_{1-x}W_xB_2$ (x = 0.1, 0.2, 0.35, 0.4, 0.45), β-WB_2 and β-MoB_2. According to these data, all ternary phases were single crystalline phases, while for the $Mo_{1-x}W_xB_2$ solid solution, single phase samples were obtained for $x < 0.35$. For $0.35 \leq x \leq 0.45$, two phase samples were obtained with the main phase α-$Mo_{1-x}W_xB_2$ accompanied by the side phase β-WB_2 (doped with Mo according to Energy dispersive X-ray spectroscopy (EDS) analysis, **Figure 4.2b and 4**). The lattice parameters of α-$Mo_{0.7}W_{0.3}B_2$, a = 3.034 (1) Å and c = 3.064 (2) Å, are only slightly different to the reported values for α-MoB_2 (ICSD No. 197947, a = 3.039 Å and c = 3.063 Å) due to the very similar atomic radii of Mo and W. Nevertheless, Rietveld refinement as well as EDS analysis (**Figure 4.2**) confirmed the presence and amounts of both Mo (69 at.%) and W (31 at.%) in the sample. Also, the refined lattice parameters of all other binary phases properly match with reported

values (**Table 4.1**).[45] The EDS mappings (**Figures 4.1b and 4.4**) show that all elements (Mo, W and B) are uniformly distributed over all materials according to their respective compositions. β-MoB_2 (**Figure 1a**) was synthesized in a tin flux according to our recently published procedure [19], then the resulting powder sample was pressed to a pellet and arc-melted in order to apply the same electrode preparation method for all samples (see below). Scanning electron microscopy (SEM) images of α-$Mo_{0.7}W_{0.3}B_2$ electrode surface shows heterogenous particle size distribution in the micrometer range with some particles larger than 5 μm (**Figures 5**), as expected from the synthesis method which always produces bulk materials. [19]

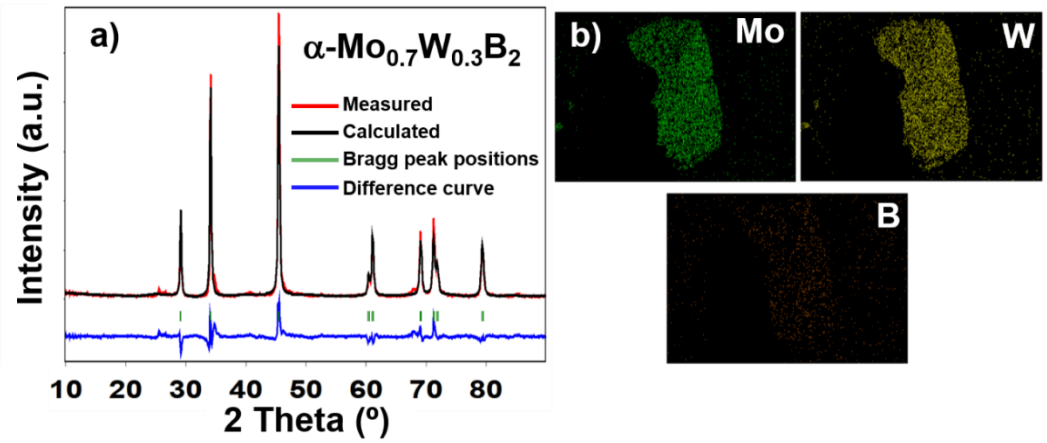

Figure 4.2. a) Refined powder X-ray diffraction pattern of α-$Mo_{0.7}W_{0.3}B_2$ b) EDS elemental mapping of Mo, W and B for α-$Mo_{0.7}W_{0.3}B_2$.

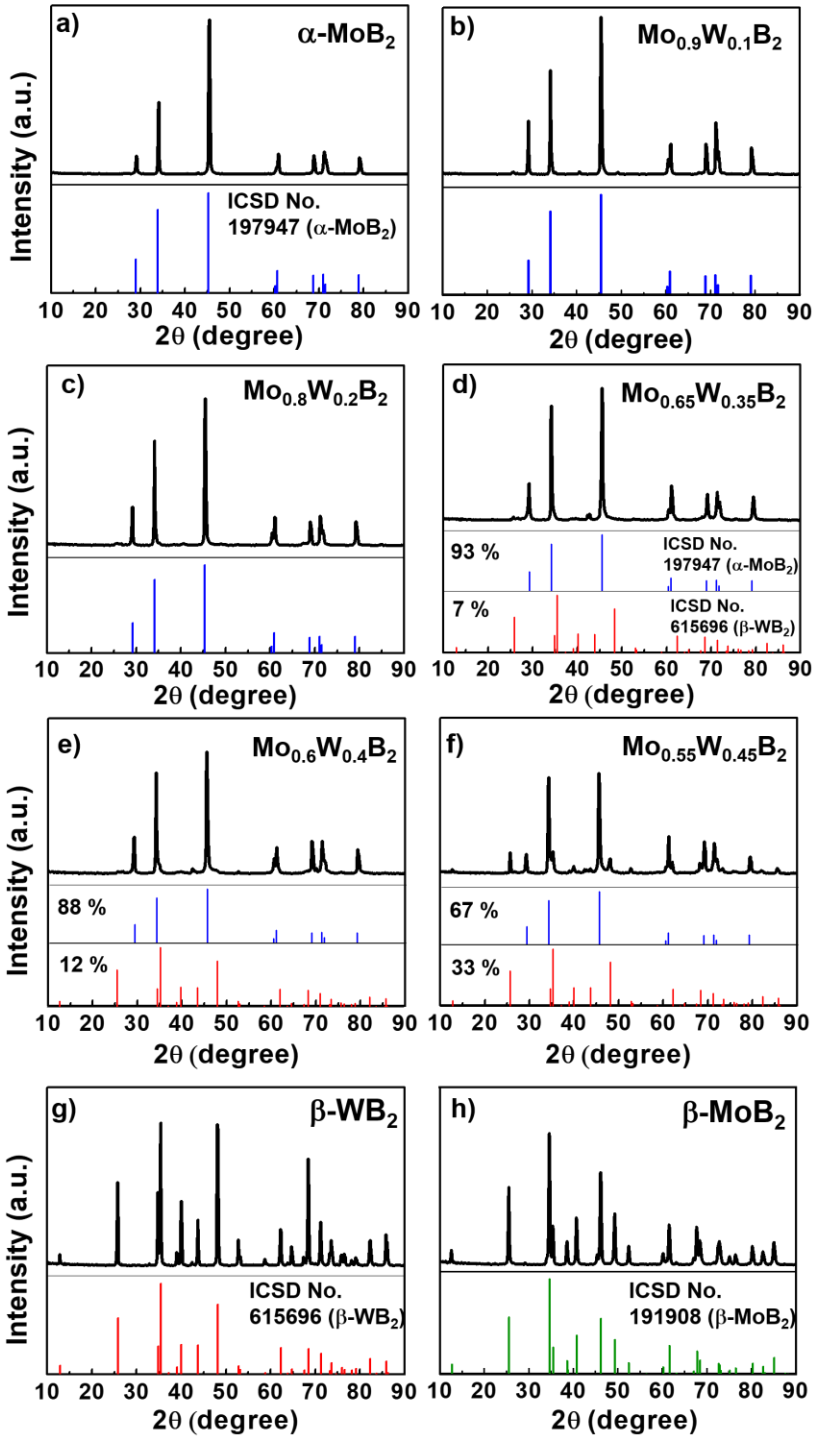

Figure 4.3. Powder X-ray diffraction data of α-MoB_2, $Mo_{1-x}W_xB_2$ (x = 0.1, 0.2, 0.35, 0.4, 0.45), β-WB_2 and β-MoB_2.

Table 4.1. Crystallographic information for the studied molybdenum-tungsten boride. Reported lattice parameters are given in square brackets. [45-46]

Phase	**α-$Mo_{0.7}W_{0.3}B_2$**
Crystal system	Hexagonal
Space group	*P6/mmm*
a [Å]	3.034(1)-[3.039]
c [Å]	3.064(2)-[3.063]
V [$Å^3$]	24.41(1)-[24.50]
Calc. density [g/cm^3]	9.794
Atomic ratio	Mo: 69 at.% , W: 31 at.%
Phase	**α-MoB_2**
Crystal system	Hexagonal
Space group	*P6/mmm*
a [Å]	3.041(1)-[3.039]
c [Å]	3.064(2)-[3.063]
V [$Å^3$]	24.53(3)-[24.50]
Calc. density [g/cm^3]	7.956
Phase	**β-MoB_2**
Crystal system	Trigonal
Space group	*R-3mH*
a [Å]	3.009(1)-[3.010]
c [Å]	20.905(4)-[20.926]
V [$Å^3$]	163.92(5)-[164.19]
Calc. density [g/cm^3]	7.146
Phase	**β-WB_2**
Crystal system	Hexagonal
Space group	*$P6_3/mmc$*
a [Å]	2.981(1)-[2.984]
c [Å]	13.873(3)-[13.87]
V [$Å^3$]	106.83(3)-[106.96]
Calc. density [g/cm^3]	13.112

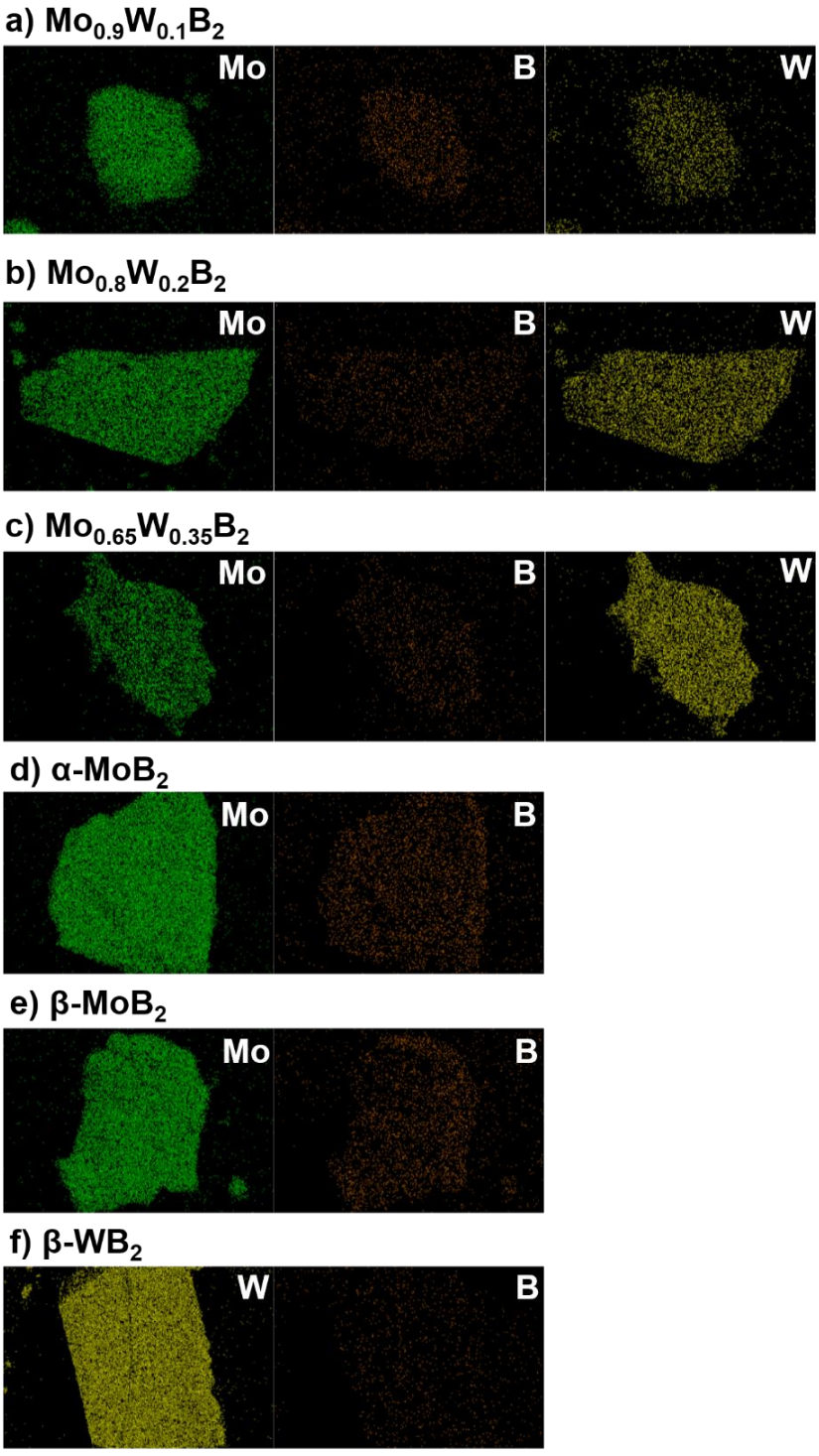

Figure 4.4. EDS mapping of $Mo_{1-x}W_xB_2$ (x = 0.1, 0.2, 0.35), α-MoB_2, β-MoB_2 and β-WB_2.

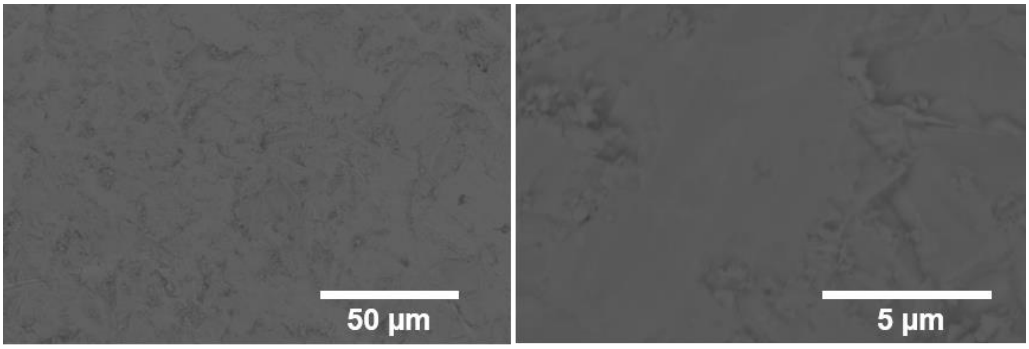

Figure 4.5. SEM images of α-$Mo_{0.7}W_{0.3}B_2$ electrode surface showing heterogenous particle size distribution in the micrometer range (left) and enlarged image showing a large particle of more than 5 µm (right).

X-ray photoelectron spectroscopy (XPS) was conducted to analyze the surface chemical composition and electronic states of α-$Mo_{0.7}W_{0.3}B_2$ (**Figure 4.6**). The high resolution XPS spectra of Mo and W can be deconvoluted into four different oxidation states (Mo^0, Mo^{3+}, Mo^{4+}, Mo^{6+} and W^0, W^{4+}, W^{5+}, W^{6+}) while those of B show two oxidation states (B^0 and B^{3+}). Oxygen peaks are also found due to the surface oxidation of the sample after exposure in air as usually found in most materials. [17, 47-49] The XPS spectrum of β-WB_2 also shows four oxidation states for tungsten and two oxidation states for boron (**Figure 4.7**). The XPS analysis of α-MoB_2 and β-MoB_2 were already reported in our previous papers.[18-19] The fact that the majority components of these spectra are from the non-oxidized species (Mo^0 and B^0) indicates that the oxide layer on the surface of these materials is very thin.

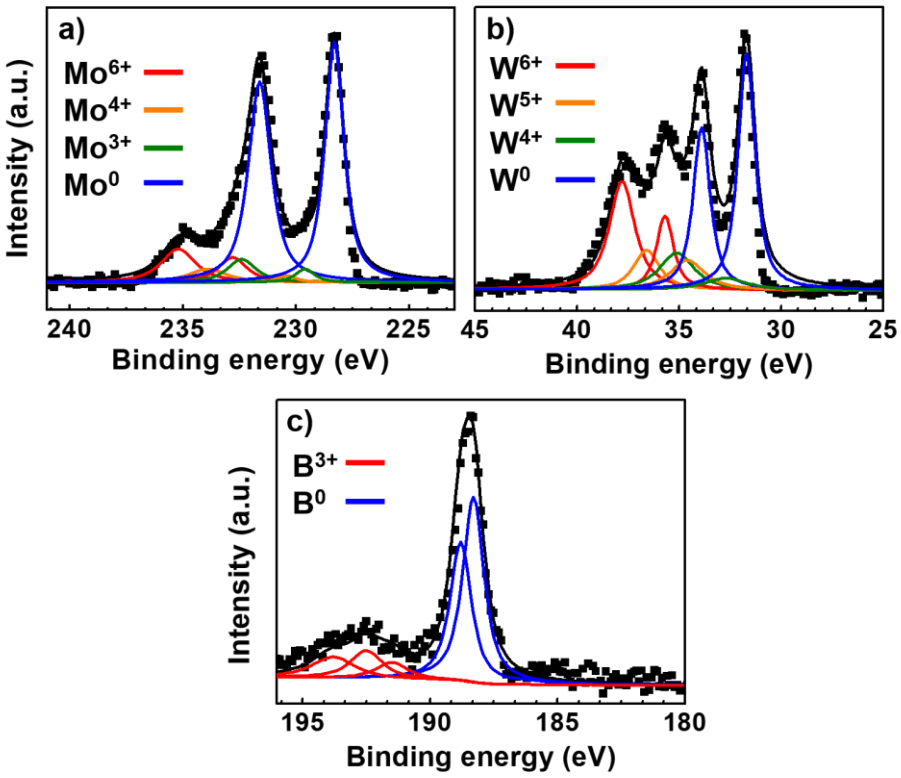

Figure 4.6. XPS spectra of α-$Mo_{0.7}W_{0.3}B_2$ a) Mo 3d, Mo^0 (blue), Mo^{3+} (green), Mo^{4+} (orange), Mo^{6+} (red), b) W 4f, W^0 (blue), W^{4+} (green), W^{5+} (orange), W^{6+} (red) and c) B 1s, B^0 (blue), B^{3+} (red). Experimental data (■), fitting peaks (black line).

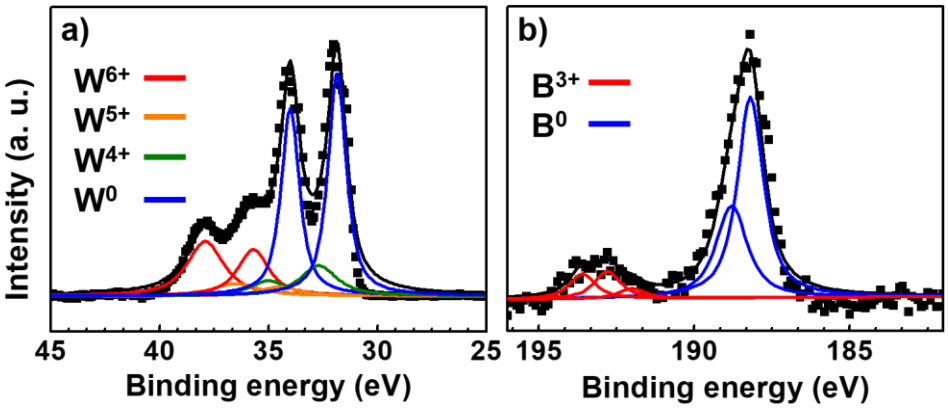

Figure 4.7. XPS spectra of β-WB_2, a) W 4f, W^0 (blue), W^{4+} (green), W^{5+} (orange), W^{6+} (red) and b) B 1s, B^0 (blue), B^{3+} (red). Experimental data (■), fitting peaks (black line).

Table 4.2. XPS parameters (peak position and full width at half maximum (FWHM)) for Mo 3d, W 4f and B 1s of $Mo_{0.7}W_{0.3}B_4$ and β-WB_2. [17, 47-51]

Phase	Species	Peak position (eV)	FWHM (eV)
α-$Mo_{0.7}W_{0.3}B_2$	Mo^0	228.3, 231.6	1, 1.2
	Mo^{3+}	229.6, 232.8	1, 1.5
	Mo^{4+}	230.4, 233.9	1, 2
	Mo^{6+}	232.8, 235.2	1.5, 1.8
	W^0	31.7, 33.6	1, 1
	W^{4+}	32.9, 35.12	2.5, 2
	W^{5+}	34.6, 36.6	2, 1.5
	W^{6+}	35.7, 37.8	1, 1.5
	B^0	188.3, 188.8	1, 1
	B^{3+}	191.5, 192.5, 193.8	1.5, 1.5, 2
Phase	**Species**	**Peak position (eV)**	**FWHM (eV)**
β-WB_2	W^0	31.85, 34.0	1, 1
	W^{4+}	32.7, 35.0	2, 2
	W^{5+}	34.5, 36.5	2, 2.5
	W^{6+}	35.7, 37.9	1.7, 2
	B^0	188.2, 188.8	1, 1.2
	B^{3+}	192.0, 192.8, 193.6	1, 1, 1

The HER activity of the metal borides α-MoB_2, α-$Mo_{1-x}W_xB_2$ (x =0.1, 0.2, 0.3, 0.35, 0.4), β-MoB_2 and β-WB_2 have been examined using the standard three electrodes system in acidic (0.5 M H_2SO_4) medium at a scan rate of 5 mV/s under IR drop compensation (**Figure 4.8**). One of the main problems of electrocatalysis is the electrode preparation, which may drastically affect the electrochemical performance of the studied material. The most common electrode preparation method is drop casting, which works very well for fine nanosized particles but very poorly for large particle (bulk) samples because of the inability of these materials to accurately cover the electrode's surface. A good example is the very active bulk α-MoB_2 material: In our first report of this phase (also repeated in this work) an overpotential of 300 mV was found to drive a current density of 10 mA/cm^2, while Shen et al. reported a twofold improved value (149 mV) for the same material, [21] due to their high-pressure-synthesized sample used as disc (similar to thin film) that completely covers the surface of the electrode. Even more impressive is that the high-pressed bulk disc electrode had a slightly better overpotential than the nanosized (albeit agglomerated) α-MoB_2 prepared by drop casting (154 mV overpotential). [20] Therefore, it is obvious that preparing denser working electrodes of bulk materials leads to better performance and higher HER activity simply because of better coverage of the electrode's surface. We have therefore prepared all working electrodes in this work using disc samples: After cutting and polishing an arc-melted sample (very dense sphere), the resulting disc was attached on a copper sheet (**Scheme 4.1**). Using this method of electrode preparation, the α-MoB_2 and β-MoB_2 disc samples show about 80-90 mV lower overpotential in comparison with the previous drop casting electrode preparation method (**Figure 4.9a, b**). For adequate

comparison purposes, we have also prepared bulk disc electrodes of molybdenum, tungsten and boron. W, Mo and B are poor electrocatalysts, but W is significantly more active than Mo and B (**Figure 4.8**). While the binaries α-MoB_2 and β-MoB_2 have been studied previously,[18-21] the HER activity of β-WB_2 was examined for the first time. Interestingly, β-WB_2 shows only slightly lower overpotential (271 mV at 10 mA/cm^2) than β-MoB_2 (277 mV at 10 mA/cm^2), an expected behavior if structure-activity relationships are valid: In fact, β-WB_2 and β-MoB_2 have similar crystal structures in which graphene-like and phosphorene-like B layers alternate (**Figure 4.1**), thus they are expected to show similar activity, the transition metal being the main difference. Because it was shown that the graphene-like B-layers are more active than the phosphorene-like B-layers (see also theory section below), α-MoB_2 (with graphene-like B layers only) is expected to be more active than β-WB_2 and β-MoB_2. Indeed, α-MoB_2 needs at least 45 mV less overpotential than the β-phases to drive a 10 mA/cm^2 current density, a further confirmation of the structure-activity relationships in these diborides and the importance of the graphene-like boron layers. Using the knowledge gained from this analysis, we have then designed a superior catalyst by substituting Mo in α-MoB_2 for the more active W (**Figure 4.8**) leading to the solid solution α-$Mo_{1-x}W_xB_2$ (single phase for $x < 0.35$, see above). Indeed, all members of this solid solution have better activity than α-MoB_2 and their activity increases with increasing x until $x = 0.3$ before slightly decreasing. This decrease of activity at $x > 0.3$ is due to the presence of the less active β-WB_2 as a side phase in significant amount (7 – 33 wt.%, see **Figure 4.3**). In the following, we will focus on α-$Mo_{0.7}W_{0.3}B_2$, which shows the

lowest overpotential among the α-$Mo_{1-x}W_xB_2$ electrocatalysts, with a 25 mV lower overpotential (201 mV at 10 mA/cm^2) than the best binary electrocatalyst, α-MoB_2.

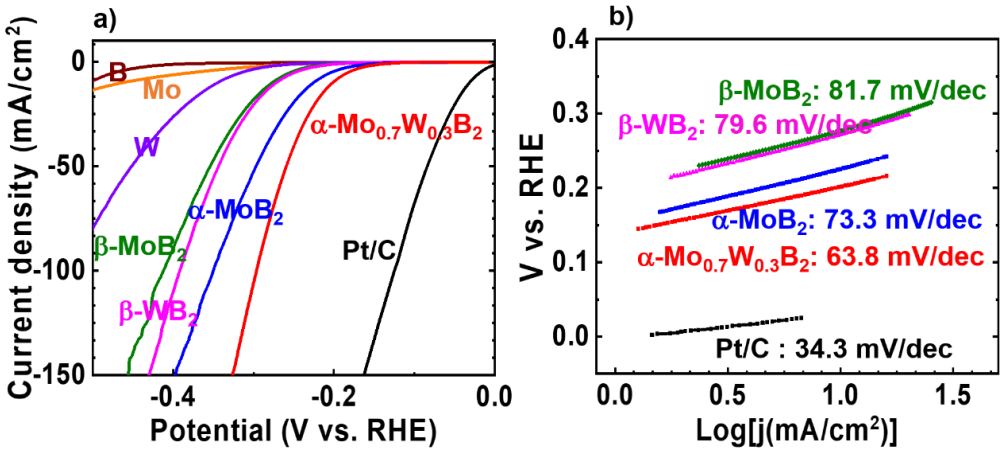

Figure 4.8. a) Linear sweep polarization curves obtained in 0.5 M H_2SO_4 of all phases studied and b) the corresponding Tafel slopes. The current density was normalized with the electrode's geometric surface area.

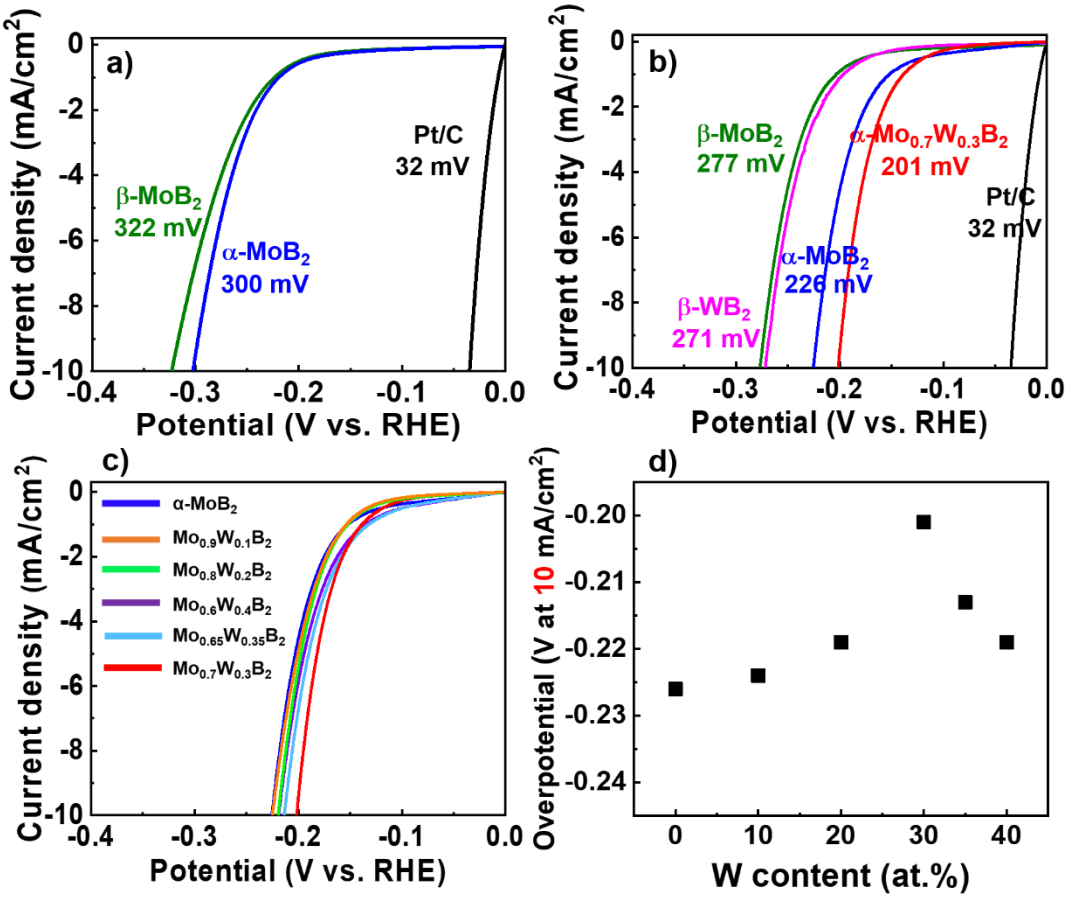

Figure 4.9. Polarization curves of a) previous method (drop-casting), b) new method (disc-electrode), c) α-MoB_2, $Mo_{1-x}W_xB_2$ (x = 0.1, 0.2, 0.3, 0.35, 0.4) in 0.5 M H_2SO_4 and d) overpotential of α-MoB_2, $Mo_{1-x}W_xB_2$ (x = 0.1, 0.2, 0.3, 0.35, 0.4) at 10 mA/cm^2.

The electrochemically active surface area (ECSA) of the four metal borides was estimated by calculating the double layer capacitance (C_{dl}) from cyclic voltammetry (CV) at various scan rates between 0.1 - 0.2 V vs. reversible hydrogen electrode (RHE). [52] As shown in **Figure 4.10**, the calculated C_{dl} values are 3, 2.3, 1.6 and 1.4 mF/cm^2 for α-$Mo_{0.7}W_{0.3}B_2$, α-MoB_2, β-WB_2 and β-MoB_2, respectively. Consequently, α-$Mo_{0.7}W_{0.3}B_2$ has the highest number of active sites, closely followed by α-MoB_2, while β-WB_2 and β-MoB_2 have similar number of active sites and far less than the α-phases. This finding is in full agreement with

the overpotential classification above. The activity trend for all four phases was further confirmed by electrochemical impedance spectroscopy (EIS) measurements, which revealed that α-$Mo_{0.7}W_{0.3}B_2$ has the smallest electron transfer resistance, followed by α-MoB_2, β-WB_2 and β-MoB_2 (**Figure 4.11**).

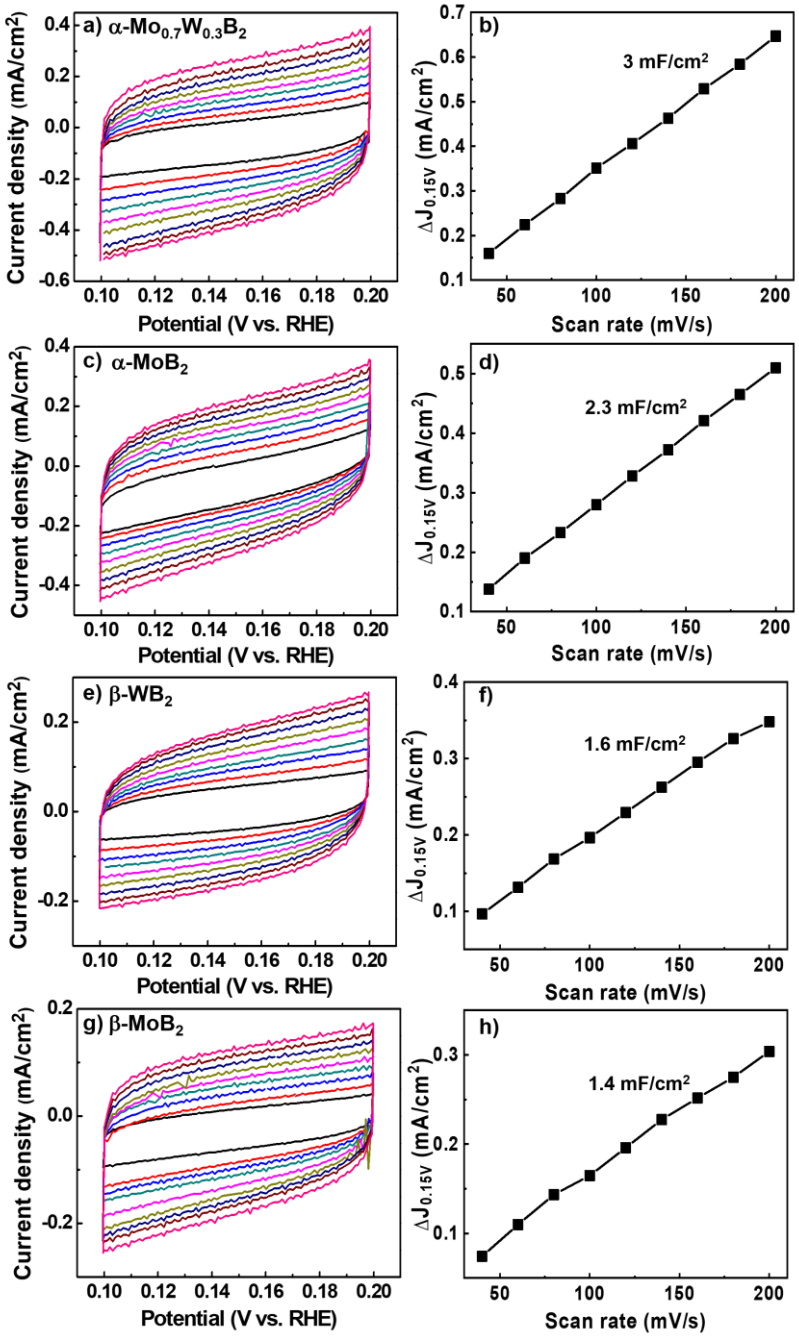

Figure 4.10. a), c), e) and g) Cyclic voltammetry curves of α-$Mo_{0.7}W_{0.3}B_2$, α-MoB_2, β-WB_2 and β-MoB_2. b), d), f) and h) The difference current density ΔJ (J_a-J_c) at 0.15 V vs. RHE plotted against the scan rate is fitted to a linear regression to estimate C_{dl}.

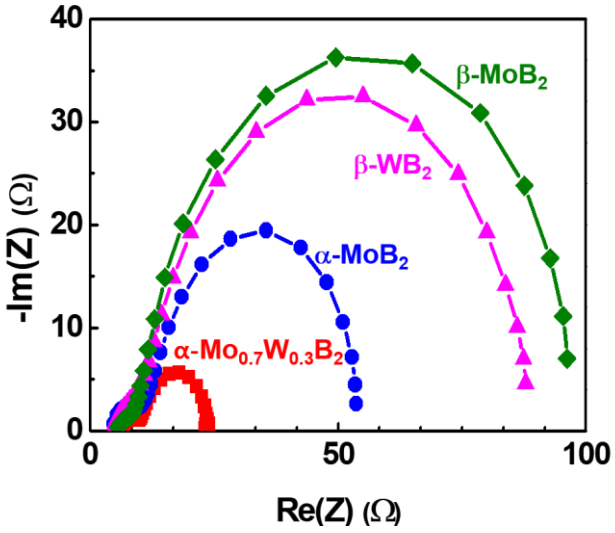

Figure 4.11. Electrochemical impedance spectroscopy (EIS) Nyquist plots of α-$Mo_{0.7}W_{0.3}B_2$, α-MoB_2, β-WB_2 and β-MoB_2.

Interestingly, at high current density (above 125 mA/cm^2), the performance gap between the new phase and others widens. For example, to deliver 150 mA/cm^2 current density α-$Mo_{0.7}W_{0.3}B_2$ needs an overpotential of 320 mV which is much lower than 400 mV, 420 mV and 440 mV required for α-MoB_2, β-WB_2 and β-MoB_2, respectively. At 10 mA/cm^2 the overpotential gap between α-$Mo_{0.7}W_{0.3}B_2$ and the best binary (α-MoB_2) was 25 mV while this gap more than tripled (80 mV) at 150 mA/cm^2. This high efficiency at high current density can be mainly attributed to W because it outperforms Mo not only in elemental form but also in the binaries β-WB_2 and β-MoB_2, a finding also confirmed by our theoretical results below.

The intrinsic electrochemical catalytic activity of bimetallic phases has primarily been attributed to the synergistic effect of the two metals.[53-54] According to our discussion above, Mo is necessary to stabilize the highly active graphene-like boron layers in α-$Mo_{1-x}W_xB_2$

while W is crucial in enhancing the activity at high current density because of its higher performance in elemental form and in binary borides if compared to molybdenum. These factors support the synergistic effect on HER activity enhancement in this novel solid solution catalyst (see also theory part below).

The Tafel plot is usually applied to reveal the HER catalytic mechanism. In general, there are three classical reactions which can be the rate-determining steps, the Volmer reaction (Tafel slope of ~120 mV/dec.), the Heyrovsky reaction (Tafel slope of ~40 mV/dec.) and the Tafel reaction (Tafel slope of ~30 mV/dec.). [55-57] As shown in **Figure 4.8b**, the obtained Tafel slopes of all samples are comprised between 63.8 mV/dec. (α-$Mo_{0.7}W_{0.3}B_2$) and 81.7 mV/dec. (β-MoB_2), meaning that they do not match any ideal Tafel slope given above. Consequently, like other bulk transition metal borides reported until now, it is difficult to determine the rate-determining step using the Tafel analysis due to reaction complexity of bulk catalysts. However, α-$Mo_{0.7}W_{0.3}B_2$ has the lowest Tafel slope indicating a much efficient HER process than for all binary borides.

The cyclic stability is also a key factor for HER electrocatalysts, and it is usually evaluated by cyclic voltammetry (CV). Our CV analysis was carried out for 5000 cycles in acid solution (**Figure 4.12a**). The final polarization curves show highly efficient HER activity without notable degradation after 5000 cycles. The long-term durability of α-$Mo_{0.7}W_{0.3}B_2$ was further confirmed by HER electrolysis at a fixed overpotential of 230 mV (**Figure 4.12b**), and it showed a very stable current density with little decay over 20 hrs.

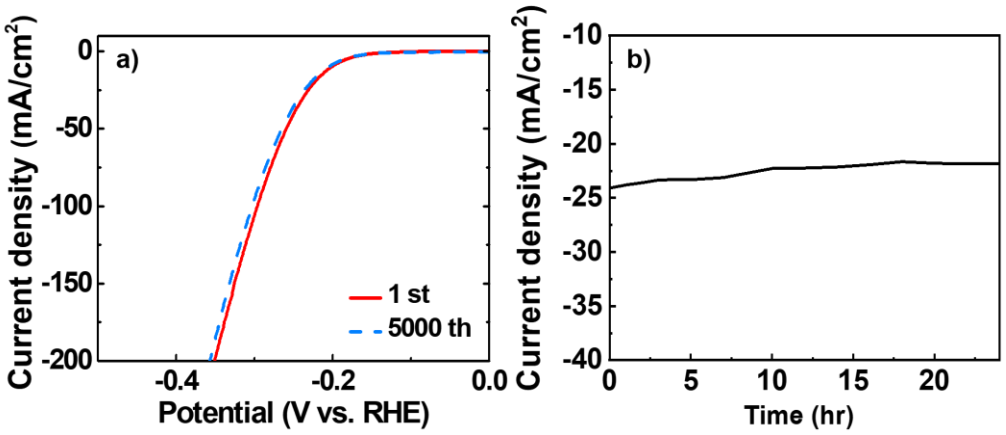

Figure 4.12. a) HER stability measurement of α-$Mo_{0.7}W_{0.3}B_2$ before and after 5000 cycles with scan rate of 100 mV/s in 0.5 M H_2SO_4. b) Chronoamperometry curve of α-$Mo_{0.7}W_{0.3}B_2$ at overpotential of 230 mV in 0.5 M H_2SO_4.

β-WB_2 and α-$Mo_{0.7}W_{0.3}B_2$ are new members of a growing list of highly active non-noble metal electrocatalysts (**Table 4.3**), and they represent the first tungsten-based boride HER electrocatalysts. The excellent HER activity of α-$Mo_{0.7}W_{0.3}B_2$ not only provides a new HER electrocatalyst containing graphene-like boron layers but also provide a new path to designing such boride electrocatalysts that are highly efficient at high current density. While high-pressure-synthesized α-MoB_2 was recently shown to be an excellent high current density material, [21] our discovery shows that α-$Mo_{0.7}W_{0.3}B_2$ clearly outperforms α-MoB_2 when synthesized and studied under the same conditions.

Table 4.3. Comparison of HER catalytic activity in acidic electrolyte of some highly active non-noble metal bulk and nanoscale materials.

Catalyst	Morphology	Electrolyte	Overpotential (mV) at 10 mA/cm²	Overpotential (mV) at 100 mA/cm²	Tafel slope (mV/dec)	Ref. No.
α-$Mo_{0.7}W_{0.3}B_2$	Bulk disc	0.5 M H_2SO_4	-202	-301	63.8	This work
α-MoB_2	Bulk disc	0.5 M H_2SO_4	-226	-349	73.3	This work
β-WB_2	Bulk disc	0.5 M H_2SO_4	-271	-391	79.6	This work
β-MoB_2	Bulk disc	0.5 M H_2SO_4	-277	-411	81.7	This work
α-MoB_2	High pressure bulk disc	0.5 M H_2SO_4	-149	-220	74.2	21
α-MoB_2	Nanoparticles	0.5 M H_2SO_4	-154	-	49	20
VB_2	Nanoparticles	0.5 M H_2SO_4	-192	-	68	28
Mo_3B	Film	0.5 M H_2SO_4	-230	-	52	26
MoAlB	Single crystal (Etched)	0.5 M H_2SO_4	-300	-	68	27
MoB	Bulk powder	1 M H_2SO_4	-210	-	55	17
Mo_2C	Bulk powder		-208	-	56	
MoS_2	Bulk powder	0.5 M H_2SO_4	-360	-	-	57
	Nano sphere		-210	-	100	
Mo_2C/CC	Micro-islands	0.5 M H_2SO_4	-120	-370	124	58
$MoSe_2$	Micro-particles	0.5 M H_2SO_4	-210	-350	117	59
	Nano-sheet		-50	-150	38	
CoS_2	Film	0.5 M H_2SO_4	-190	-	51.4	60
	Microwire		-158	-230	58	
	Nanowire		-145	-210	51.6	
P-Ag	Nanoflake	0.5 M H_2SO_4	-100	-340	107	61
$MoSe_2$-$CoSe_2$	Nanotube	0.5 M H_2SO_4	-210	-300 (@ 80 mA/cm₂)	45	62
CoP/CC	Nanowire	0.5 M H_2SO_4	-80	-210	51	63
$Mo_{0.06}W_{0.94}C$/CB	Nanoparticles	0.5 M H_2SO_4	-220	-	-	32
TiS_2	Nanosheets	0.5 M H_2SO_4	-245	-	77	64

To investigate the active sites and distinct HER activities, the binding energy (ΔE_H) and Gibbs free energy (ΔG_H) for H adsorption on different surfaces of the new β-WB_2 and α-$Mo_{0.75}W_{0.25}B_2$ electrocatalysts were evaluated by density functional theory (DFT) calculations and compared with those for known α- and β-MoB_2 (see SI for more details). ΔE_H at 25% H-coverage is commonly used to determine the preferred adsorption site on each surface while ΔG_H is widely accepted as a descriptor for correlating theoretical predictions with experimental measurements of the HER activity. [43-44, 65-67] An optimal activity can be achieved at a ΔG_H value close to zero, where the overall reaction of both H adsorption and H_2 desorption has the maximum rate. [66] Four surfaces in β-WB_2 were considered, namely W1-, W2-, flat B- and puckered B-terminated {001} surfaces, while the flat B- and mixed Mo/W-terminated {001}, the mixed Mo/B- and Mo/W/B-terminated {110} surfaces were investigated in α-$Mo_{0.75}W_{0.25}B_2$. The results are listed in **Figure 4.13-17** and **Tables 4.4-7**. Similar to the previous results obtained for β-MoB_2 [19], in β-WB_2 the bridge site (Bg) of the flat B surface, the Hollow sites (Ho) of the metal (W1 and W2) surfaces and one of the top sites (T1) of the puckered B surface are the preferred adsorption sites because of their relatively high H-surface binding energy at 25% H-coverage (see **Table 4.4**). ΔG_H was examined at different H coverages for the preferred adsorption sites of all four W- and B-terminated surfaces in β-WB_2 and compared with those of β-MoB_2. The results are listed in the **Table 4.5** and plotted in **Figure 4.13a**. Like in β-MoB_2, [19] ΔG_H for the puckered B and the W2 surfaces in β-WB_2 are far below zero even at 100% H-coverage (light green and orange lines in **Figure 4.13a**), indicating weak HER activity of these two surfaces. At 25% H-coverage, ΔG_H for the flat B surface in β-WB_2 is −0.10 eV

and reaches zero between 25% and 50% H-coverage (green line in **Figure 4.13a**), indicating that the flat B surface is very active for HER, as found for all flat B surfaces studied until now. [19-20, 22, 28] Unlike in β-MoB_2, where the Mo surface is not active the W1 surface in β-WB_2 has relatively high HER activity, as its ΔG_H reaches −0.20 eV at 50% H-coverage and stays nearly constant up to 100% H-coverage (red line in **Figure 4.13a**). While most surfaces have similar activities in β-WB_2 and β-MoB_2 the presence of W significantly improves the HER activity of β-WB_2, thus confirming the experimentally found results.

To simulate the most HER active α-$Mo_{0.7}W_{0.3}B_2$ ternary, a 2 × 2 × 2 supercell was used in which each metal layer contains three Mo atoms and one W atom resulting in α-$Mo_{0.75}W_{0.25}B_2$. Two structural configurations of α-$Mo_{0.75}W_{0.25}B_2$ were built based on two different distributions of W in the metal layers: In the low total energy configuration W builds an I-lattice and short W-W contacts are avoided (**Figure 4.16**). With a 5% increase of W from α-$Mo_{0.75}W_{0.25}B_2$ to α-$Mo_{0.7}W_{0.3}B_2$, there will still be avoidance of direct W-W contacts, therefore $Mo_{0.75}W_{0.25}B_2$ is a good model to describe $Mo_{0.7}W_{0.3}B_2$ and it saves a lot of computation time. Because of the coexistence of Mo and W atoms in one metal layer, there are more sites for H-adsorption in α-$Mo_{0.75}W_{0.25}B_2$ than in α-MoB_2. There are two top sites (T1 and T2), two bridge sites (Bg1 and Bg2) and two hollow sites (Ho1 and Ho2) for each B- and M-terminated {001} surfaces (**Figure 4.17**). Like α-MoB_2, the two Bg sites of B-terminated {001} and the two Ho sites of M-terminated {001} are the most preferred adsorption sites because of their relatively high H-surface binding energy at 25% H-coverage (**Table 4.6**). There are two {110} surfaces in α-$Mo_{0.75}W_{0.25}B_2$ because of the W

substitution, namely the Mo/B mixed surface and the Mo/W/B mixed surface (**Figure 4.17**). Since the Ho site is the only active site of the Mo/B mixed {110} surface in α-MoB_2 [20] (the T, Bg1 and Bg2 sites all have positive H-binding energy, while only the Ho site has negative H-binding energy), only the Ho site of the two {110} metal surfaces in α-$Mo_{0.75}W_{0.25}B_2$ was considered for comparison.

ΔG_H was examined at different H coverages for the Bg and Ho sites of the B- and M-terminated {001} surfaces and the Ho site of the mixed Mo/B and Mo/W/B {110} surfaces in α-$Mo_{0.75}W_{0.25}B_2$ and compared with those in α-MoB_2. The results are listed in the **Table 4.7** and plotted in **Figure 4.13b**. Similar to α-MoB_2 [20], ΔG_H for the flat B layer stays close to zero below 75% H-coverage and reaches zero between 75% and 100% H-coverage (green line), indicating high HER activity. Just like in α-MoB_2, the Ho sites of the two α-$Mo_{0.75}W_{0.25}B_2$ {110} surfaces are also highly active, as their ΔG_H curves cross zero between 50% and 75% H coverage (pink and blue lines). On the contrary, ΔG_H for the M-terminated {001} surface increases as H-coverage increases but never reaches zero even at 100% H-coverage (orange line), indicating the weak HER activity of this surface. Based on the results in **Table 4.7** and **Figure 4.13b**, ΔG_H for all surfaces in α-$Mo_{0.75}W_{0.25}B_2$ are slightly better than those of α-MoB_2 at 50% H-coverage while they are close to each other at other H-coverages, indicating α-$Mo_{0.75}W_{0.25}B_2$ has slightly better HER activity, in agreement with the experimental observation. To understand the experimentally observed better HER activity at high current densities in favor of α-$Mo_{0.75}W_{0.25}B_2$, we have examined the optimized structural configurations of H adsorption on the mixed {110} surfaces of α-$Mo_{0.75}W_{0.25}B_2$ at 100% H-coverage. Interestingly, two hydrogen atoms are attracted by the

W atoms on the Mo/W/B mixed {110} surface **(Figure 4.14a, b**) while they are not attracted by the Mo atoms on the Mo/B mixed {110} surface (**Figure 4.14c**). Therefore, on the mixed Mo/W/B surface the interaction between W and the two nearby H atoms brings these H atoms much closer to each other, thus facilitating their binding toward producing H_2. A behavior not found for the mixed Mo/B surface. Consequently, the presence of W helps with the formation of H_2, especially at high H-coverage. This result is consistent with the higher HER activity experimentally observed for α-$Mo_{0.7}W_{0.3}B_2$ if compared to α-MoB_2 at high current density.

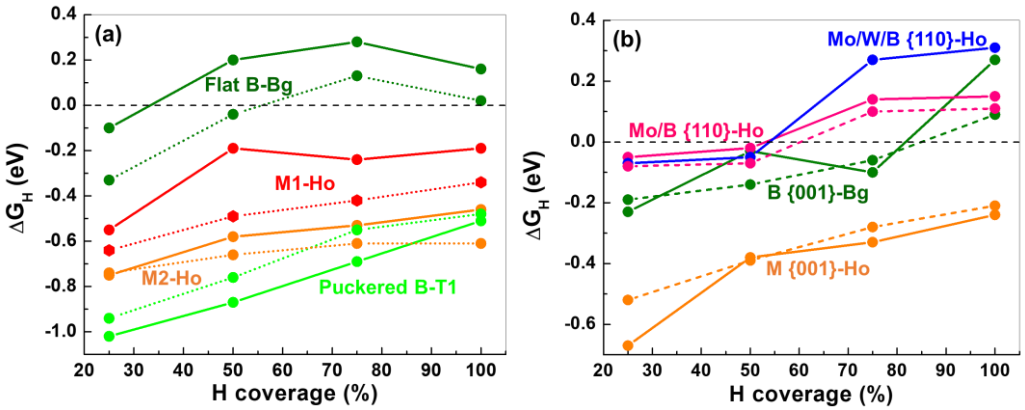

Figure 4.13. (a) The Gibbs free energy (ΔG_H) for H adsorption on the Bg site of flat B (green), T1 site of puckered B (light green), Ho site of M1- and M2-terminated {001} (red and orange, respectively) surfaces for β-WB_2 (solid lines) and β-MoB_2[19] (dashed lines) plotted as a function of hydrogen coverage. (b) The Gibbs free energy (ΔG_H) for H adsorption on the Bg site of B-terminated {001} (green), Ho site of M-terminated {001} (orange), mixed Mo/B {110} (pink) and mixed Mo/W/B {110} (blue) surfaces for α-$Mo_{0.75}W_{0.25}B_2$ (solid lines) and α-MoB_2[20] (dashed lines) plotted as a function of hydrogen coverage.

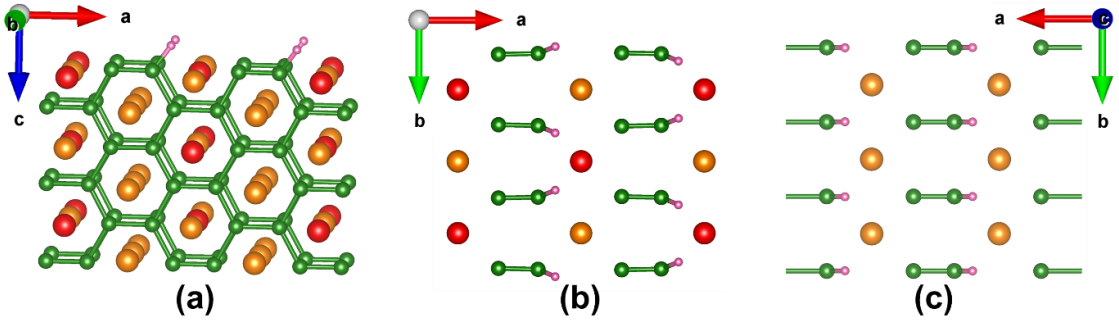

Figure 4.14. (a) The optimized structural configuration on the mixed Mo/W/B {110} surface of α-$Mo_{0.75}W_{0.25}B_2$ at 100% H-coverage. The ab-plane projection of the 100% H-coverage configuration on (b) the mixed Mo/W/B {110} and (c) the mixed Mo/B surfaces of α-$Mo_{0.75}W_{0.25}B_2$. Mo, W, B and H atoms are indicated by orange, red, green and pink spheres, respectively.

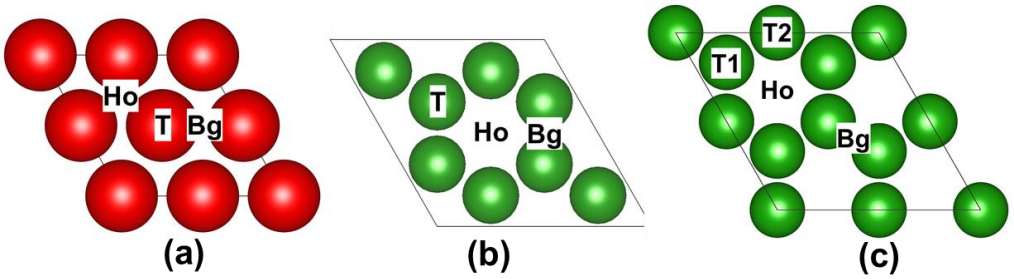

Figure 4.15. H adsorption site on (a) W1 and W2 surface, (b) flat B surface, (c) puckered B surface of β-WB_2. T, Bg and Ho represents the top, the bridge and the hollow sites, respectively. W and B atoms are indicated by red and green spheres, respectively. There are two top sites for the puckered B layer: the one on top of the outer B (T1) and the one on top of the inner B (T2).

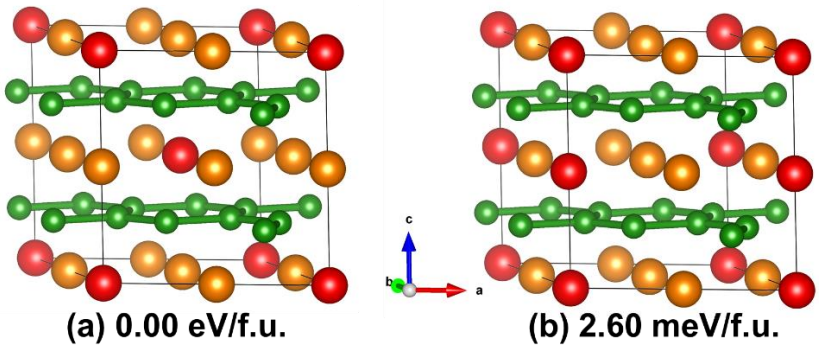

Figure 4.16. Two different configurations of $Mo_{0.75}W_{0.25}B_2$. Configuration (a) is lower in energy than configuration (b) by 2.60 meV/formula unit (meV/f.u.) so it is relatively stable and indicate that avoiding W-W contacts is favorable. Mo, W and B atoms are indicated by orange, red and green spheres, respectively.

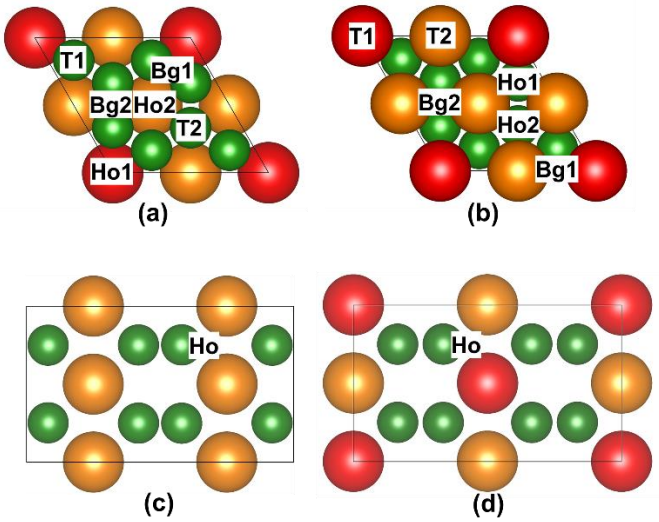

Figure 4.17. H adsorption site on (a) the B- and (b) the metal (M)-terminated {001} surfaces of α-$Mo_{0.75}W_{0.25}B_2$. T, Bg and Ho represents the top, the bridge and the hollow sites, respectively. The B-terminated {001} layer has two top sites, T1: on top of B that sits above the hollow of two Mo and one W and T2: on top of B that sits above the hollow of three Mo; two bridge sites, Bg1: on top of the B−B and Mo−W bonds and Bg2: on top of the B−B and Mo−Mo bonds; two hollow sites, Ho1: in the hollow of B6 ring and above W and Ho2: in the hollow of B6 ring and above Mo. The M-terminated {001} layer has two top sites, T1: above W and T2: above Mo; two bridge sites, Bg1: on top of the Mo−W bond and Bg2: on top of the Mo−Mo bond; two hollow sites, Ho1: in the hollow of two Mo and one W and Ho2: in the hollow of three Mo. The HER active hollow (Ho) site of (c) the Mo/B mixed and (d) the Mo/W/B mixed {110} surfaces of α-$Mo_{0.75}W_{0.25}B_2$. Mo, W and B atoms are indicated by orange, red and green spheres, respectively.

Table 4.4. Calculated binding energy (ΔE_H) and Gibbs free energy (ΔG_H) of single H (**25% H coverage**) adsorption on W1-, W2-, flat and puckered B-terminated β-WB_2 {001} surfaces.

Binding site	Top (T)		Bridge (Bg)		Hollow (Ho)	
	ΔE_H (eV)	ΔG_H (eV)	ΔE_H (eV)	ΔG_H (eV)	ΔE_H (eV)	ΔG_H (eV)
W1	−0.41	−0.21	−0.55	−0.35	−0.75	−0.55
W2	+0.26	+0.46	−0.95[a]	−0.75[a]	−0.95	−0.75
Flat B	−0.04	+0.16	−0.30	−0.10	+1.57	+1.77
Puckered B	−1.23 (T1)	−1.03 (T1)	−1.22[b]	−1.02[b]	+0.74	+0.94
	+0.29 (T2)	+0.49 (T2)				

[a] Converge to hollow site [b] Converge to T1 site

Table 4.5. Calculated Gibbs free energy (ΔG_H) of H adsorption on different surfaces: Bridge (Bg) and top (T1) sites of the flat and puckered B-terminated, as well as W1- and W2-terminated β-WB_2 {001} at different H coverages. Bold values indicate the ΔG_H window enclosing $\Delta G_H = 0$.

H coverage	Gibbs free energy (ΔG_H) / eV			
	Flat B (Bg)	Puckered B (T1)	W1 (Ho)	W2 (Ho)
25%	**−0.10**	−1.02	−0.55	−0.75
50%	**+0.20**	−0.87	−0.19	−0.58
75%	+0.28	−0.69	−0.24	−0.53
100%	+0.16	−0.51	−0.19	−0.46

Table 4.6. Calculated binding energy (ΔE_H) and Gibbs free energy (ΔG_H) of single H (25% H coverage) adsorption on the Mo/W- and B-terminated {001} surfaces of $Mo_{0.75}W_{0.25}B_2$.

Binding site	Top (T1/T2)		Bridge (Bg1/Bg2)		Hollow (Ho1/Ho2)	
	ΔE_H (eV)	ΔG_H (eV)	ΔE_H (eV)	ΔG_H (eV)	ΔE_H (eV)	ΔG_H (eV)
Mo/W-terminated {001}	−0.53/ −0.31	−0.33/ −0.11	−0.39/ −0.87[a]	−0.19/ −0.67[a]	−0.85/ −0.86	−0.65/ −0.66
B-terminated {001}	−0.41[b]/ −0.18	−0.21[b]/ +0.02	−0.43/ −0.39	−0.23/ −0.19	+1.77/ +1.63	+1.97/ +1.83

[a] Converge to Ho2 [b] Converge to Bg2

Table 4.7. Calculated Gibbs free energy (ΔG_H) of H adsorption on the bridge site (Bg) of B-terminated {001}, the hollow site (Ho) of Mo/W-terminated {001} and mixed Mo/B, Mo/W/B {110} surfaces of $Mo_{0.75}W_{0.25}B_2$ at different H coverages. Bold values indicate the ΔG_H window enclosing $\Delta G_H = 0$.

H coverage	Gibbs free energy (ΔG_H) / eV			
	B {001} (Bg)	Mo/W {001} (Ho)	Mo/B {110} (Ho)	Mo/W/B {110} (Ho)
25%	−0.23	−0.67	−0.05	−0.07
50%	−0.03	−0.38	**−0.02**	**−0.05**
75%	**−0.10**	−0.33	**+0.14**	**+0.27**
100%	**+0.27**	−0.24	+0.15	+0.31

4.4. Conclusion

In summary, bulk β-WB_2 and α-$Mo_{0.7}W_{0.3}B_2$ have been studied for their HER activity experimentally and theoretically for the first time. We found that β-WB_2 has only slightly better HER activity than β-MoB_2, as both have similar crystal structures containing both flat graphene- and puckered phosphorene-like boron layers. However, they are far less active than α-MoB_2 which contains only the flat graphene-like boron layers. Interestingly, a 30% substitution of W for Mo in α-MoB_2 produces α-$Mo_{0.7}W_{0.3}B_2$, which also contains only graphene-like boron layers and exhibits the highest HER activity in acidic medium at high current density. This result will pave the way for the design of inexpensive, durable, highly active high current density HER materials based on structure-activity relationships.

References

1. Cook, T. R.; Dogutan, D. K.; Reece, S. Y.; Surendranath, Y.; Teets, T. S.; Nocera, D. G., *Chem. Rev.* **2010,** *110*, 6474.
2. Merki, D.; Hu, X., *Energy Environ. Sci.* **2011,** *4*, 3878.
3. Hinnemann, B.; Moses, P. G.; Bonde, J.; Jørgensen, K. P.; Nielsen, J. H.; Horch, S.; Chorkendorff, I.; Nørskov, J. K., *J. Am. Chem. Soc.* **2005,** *127*, 5308.
4. Morales-Guio, C. G.; Stern, L. A.; Hu, X., *Chem. Soc. Rev.* **2014,** *43*, 6555.
5. Subbaraman, R.; Tripkovic, D.; Strmcnik, D.; Chang, K. C.; Uchimura, M.; Paulikas, A. P.; Stamenkovic, V.; Markovic, N. M., *Science* **2011,** *334*, 1256.
6. Lu, Q.; Yu, Y.; Ma, Q.; Chen, B.; Zhang, H., *Adv. Mater.* **2016,** *28*, 1917.
7. Xiao, X.; Tao, L.; Li, M.; Lv, X.; Huang, D.; Jiang, X.; Pan, H.; Wang, M.; Shen, Y., *Chem. Sci.* **2018,** *9*, 1970.
8. Zhang, R.; Wang, X.; Yu, S.; Wen, T.; Zhu, X.; Yang, F.; Sun, X.; Wang, X.; Hu, W., *Adv. Mater.* **2017,** *29*, 1605502.
9. Jaramillo, T. F.; Jørgensen, K. P.; Bonde, J.; Nielsen, J. H.; Horch, S.; Chorkendorff, I., *Science* **2007,** *317*, 100.
10. Wang, D.-Y.; Gong, M.; Chou, H. L.; Pan, C.-J.; Chen, H. A.; Wu, Y.; Lin, M. C.; Guan, M.; Yang, J.; Chen, C. W., *J. Am. Chem. Soc.* **2015,** *137*, 1587.
11. Chen, W. F.; Muckerman, J. T.; Fujita, E., *Chem. Commun.* **2013,** *49*, 8896.
12. Chen, W. F.; Sasaki, K.; Ma, C.; Frenkel, A. I.; Marinkovic, N.; Muckerman, J. T.; Zhu, Y.; Adzic, R. R., *Angew. Chem. Int. Ed.* **2012,** *51*, 6131.
13. Michalsky, R.; Zhang, Y. J.; Peterson, A. A., *ACS Catal.* **2014,** *4*, 1274.
14. Liao, L.; Wang, S.; Xiao, J.; Bian, X.; Zhang, Y.; Scanlon, M. D.; Hu, X.; Tang, Y.; Liu, B.; Girault, H. H., *Energy Environ. Sci.* **2014,** *7*, 387.
15. Fosdick, S. E.; Berglund, S. P.; Mullins, C. B.; Crooks, R. M., *ACS Catal.* **2014,** *4*, 1332.
16. Lv, H.; Xi, Z.; Chen, Z.; Guo, S.; Yu, Y.; Zhu, W.; Li, Q.; Zhang, X.; Pan, M.; Lu, G., *J. Am. Chem. Soc.* **2015,** *137*, 5859.
17. Vrubel, H.; Hu, X., *Angew. Chem. Int. Ed.* **2012,** *51*, 12703.
18. Park, H.; Encinas, A.; Scheifers, J. P.; Zhang, Y.; Fokwa, B., *Angew. Chem. Int. Ed.* **2017,** *56*, 5575.
19. Park, H.; Zhang, Y.; Scheifers, J. P.; Jothi, P. R.; Encinas, A.; Fokwa, B. P., *J. Am. Chem. Soc.* **2017,** *139*, 12915.
20. Jothi, P. R.; Zhang, Y.; Scheifers, J. P.; Park, H.; Fokwa, B. P., *Sustainable Energy Fuels* **2017,** *1*, 1928.
21. Chen, Y.; Yu, G.; Chen, W.; Liu, Y.; Li, G.-D.; Zhu, P.; Tao, Q.; Li, Q.; Liu, J.; Shen, X., *J. Am. Chem. Soc.* **2017,** *139*, 12370.
22. Li, H.; Wen, P.; Li, Q.; Dun, C.; Xing, J.; Lu, C.; Adhikari, S.; Jiang, L.; Carroll, D. L.; Geyer, S. M., *Adv. Energy Mater.* **2017,** *7*, 1700513.
23. Gupta, S.; Patel, N.; Miotello, A.; Kothari, D., *J. Power Sources* **2015,** *279*, 620.
24. Xu, N.; Cao, G.; Chen, Z.; Kang, Q.; Dai, H.; Wang, P., *J. Mater. Chem. A* **2017,** *5*, 12379.
25. Los, P.; Lasia, A., *J. Electroanal. Chem.* **1992,** *333*, 115.

26. Wang, X.; Tai, G.; Wu, Z.; Hu, T.; Wang, R., *J. Mater. Chem. A* **2017,** *5*, 23471.
27. Alameda, L. T.; Holder, C. F.; Fenton, J. L.; Schaak, R. E., *Chem. Mater.* **2017,** *29*, 8953.
28. Jothi, P. R.; Zhang, Y.; Yubuta, K.; Culver, D.; Conley, M. P.; Fokwa, B. P., *ACS Appl. Energy Mater.* **2019,** *2*, 176.
29. Voiry, D.; Yamaguchi, H.; Li, J.; Silva, R.; Alves, D. C.; Fujita, T.; Chen, M.; Asefa, T.; Shenoy, V. B.; Eda, G., *Nat. Mater.* **2013,** *12*, 850.
30. Cheng, L.; Huang, W.; Gong, Q.; Liu, C.; Liu, Z.; Li, Y.; Dai, H., *Angew. Chem. Int. Ed.* **2014,** *53*, 7860.
31. Wirth, S.; Harnisch, F.; Weinmann, M.; Schröder, U., *Appl. Catal., B* **2012,** *126*, 225.
32. Hunt, S. T.; Nimmanwudipong, T.; Román-Leshkov, Y., *Angew. Chem. Int. Ed.* **2014,** *53*, 5131.
33. McEnaney, J. M.; Crompton, J. C.; Callejas, J. F.; Popczun, E. J.; Read, C. G.; Lewis, N. S.; Schaak, R. E., *Chem. Commun.* **2014,** *50*, 11026.
34. Xing, Z.; Liu, Q.; Asiri, A. M.; Sun, X., *ACS Catal.* **2014,** *5*, 145.
35. Woods, H.; Wawner, F.; Fox, B. G., *Science* **1966,** *151*, 75.
36. Hayami, W.; Momozawa, A.; Otani, S., *Inorg. Chem.* **2013,** *52*, 7573.
37. Blöchl, P. E., *Physical review B* **1994,** *50*, 17953.
38. Kresse, G.; Joubert, D., *Physical Review B* **1999,** *59*, 1758.
39. Kresse, G.; Furthmüller, J., *Physical review B* **1996,** *54*, 11169.
40. Perdew, J. P.; Burke, K.; Ernzerhof, M., *Phys. Rev. Lett.* **1996,** *77*, 3865.
41. Hammer, B.; Hansen, L. B.; Nørskov, J. K., *Physical Review B* **1999,** *59*, 7413.
42. Skffllason, E.; Tripkovic, V.; Björçrketun, M., *J. Phys. Chem. C* **2010,** *114*, 18182.
43. Tang, Q.; Jiang, D.-e., *ACS Catal.* **2016,** *6*, 4953.
44. Atkins, P. W., *Physical chemistry 3rd ed.* Freeman and Company: New York: 1985.
45. Rudy, E.; Benesovsky, F.; Toth, L., *Z. METALLKD.* **1963,** *54*, 345.
46. Shein, I.; Shein, K.; Ivanovskii, A., *Physica B Condens Matter* **2007,** *387*, 184.
47. Wan, C.; Regmi, Y. N.; Leonard, B. M., *Angew. Chem. Int. Ed.* **2014,** *53*, 6407.
48. Xu, T. T.; Zheng, J. G.; Wu, N.; Nicholls, A. W.; Roth, J. R.; Dikin, D. A.; Ruoff, R. S., *Nano Lett.* **2004,** *4*, 963.
49. Guo, C.; Yin, S.; Yan, M.; Kobayashi, M.; Kakihana, M.; Sato, T., *Inorg. Chem.* **2012,** *51*, 4763.
50. Feng, B.; Zhang, J.; Zhong, Q.; Li, W.; Li, S.; Li, H.; Cheng, P.; Meng, S.; Chen, L.; Wu, K., *Nat Chem* **2016,** *8*, 563.
51. Ospina, R.; Castillo, H.; Benavides, V.; Restrepo, E.; Arango, Y.; Arias, D.; Devia, A., *Vacuum* **2006,** *81*, 373.
52. Benck, J. D.; Chen, Z.; Kuritzky, L. Y.; Forman, A. J.; Jaramillo, T. F., *ACS Catal.* **2012,** *2*, 1916.
53. Wang, X. D.; Xu, Y. F.; Rao, H. S.; Xu, W. J.; Chen, H. Y.; Zhang, W. X.; Kuang, D. B.; Su, C. Y., *Energy Environ. Sci.* **2016,** *9*, 1468.
54. Kibsgaard, J.; Tsai, C.; Chan, K.; Benck, J. D.; Nørskov, J. K.; Abild-Pedersen, F.; Jaramillo, T. F., *Energy Environ. Sci.* **2015,** *8*, 3022.

55. Li, Y.; Wang, H.; Xie, L.; Liang, Y.; Hong, G.; Dai, H., *J. Am. Chem. Soc.* **2011,** *133*, 7296.
56. Tang, Y. J.; Gao, M. R.; Liu, C. H.; Li, S. L.; Jiang, H. L.; Lan, Y. Q.; Han, M.; Yu, S. H., *Angew. Chem. Int. Ed.* **2015,** *54*, 12928.
57. Chung, D. Y.; Park, S. K.; Chung, Y. H.; Yu, S. H.; Lim, D. H.; Jung, N.; Ham, H. C.; Park, H. Y.; Piao, Y.; Yoo, S. J., *Nanoscale* **2014,** *6*, 2131.
58. Fan, M.; Chen, H.; Wu, Y.; Feng, L.-L.; Liu, Y.; Li, G.-D.; Zou, X., *J. Mater. Chem. A* **2015,** *3*, 16320.
59. Gao, D.; Xia, B.; Wang, Y.; Xiao, W.; Xi, P.; Xue, D.; Ding, J., *Small* **2018,** *14*, 1704150.
60. Faber, M. S.; Dziedzic, R.; Lukowski, M. A.; Kaiser, N. S.; Ding, Q.; Jin, S., *J. Am. Chem. Soc.* **2014,** *136*, 10053.
61. Ji, X.; Liu, B.; Ren, X.; Shi, X.; Asiri, A. M.; Sun, X., *ACS Sustainable Chemistry & Engineering* **2018,** *6*, 4499.
62. Wang, X.; Zheng, B.; Yu, B.; Wang, B.; Hou, W.; Zhang, W.; Chen, Y., *J. Mater. Chem. A* **2018,** *6*, 7842.
63. Tian, J.; Liu, Q.; Asiri, A. M.; Sun, X., *J. Am. Chem. Soc.* **2014,** *136*, 7587.
64. Liu, Y.; Liang, C.; Wu, J.; Sharifi, T.; Xu, H.; Nakanishi, Y.; Yang, Y.; Woellne, C. F.; Aliyan, A.; Martí, A. A., *Advanced Materials Interfaces* **2018,** *5*, 1700895.
65. Xiao, P.; Sk, M. A.; Thia, L.; Ge, X.; Lim, R. J.; Wang, J.-Y.; Lim, K. H.; Wang, X., *Energy Environ. Sci.* **2014,** *7*, 2624.
66. Zheng, Y.; Jiao, Y.; Jaroniec, M.; Qiao, S. Z., *Angew. Chem. Int. Ed.* **2015,** *54*, 52.
67. Skúlason, E.; Tripkovic, V.; Björketun, M. E.; Gudmundsdottir, S.; Karlberg, G.; Rossmeisl, J.; Bligaard, T.; Jónsson, H.; Nørskov, J. K., *The Journal of Physical Chemistry C* **2010,** *114*, 18182.

Chapter 5

Synthesis of a Highly active and Efficient HER electrocatalyst by Solid Solution of AlB_2-type Chromium-Molybdenum Diborides

5.1. Introduction

Hydrogen is considered as one of the most promising energy carrier because of its clean, renewable and abundant nature. [1-3] Among various methods to produce hydrogen, electrochemical water splitting through hydrogen evolution reaction (HER) is highly attractive since it is efficient, sustainable and environmentally friendly. [4-5] In water electrolysis, to efficiently attain hydrogen and reduce overpotential, electrocatalysts play vital roles. Up to date, Pt-group noble metals which have extremely low overpotential present the best HER electrocatalytic activity. Unfortunately, their low abundance and high price limit their large-scale application. [6-8] Thus, developing earth-abundant and high HER performance electrocatalysts are important and inevitable topic. [9-10]

In the past few years, non-noble metal electrocatalysts including sulfides[11-13], nitrides[14-15], phosphide[16-19], carbides[20-22], selenides[23-25], and metal alloys[26-27] have shown remarkable HER activity.

Among these materials, especially, transition metal borides (TMBs) such as Mo-B (bulk, nanoscale)[28-32], MoAlB (bulk)[33], Co-B (amorphous)[34-36], Ni-B (amorphous, nanoscale)[37-38], Co-Ni-B (amorphous)[39] , FeB_2 (nanoscale)[40] and VB_2 (nanoscale)[41] are highly attractive as promising candidate of HER electrocatalysts due to their abundance and cheap price and their outstanding HER activity and stability both in acidic and alkaline solution. In the

amorphous TMBs, boron is considered as an electron donor to provide electron to transition metal. Thus, the electron rich TMBs can be a good HER catalyst. [34-36] There some studies about relationship of crystal structure and catalytic activity and people experimentally and theoretically find that borides containing the flat boron (graphene-like) layers such as α-MoB_2, FeB_2 and VB_2 have the highest HER performance.

Chromium is in the same group of the periodic table with molybdenum and tungsten and so it has a similar structural electronic property with molybdenum and tungsten. However, there are few studies about chromium-based materials for HER electrocatalyst and no chromium-based borides have been researched even it is much more abundant than molybdenum (about two order of magnitude). [42] Lin *et al.* found that Cr played an important role in improving the oxygen evolution reaction (OER) activity and stability by tuning the electronic structure of RuO_2 phase and $Cr_{0.6}Ru_{0.4}O_2$ exhibited highest OER activity. [43]

Thus, it is very valuable to study about chromium-based borides for HER electrocatalyst. Similar to ternary transition metal phosphides, carbides, and nitrides, AlB_2-type ternary transition metal borides would have higher HER activity than their binary phase. [44-46]

Herein, we report the successful synthesis of solid solutions of CrB_2, and $Cr_{1-x}Mo_xB_2$ (x = 0.25, 0.4, 0.5, 0.6, 0.75) for HER electrocatalyst. The ternary Cr-Mo-B phases are synthesized and firstly applied for HER catalysts by solid solution.

5.2. Experimental section

$Cr_{1-x}Mo_xB_2$ (x = 0.25, 0.4, 0.5, 0.6, 0.75), CrB_2 and α-MoB_2

Powders of chromium (Cr), molybdenum (Mo) and boron (B) were weighted in appropriate stoichiometric ratios (total mass 0.3 g) and pressed into pellets. The pellets were arc-melted in a water-cooled copper crucible (first electrode) under argon atmosphere by using a tungsten tip as second electrode. The pellet was arc-melted at 60 A in the first step until homogeneous melting occurred. Then, the current was reduced to 40 A and the melting process was repeated 5 times to ensure homogeneity.

Powder X-ray diffraction (PXRD)

Powder X-ray diffraction patterns of the samples were recorded using a Rigaku Miniflex-600 and operating condition were 40 kV and 15 mA generating Cu K_α radiation (λ=1.5418 Å). The recorded powder X-ray diffractograms were refined by means of the Rietveld method (full-matrix least-squares refinement) as implemented in the FULLPROF program suite.

XPS, SEM and EDX, Mapping

X-ray photoelectron spectroscopy (XPS) was conducted using a Kratos AXIS ULTRA ^{DLD} XPS system equipped with an A1 Kα monochromated X-ray source and a 165 mm mean radius hemispherical electron energy analyzer.

The surface morphology and mapping of the synthesized material were obtained by using scanning electron microscopy (SEM) and energy dispersive X-ray spectroscopy (EDS), on

the ultra-high-resolution low-energy system Nova NanoSEM450 equipped with a 50mm^2 X-Max50 SD EDX detector.

Electrochemical characterization

The electrochemical catalytic activity measurements were performed with VSP electrochemical workstation (Bio-Logic VSP, France) in standard three-electrode system using saturated calomel electrode (SCE) as the reference electrode and graphite rod as the counter electrode in 0.5 M H_2SO_4 electrolyte at room temperature. The working electrodes were prepared as follows: arc-melted samples were put into epoxy glue and dried for 2 days. Top and bottom of the dried samples were ground using grinder (South Bay Technology). Ground samples (disc shape) were attached on copper sheet using conductive silver paste. The exposed surface of copper sheet was covered with epoxy glue.

The polarization curves were collected from linear sweep voltammetry (LSV) within -1.0 to 0.0 V at scan rate 5 mV/s and the electrochemical stability of the catalyst was measured by cyclic voltammetry (CV) at scan rate 100 mV/s for 5000 cycles.

All the potentials were calibrated to the reversible hydrogen electrode (RHE), $E_{RHE} = E_{SCE} + 0.242\ V + 0.059 \times pH$ and an *iR*-drop (iR_Ω) correction was applied.

The electrochemically active surface area of the sample was estimated from CV measurements at various scan rates (40 -200 mV/s). The CV measurements were carried out in the region of 0.05 – 0.15 V vs. RHE. The double layer capacitance was estimated by plotting the ΔJ (J_a-J_c) at 0.1 V vs. RHE against the scan rate.

Electrochemical impedance spectroscopy (EIS) was performed at overpotentials (η = 200 mV) in the frequency range of 500 kHz to 1 Hz under the amplitude of 10 mV.

5.3. Results and discussion

Figure 5.1 presents Rietveld refinement plots of X-ray diffraction data of CrB_2, $Cr_{1-x}Mo_xB_2$ (x = 0.25, 0.4, 0.5, 0.6, 0.75). According to these plots, we can observe all ternary phases are successfully synthesized by solid solution with showing AlB_2-type structure and single phase. The lattice parameters and unit cell volume of all samples are listed in **Table 5.1**. The lattice parameters of CrB_2, *a* = 2.9720 (5) Å and *c* = 3.0532 (7) Å, and $Cr_{0.5}Mo_{0.5}B_2$, *a* = 3.0148 (5) Å and *c* = 3.1210 (6) Å, match remarkably the reported values for CrB_2 (ICSD No. 30416, *a* = 2.97 Å and *c* = 3.07Å) and $Cr_{0.5}Mo_{0.5}B_2$ (ICSD No. 108037, *a* = 3.01 Å and *c* = 3.13Å), respectively. [47-48]

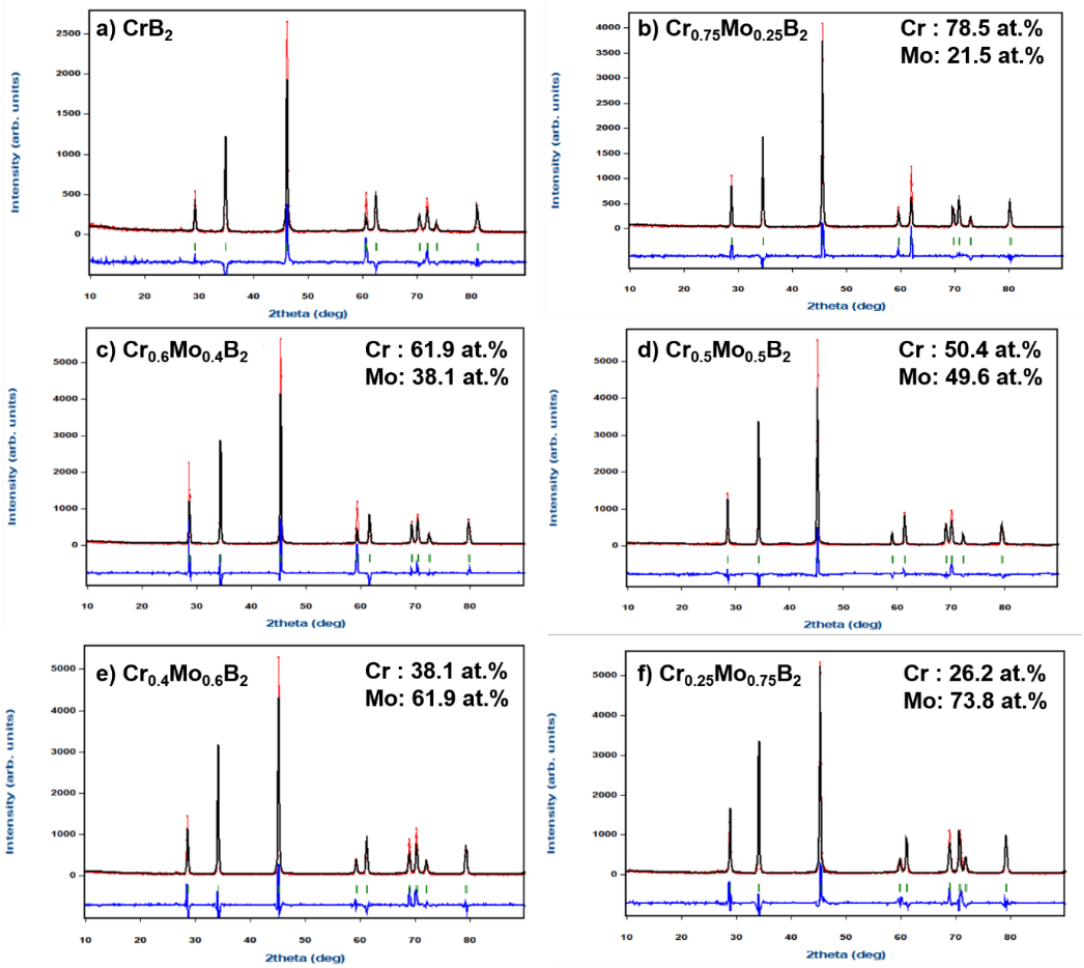

Figure 5.1. Refined powder X-ray diffraction data of CrB_2, $Cr_{1-x}Mo_xB_2$ (x=0.25, 0.4, 0.5, 0.6, 0.75).

Table 5.1. Crystallographic information for the studied chromium-molybdenum boride. Reported lattice parameters are given in square brackets. [47-48]

Phase	**CrB_2**	**$Cr_{0.75}Mo_{0.25}B_2$**
Crystal system	Hexagonal	Hexagonal
Space group	*P6/mmm*	*P6/mmm*
a [Å]	2.9720(5)-[2.97]	2.9931(4)
c [Å]	3.0532(7)-[3.07]	3.0914(7)
V [$Å^3$]	23.356(8)-[23.45]	23.983(7)
Phase	**$Cr_{0.6}Mo_{04}B_2$**	**$Cr_{0.5}Mo_{0.5}B_2$**
Crystal system	Hexagonal	Hexagonal
Space group	*P6/mmm*	*P6/mmm*
a [Å]	3.0078(5)	3.0148(5)-[3.01]
c [Å]	3.1113(6)	3.1210(6)-[3.13]
V [$Å^3$]	24.377(3)	24.567(8)-[24.56]
Phase	**$Cr_{0.4}Mo_{0.6}B_2$**	**$Cr_{0.25}Mo_{0.75}B_2$**
Crystal system	Hexagonal	Hexagonal
Space group	*P6/mmm*	*P6/mmm*
a [Å]	3.0237(9)	3.0324(6)
c [Å]	3.1275(5)	3.1027(7)
V [$Å^3$]	24.763(11)	24.708(8)

Energy dispersive X-ray spectroscopy (EDS) and mapping were conducted to determine the elemental compositions of all samples (**Figure 5.2**). The EDS mappings prove that all elements Cr, Mo and B are uniformly distributed over all materials.

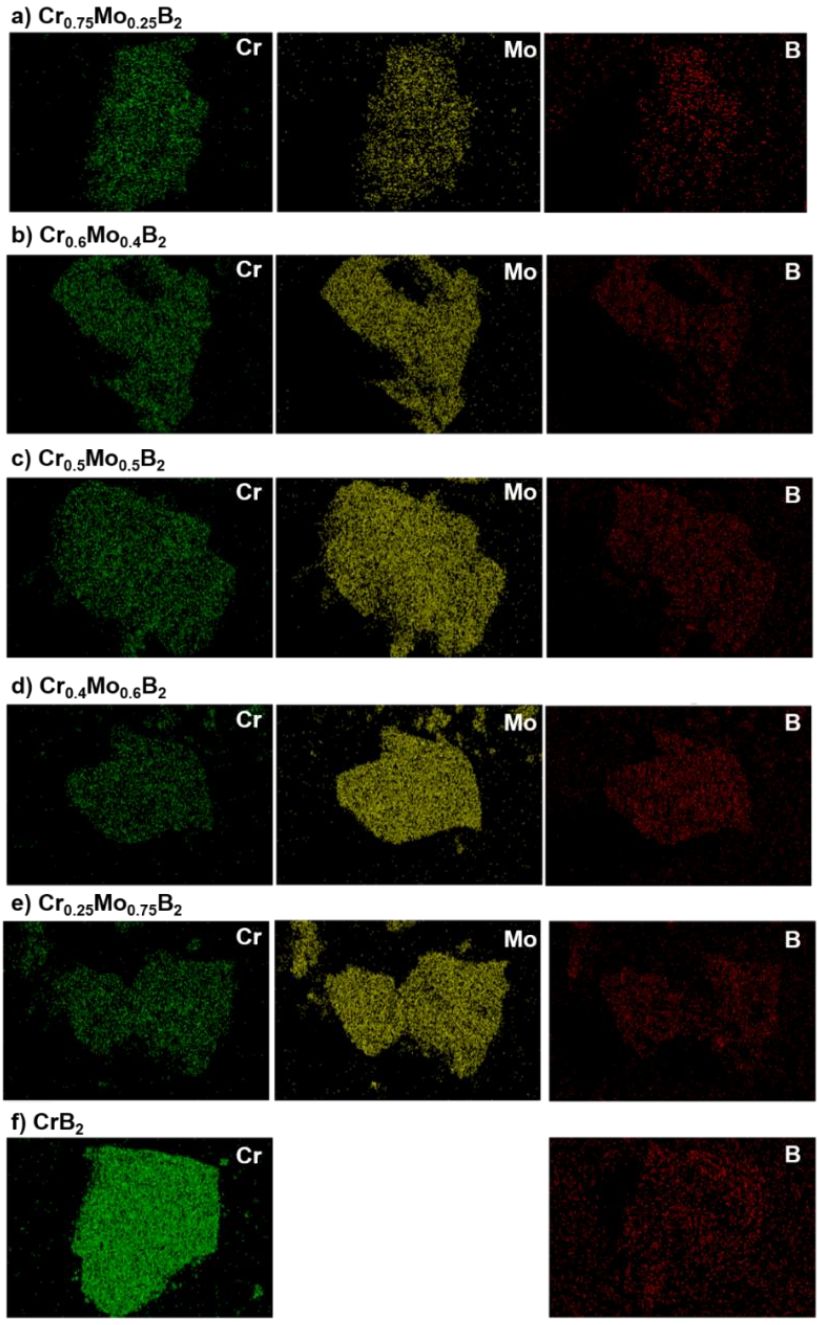

Figure 5.2. EDS mapping of $Cr_{1-x}Mo_xB_2$ (x = 0.25, 0.4, 0.5, 0.6, 0.75) and CrB_2.

Figure 5.3 shows SEM morphology of the ground $Cr_{0.4}Mo_{0.6}B_2$ electrode surface and exhibits heterogeneous particle size distribution in micrometer range. It is well accordance with our previous report of Mo-W-B HER catalyst. [49]

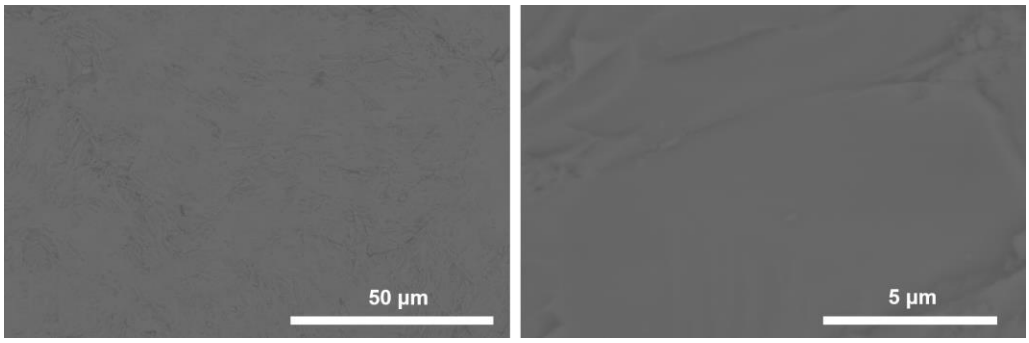

Figure 5.3. SEM morphologies of $Cr_{0.4}Mo_{0.6}B_2$ electrode surface.

According to Vegard's law, the increase of lattice parameter (*a*) with increasing molybdenum content was expected, because slightly larger molybdenum increasingly substitutes chromium in $Cr_{1-x}Mo_xB_2$ series, and a Vegard-like behavior was observed (**Figure 5.4e**). Unlike the lattice parameter (*a*), the lattice parameter (*c*) and unit cell volume did not follow Vegard's law (**Figure 5.4a-d**). The lattice parameter (*c*) and unit cell volume increased until 60 at.% of molybdenum and then decreased. In our previous work about Mo-W-B HER catalyst, this behavior was not observed and ternary phases had similar lattice parameters with binary phase because molybdenum and tungsten had similar atomic radii. [49]

Figure 5.4a-d shows that the lattice parameter (*c*) and overpotential at 10 mA/cm^2 and 150 mA/cm^2. Interestingly, the trend of lattice parameter (*c*) and unit cell volume was

corresponded with the trend of overpotential and $Cr_{0.4}Mo_{0.6}B_2$ has highest *c* value and smallest overpotential.

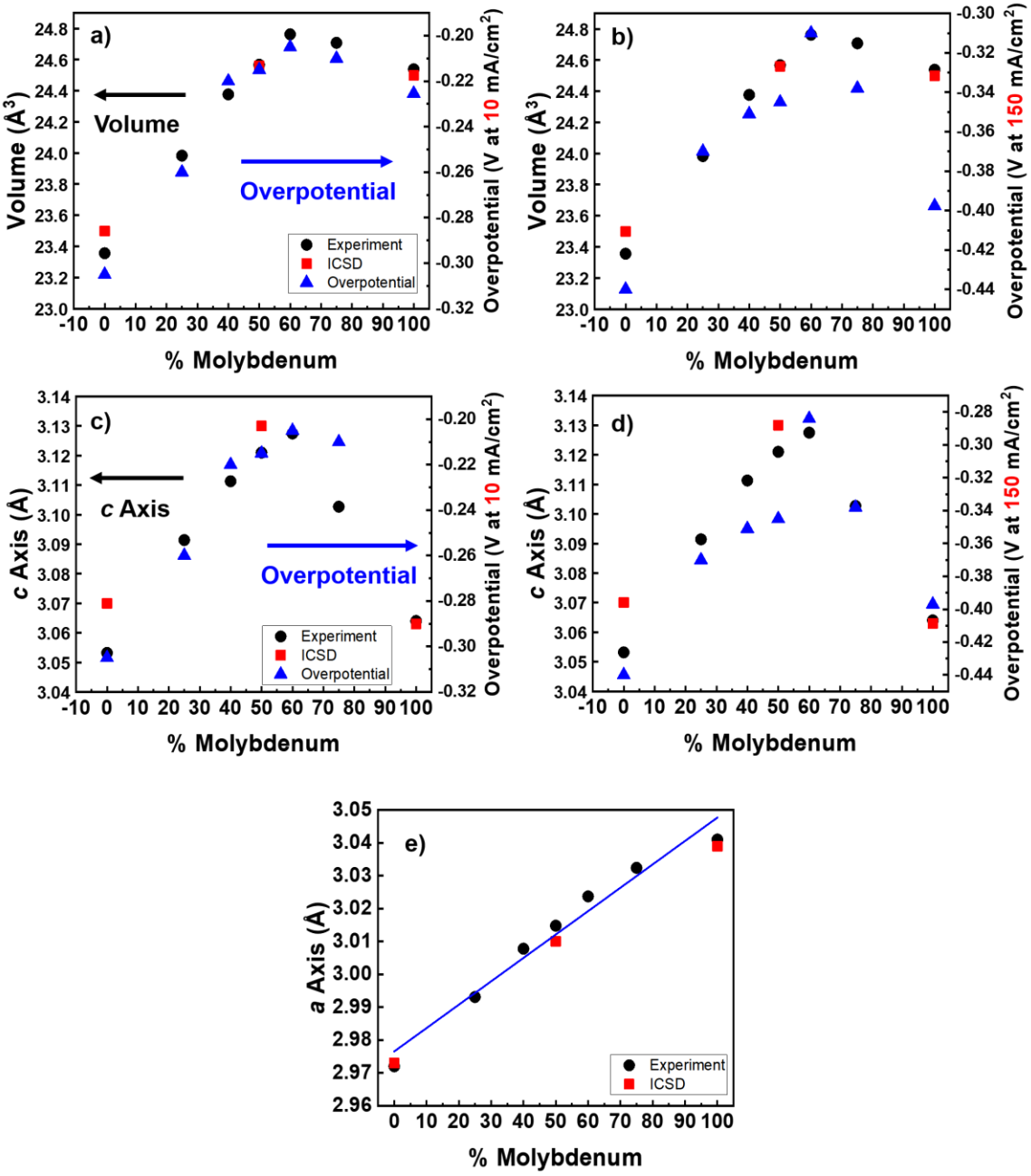

Figure 5.4. The unit cell volume and overpotential a) at 10 mA/cm^2 and b) at 150 mA/cm^2, and the lattice parameter *c* and overpotential c) at 10 mA/cm^2 d) at 150 mA/cm^2, and e) The lattice parameter *a* with molybdenum content.

To analyze the surface chemical composition and electronic state of CrB_2, $Cr_{1-x}Mo_xB_2$ (x = 0.25, 0.4, 0.5, 0.6, 0.75), X-ray photoelectron spectroscopy (XPS) was performed (**Figure 5.5**). **Figure 5.5** displays chromium has three different oxidation states (Cr^0, Cr^{3+} and Cr^{6+}) and indicate four oxidation states of molybdenum (Mo^0, Mo^{3+}, Mo^{4+}, and Mo^{6+}) and two for boron (B^0 and B^{3+}). Oxygen peaks usually are found in most materials due to the surface oxidation of air exposure of samples. [28, 31, 50-52]

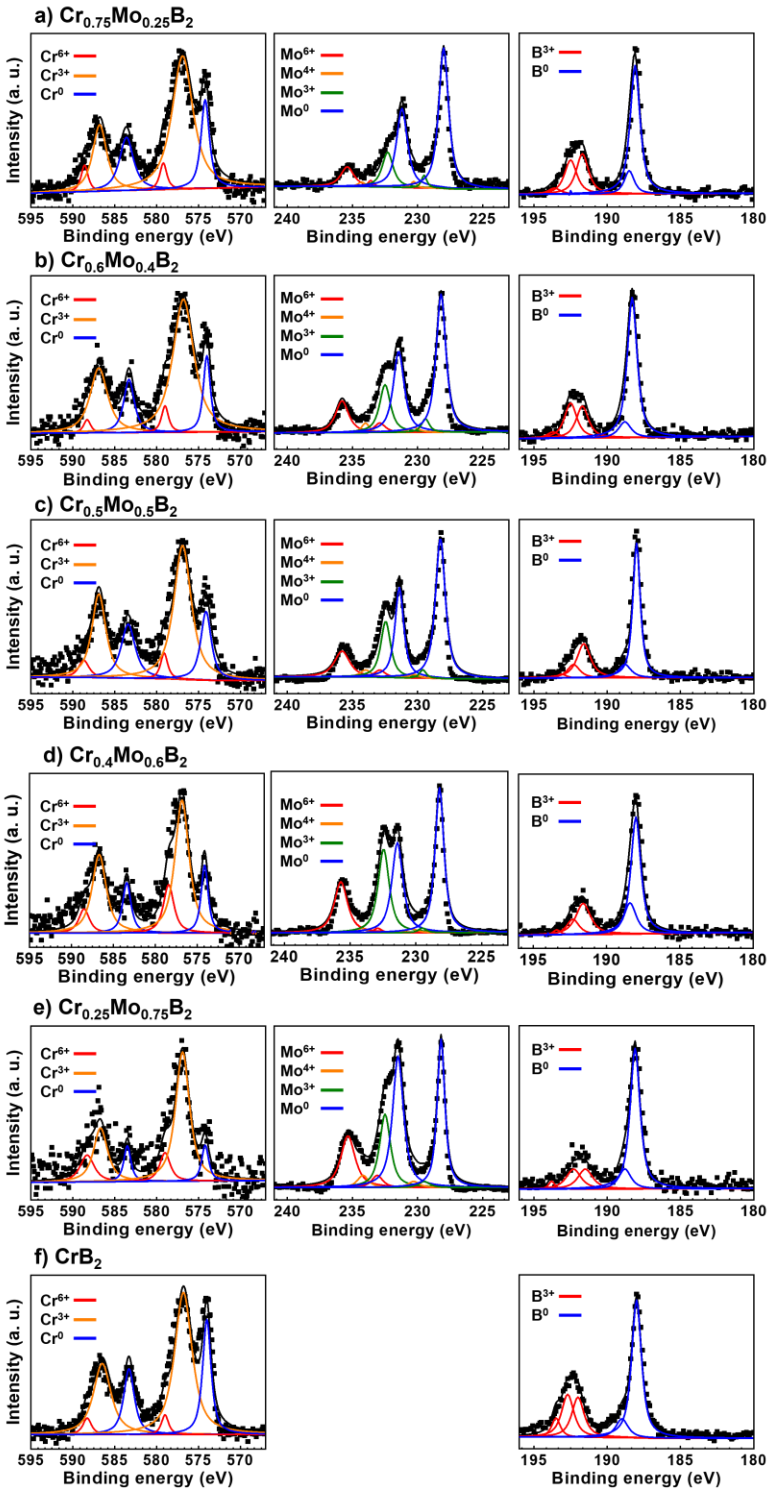

Figure 5.5. XPS spectra of $Cr_{1-x}Mo_xB_2$ (x = 0.25, 0.4, 0.5, 0.6, 0.75) and CrB_2. Experimental data (■), fitting peaks (black line).

Table 5.2. XPS parameters (peak position and full width at half maximum (FWHM)) for Cr 2p, Mo 3d and B 1s of $Cr_{0.4}Mo_{0.6}B_4$ and CrB_2.[28, 53-57]

Phase	Species	Peak position (eV)	FWHM (eV)
$Cr_{0.4}Mo_{0.6}B_2$	Cr^0	574.1, 583.4	1, 1.2
	Cr^{3+}	576.8, 586.7	2, 2
	Cr^{6+}	578.4, 588.5	1.5, 1.5
	Mo^0	228.2, 231.4	0.8, 1
	Mo^{3+}	229.5, 232.45	0.7, 1
	Mo^{4+}	230.3, 234.1	1, 0.7
	Mo^{6+}	232.9, 235.7	0.7, 1.2
	B^0	188.3, 187.9	0.8, 1
	B^{3+}	191.5, 192.2, 193.3	1.2, 1, 0.6
Phase	**Species**	**Peak position (eV)**	**FWHM (eV)**
CrB_2	Cr^0	573.9, 583.2	1.2, 1.5
	Cr^{3+}	576.7, 586.4	2.5, 2.5
	Cr^{6+}	579.9, 588.2	1, 1.2
	B^0	188.0, 189.0	0.8, 1
	B^{3+}	192.0, 192.7, 193.5	1, 1, 0.7

The electrochemical HER activity of $Cr_{1-x}Mo_xB_2$ (x = 0.25, 0.4, 0.5, 0.6, 0.75), CrB_2 and α-MoB_2 have been measured using the standard three electrodes system in acid (0.5 M H_2SO_4) electrolyte at a scan rate of 5 mV/s with IR drop compensation (**Figure 5.6**). In the previous paper, we demonstrated the importance of working electrode preparation method and drop-casting was not appropriate for the bulk sample and denser electrode could lead to better HER performance. Thus, the arc-melted samples were ground to disc shape and attached on the copper sheet. [49]

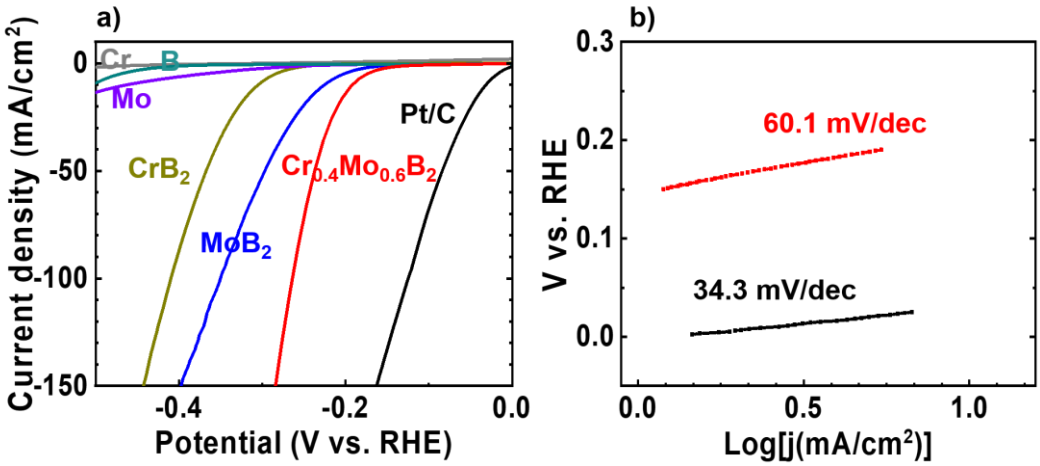

Figure 5.6. a) Linear sweep polarization curves in 0.5 M H_2SO_4, and b) The corresponding Tafel slopes. The current density is normalized with the electrode's geometric surface area.

The HER activity of Cr-Mo-B systems was firstly examined. CrB_2 and α-MoB_2 have the same crystal structure (AlB_2-type) but α-MoB_2 has higher HER activity than CrB_2 because molybdenum is more active than chromium. Upon increasing the amount of molybdenum, the HER activity greatly increases for $Cr_{0.75}Mo_{0.25}B_2$, then it further increases for $Cr_{0.5}Mo_{0.5}B_2$. $Cr_{0.5}Mo_{0.5}B_2$ and $Cr_{0.6}Mo_{0.4}B_2$ have similar activities and their activities are higher than α-MoB_2 Adding more molybdenum improved the HER activity

and $Cr_{0.4}Mo_{0.6}B_2$ shows best HER activity in Cr-Mo-B system. After 60 at.% of molybdenum, the HER activity was decreased and the HER activity of $Cr_{0.25}Mo_{0.75}B_2$ is similar to $Cr_{0.5}Mo_{0.5}B_2$ and it is close to α-MoB_2 (**Figure 5..7**).

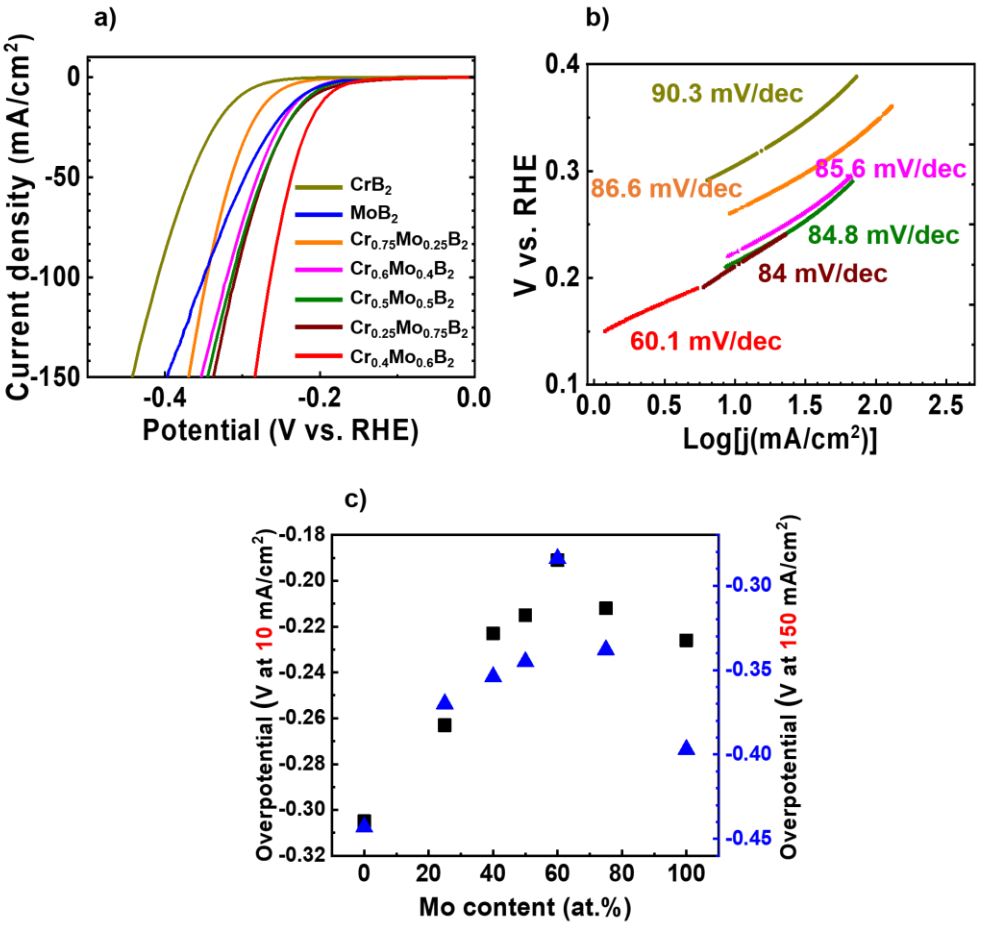

Figure 5.7. a) Linear sweep polarization curves of $Cr_{1-x}Mo_xB_2$ (x = 0.25, 0.4, 0.5, 0.6, 0.75), CrB_2 and MoB_2 obtained in 0.5 M H_2SO_4, b) The corresponding Tafel slopes, and c) The overpotential of $Cr_{1-x}Mo_xB_2$ (x = 0.25, 0.4, 0.5, 0.6, 0.75), CrB_2 and MoB_2 at current density of 10 and 150 mA/cm^2.

Similar trend was found in recently reported studies on borides and oxides system.[43, 58] In $(Co_{1-x}Fe_x)_2B$ system, OER activity was improved by incorporation of Fe and the overpotentials of $(Co_{1-x}Fe_x)_2B$ decreased $x \leq 0.3$, then increased and the OER activities $x > 0.3$ were similar to Co_2B in alkaline solution.[58] In addition, $Cr_{0.6}Ru_{0.4}O_2$ derived from metal-organic framework exhibited much improved OER activity than RuO_2 in acid electrolyte. [43]

These results suggest that addition of element such as Fe and Co could increase HER activity by tuning electronic structure and reducing gibbs energy. Thus, the ternary phase would have higher activity than their binary phase. [43, 58]

Interestingly, at high current density (above 500 mA/cm^2), the $Cr_{0.4}Mo_{0.6}B_2$ outperforms Pt/C in acid solution. For example, $Cr_{0.4}Mo_{0.6}B_2$ requires the overpotential of 400 mV compared to 500 mV for Pt/C at a current density of 500 mA/cm^2 in the acid electrolyte (**Figure 5.8**).

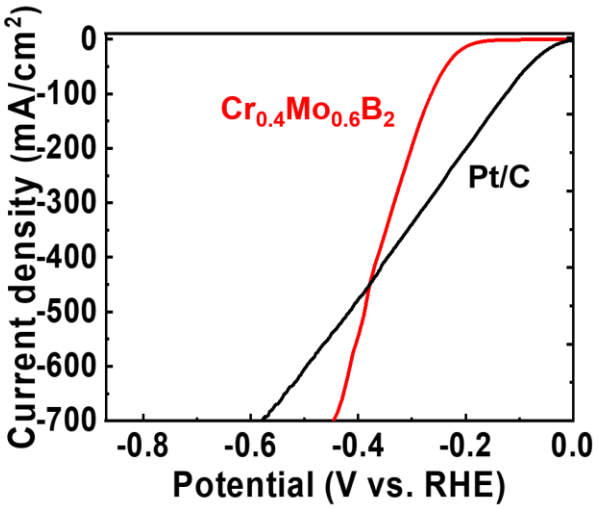

Figure 5.8. Linear sweep polarization curves of $Cr_{0.4}Mo_{0.6}B_2$ in 0.5 M H_2SO_4.

The HER catalytic mechanism is usually revealed by Tafel plot, η versus log(j). Typically, there are three classical reactions which can be the rate-determining steps, the Volmer reaction (electrochemical hydrogen ion adsorption, Tafel slope of ~120 mV/dec.), the Heyrovsky reaction (electrochemical desorption, Tafel slope of ~40 mV/dec.) and the Tafel reaction (chemical desorption, Tafel slope of ~30 mV/dec.). The first step of HER is Volmer reaction. Subsequently, there are two different possible H_2 formation pathway, Heyrovsky or Tafel reaction. [59-61] The calculated Tafel slopes of all samples are shown in **Figure 5.6b and 5.7b**. All the Tafel slope range is from 60.1 to 90.3 mV/dec., representing that these values do not match any theoretical Tafel slope and it is difficult to determine the rate-determining step (RDS) using Tafel analysis because of reaction complexity of bulk HER catalyst. However, $Cr_{0.4}Mo_{0.6}B_2$ exhibits the lowest Tafel slope, demonstrating much faster and efficient process of HER than for binary and all ternary phases. [16]

The electrochemically active surface area (ECSA) of six different metal borides (CrB_2, $Cr_{1-x}Mo_xB_2$ (x = 0.25, 0.4, 0.5, 0.6, 0.75)) was estimated by measurement of double layer capacitance (C_{dl}) through cyclic voltammetry (CV) at various scan rate between 0.05-0.15 V vs. reversible hydrogen electrode (RHE) (**Figure 5.9**).[62-63] In accordance with the HER activity result, $Cr_{0.4}Mo_{0.6}B_2$ has the highest ECSA value, indicating the most number of active sites. The highest HER activity of $Cr_{0.4}Mo_{0.6}B_2$ can be confirmed by electrochemical impedance spectroscopy (EIS) measurement. $Cr_{0.4}Mo_{0.6}B_2$ has the smallest electron transfer resistance and the trend of EIS result is in good conformity with the HER activity trend (**Figure 5.10**).

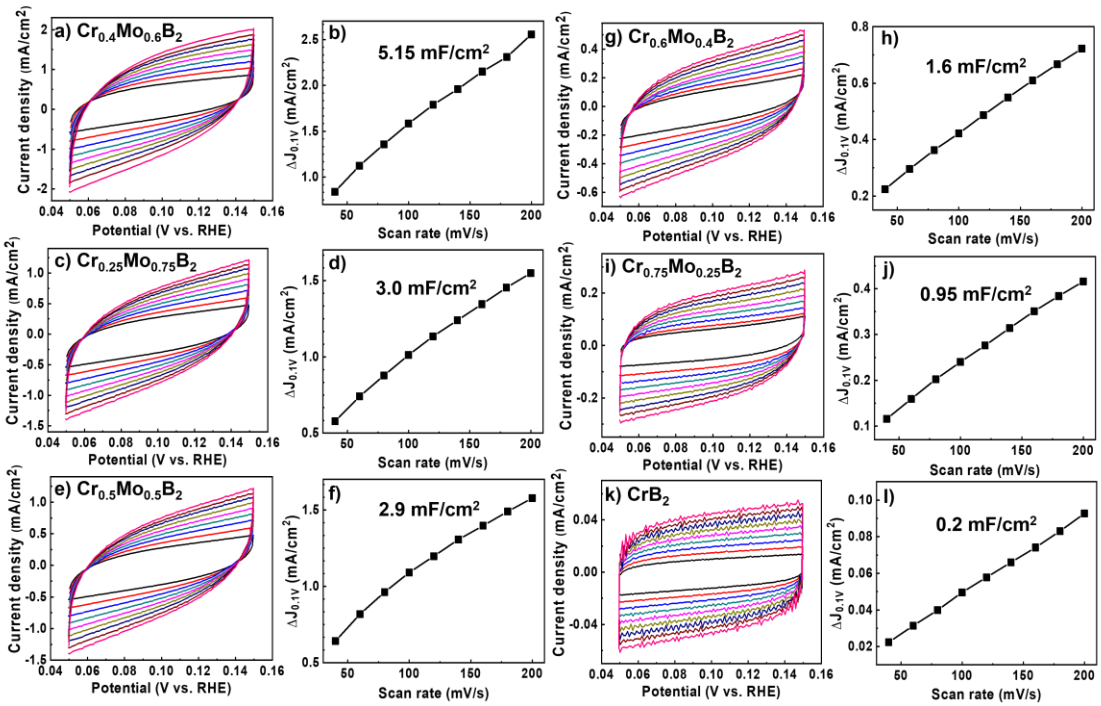

Figure 5.9. a), c), e), g), i) and k) Cyclic Voltammetry curves of $Cr_{0.4}Mo_{0.6}B_2$, $Cr_{0.25}Mo_{0.75}B_2$, $Cr_{0.5}Mo_{0.5}B_2$, $Cr_{0.6}Mo_{0.4}B_2$, $Cr_{0.75}Mo_{0.25}B_2$ and CrB_2. b), d), f), h), j) and l) The difference current density ΔJ (J_a-J_c) at 0.1 V vs. RHE plotted against the scan rate is fitted to a linear regression to estimate C_{dl}.

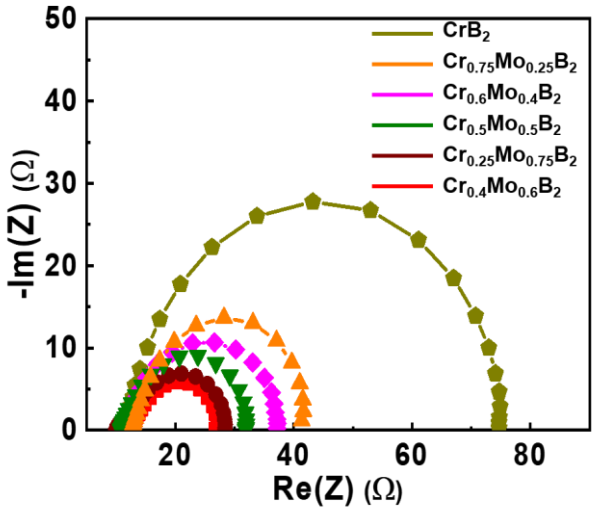

Figure 5.10. Electrochemical impedance spectroscopy (EIS) Nyquist plots of $Cr_{1-x}Mo_xB_2$ (x = 0.25, 0.4, 0.5, 0.6, 0.75) and CrB_2.

The long-term durability test was evaluated by potential cycling for 5000 cycles in acid electrolyte. As shown in **Figure 5.11a**, $Cr_{0.4}Mo_{0.6}B_2$ depicts no appreciable activity loss after 5000 potential cycles. In addition, the chronoamperometry curve for $Cr_{0.4}Mo_{0.6}B_2$ indicates that the current density of $Cr_{0.4}Mo_{0.6}B_2$ is maintained a constant value with a negligible loss, revealing $Cr_{0.4}Mo_{0.6}B_2$ has superior long-term electrochemical stability (**Figure 5.11b**).

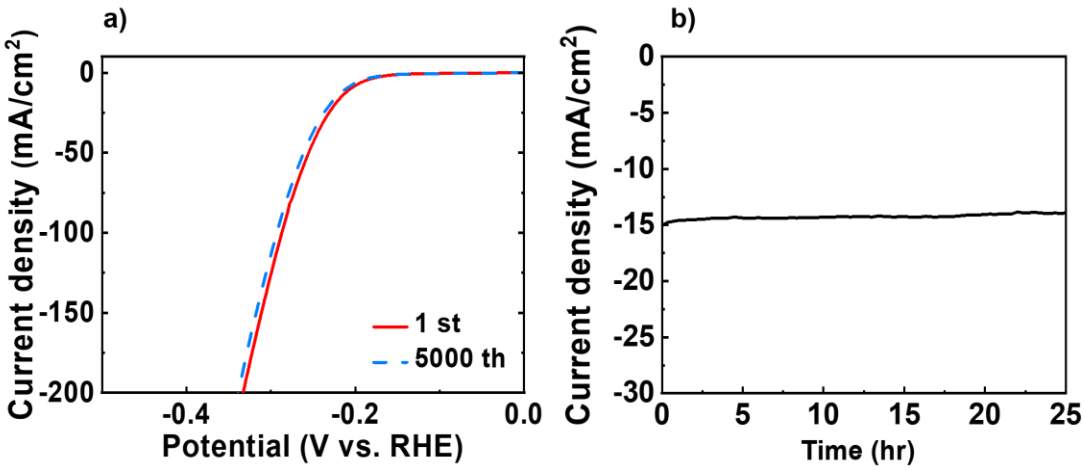

Figure 5.11. a) HER stability measurement of $Cr_{0.4}Mo_{0.6}B_2$ before and after 5000 cycles with scan rate of 100 mV/s in 0.5 M H_2SO_4, b) Chronoamperometry curve of $Cr_{0.4}Mo_{0.6}B_2$ for 25 hr in 0.5 M H_2SO_4.

5.4. Conclusions

In summary, single-phase bulk solid solution $Cr_{1-x}Mo_xB_2$ (x = 0, 0.25, 0.4, 0.5, 0.6, 0.75, AlB_2-type structure) has been firstly successfully synthesized by arc melting. We found that the ternary phase has higher HER activity than binary phase. Among $Cr_{1-x}Mo_xB_2$ electrochemical catalyst, $Cr_{0.4}Mo_{0.6}B_2$ exhibits highest HER catalytic activity and has even higher HER activity than Pt/C at high current density in acid solution. $Cr_{0.4}Mo_{0.6}B_2$ has excellent long-term stability and there is no significant HER activity loss after 5000 cycles and 25 hr.

References

1. Turner, J. A., *Science* **2004,** *305*, 972.
2. Lewis, N. S.; Nocera, D. G., *Prog. Nat. Acad. Sci.* **2006,** *103*, 15729.
3. Dresselhaus, M.; Thomas, I., *Nature* **2001,** *414*, 332.
4. Wang, J.; Cui, W.; Liu, Q.; Xing, Z.; Asiri, A. M.; Sun, X., *Adv. Mater.* **2016,** *28*, 215.
5. Laursen, A. B.; Kegnæs, S.; Dahl, S.; Chorkendorff, I., *Energy Environ. Sci.* **2012,** *5*, 5577.
6. Faber, M. S.; Jin, S., *Energy Environ. Sci.* **2014,** *7*, 3519.
7. Jiao, Y.; Zheng, Y.; Jaroniec, M.; Qiao, S. Z., *Chem. Soc. Rev.* **2015,** *44*, 2060.
8. Morales-Guio, C. G.; Stern, L. A.; Hu, X., *Chem. Soc. Rev.* **2014,** *43*, 6555.
9. Shi, Y.; Zhang, B., *Chem. Soc. Rev.* **2016,** *45*, 1529.
10. Lu, Q.; Yu, Y.; Ma, Q.; Chen, B.; Zhang, H., *Adv. Mater.* **2016,** *28*, 1917.
11. Jaramillo, T. F.; Jørgensen, K. P.; Bonde, J.; Nielsen, J. H.; Horch, S.; Chorkendorff, I., *Science* **2007,** *317*, 100.
12. Wang, D.-Y.; Gong, M.; Chou, H. L.; Pan, C.-J.; Chen, H. A.; Wu, Y.; Lin, M. C.; Guan, M.; Yang, J.; Chen, C. W., *J. Am. Chem. Soc.* **2015,** *137*, 1587.
13. Staszak-Jirkovský, J.; Malliakas, C. D.; Lopes, P. P.; Danilovic, N.; Kota, S. S.; Chang, K.-C.; Genorio, B.; Strmcnik, D.; Stamenkovic, V. R.; Kanatzidis, M. G., *Nat. Mater.* **2016,** *15*, 197.
14. Chen, W.-F.; Muckerman, J. T.; Fujita, E., *Chemical Communications* **2013,** *49*, 8896.
15. Chen, W. F.; Sasaki, K.; Ma, C.; Frenkel, A. I.; Marinkovic, N.; Muckerman, J. T.; Zhu, Y.; Adzic, R. R., *Angew. Chem. Int. Ed.* **2012,** *51*, 6131.
16. Xiao, X.; Tao, L.; Li, M.; Lv, X.; Huang, D.; Jiang, X.; Pan, H.; Wang, M.; Shen, Y., *Chem. Sci.* **2018,** *9*, 1970.
17. Zhang, R.; Wang, X.; Yu, S.; Wen, T.; Zhu, X.; Yang, F.; Sun, X.; Wang, X.; Hu, W., *Adv. Mater.* **2017,** *29*, 1605502.
18. Callejas, J. F.; McEnaney, J. M.; Read, C. G.; Crompton, J. C.; Biacchi, A. J.; Popczun, E. J.; Gordon, T. R.; Lewis, N. S.; Schaak, R. E., *ACS nano* **2014,** *8*, 11101.
19. Popczun, E. J.; McKone, J. R.; Read, C. G.; Biacchi, A. J.; Wiltrout, A. M.; Lewis, N. S.; Schaak, R. E., *J. Am. Chem. Soc.* **2013,** *135*, 9267.
20. Michalsky, R.; Zhang, Y. J.; Peterson, A. A., *ACS Catal.* **2014,** *4*, 1274.
21. Liao, L.; Wang, S.; Xiao, J.; Bian, X.; Zhang, Y.; Scanlon, M. D.; Hu, X.; Tang, Y.; Liu, B.; Girault, H. H., *Energy Environ. Sci.* **2014,** *7*, 387.
22. Chen, W.-F.; Wang, C.-H.; Sasaki, K.; Marinkovic, N.; Xu, W.; Muckerman, J.; Zhu, Y.; Adzic, R., *Energy Environ. Sci.* **2013,** *6*, 943.
23. Kong, D.; Wang, H.; Cha, J. J.; Pasta, M.; Koski, K. J.; Yao, J.; Cui, Y., *Nano Lett.* **2013,** *13*, 1341.
24. Xu, K.; Wang, F.; Wang, Z.; Zhan, X.; Wang, Q.; Cheng, Z.; Safdar, M.; He, J., *ACS nano* **2014,** *8*, 8468.
25. Wang, X.; Chen, Y.; Zheng, B.; Qi, F.; He, J.; Li, P.; Zhang, W., *Electrochim. Acta* **2016,** *222*, 1293.

26. Fosdick, S. E.; Berglund, S. P.; Mullins, C. B.; Crooks, R. M., *ACS Catal.* **2014,** *4*, 1332.
27. Lv, H.; Xi, Z.; Chen, Z.; Guo, S.; Yu, Y.; Zhu, W.; Li, Q.; Zhang, X.; Pan, M.; Lu, G., *J. Am. Chem. Soc.* **2015,** *137*, 5859.
28. Vrubel, H.; Hu, X., *Angew. Chem. Int. Ed.* **2012,** *51*, 12703.
29. Park, H.; Encinas, A.; Scheifers, J. P.; Zhang, Y.; Fokwa, B., *Angew. Chem. Int. Ed.* **2017,** *56*, 5575.
30. Park, H.; Zhang, Y.; Scheifers, J. P.; Jothi, P. R.; Encinas, A.; Fokwa, B. P., *J. Am. Chem. Soc.* **2017,** *139*, 12915.
31. Jothi, P. R.; Zhang, Y.; Scheifers, J. P.; Park, H.; Fokwa, B. P., *Sustainable Energy Fuels* **2017,** *1*, 1928.
32. Wang, X.; Tai, G.; Wu, Z.; Hu, T.; Wang, R., *J. Mater. Chem. A* **2017,** *5*, 23471.
33. Alameda, L. T.; Holder, C. F.; Fenton, J. L.; Schaak, R. E., *Chem. Mater.* **2017,** *29*, 8953.
34. Gupta, S.; Patel, N.; Miotello, A.; Kothari, D., *J. Power Sources* **2015,** *279*, 620.
35. Masa, J.; Weide, P.; Peeters, D.; Sinev, I.; Xia, W.; Sun, Z.; Somsen, C.; Muhler, M.; Schuhmann, W., *Adv. Energy Mater.* **2016,** *6*, 1502313.
36. Chen, Z.; Kang, Q.; Cao, G.; Xu, N.; Dai, H.; Wang, P., *Int. J. Hydrogen Energy* **2018,** *43*, 6076.
37. Los, P.; Lasia, A., *J. Electroanal. Chem.* **1992,** *333*, 115.
38. Zeng, M.; Wang, H.; Zhao, C.; Wei, J.; Qi, K.; Wang, W.; Bai, X., *ChemCatChem* **2016,** *8*, 708.
39. Xu, N.; Cao, G.; Chen, Z.; Kang, Q.; Dai, H.; Wang, P., *J. Mater. Chem. A* **2017,** *5*, 12379.
40. Li, H.; Wen, P.; Li, Q.; Dun, C.; Xing, J.; Lu, C.; Adhikari, S.; Jiang, L.; Carroll, D. L.; Geyer, S. M., *Adv. Energy Mater.* **2017,** *7*, 1700513.
41. Jothi, P. R.; Zhang, Y.; Yubuta, K.; Culver, D.; Conley, M. P.; Fokwa, B. P., *ACS Appl. Energy Mater.* **2019,** *2*, 176.
42. Schmuecker, S. M.; Clouser, D.; Kraus, T. J.; Leonard, B. M., *Dalton Transactions* **2017,** *46*, 13524.
43. Lin, Y.; Tian, Z.; Zhang, L.; Ma, J.; Jiang, Z.; Deibert, B. J.; Ge, R.; Chen, L., *Nat. Commun.* **2019,** *10*, 162.
44. Hunt, S. T.; Nimmanwudipong, T.; Román-Leshkov, Y., *Angew. Chem. Int. Ed.* **2014,** *53*, 5131.
45. Cao, B.; Veith, G. M.; Neuefeind, J. C.; Adzic, R. R.; Khalifah, P. G., *J. Am. Chem. Soc.* **2013,** *135*, 19186.
46. Wu, H. B.; Xia, B. Y.; Yu, L.; Yu, X.-Y.; Lou, X. W. D., *Nat. Commun.* **2015,** *6*.
47. Post, B.; Glaser, F. W.; Moskowitz, D., *Acta Metall.* **1954,** *2*, 20.
48. Kuz'ma, Y. B.; Telegus, V.; Kovalyk, D., *Soviet Powder Metallurgy and Metal Ceramics* **1969,** *8*, 403.
49. Park, H.; Zhang, Y.; Lee, E.; Shankhari, P.; Fokwa, B. T. P., *ChemSusChem* **2019,** *12*, 1.
50. Skomski, D.; Tempas, C. D.; Bukowski, G. S.; Smith, K. A.; Tait, S. L., *The Journal of chemical physics* **2015,** *142*, 101913.

51. Choudhary, B.; Paul, D.; Singh, A.; Gupta, T., *Environmental Science and Pollution Research* **2017,** *24*, 16786.
52. Yao, W.; Duan, T.; Li, Y.; Yang, L.; Xie, K., *New J. Chem.* **2015,** *39*, 2956.
53. Wan, C.; Regmi, Y. N.; Leonard, B. M., *Angew. Chem. Int. Ed.* **2014,** *53*, 6407.
54. Xu, T. T.; Zheng, J. G.; Wu, N.; Nicholls, A. W.; Roth, J. R.; Dikin, D. A.; Ruoff, R. S., *Nano Lett.* **2004,** *4*, 963.
55. Feng, B.; Zhang, J.; Zhong, Q.; Li, W.; Li, S.; Li, H.; Cheng, P.; Meng, S.; Chen, L.; Wu, K., *Nat Chem* **2016,** *8*, 563.
56. Guo, C.; Yin, S.; Yan, M.; Kobayashi, M.; Kakihana, M.; Sato, T., *Inorg. Chem.* **2012,** *51*, 4763.
57. Ospina, R.; Castillo, H.; Benavides, V.; Restrepo, E.; Arango, Y.; Arias, D.; Devia, A., *Vacuum* **2006,** *81*, 373.
58. Klemenz, S.; Schuch, J.; Hawel, S.; Zieschang, A. M.; Kaiser, B.; Jaegermann, W.; Albert, B., *ChemSusChem* **2018,** *11*, 3150.
59. Chung, D. Y.; Park, S. K.; Chung, Y. H.; Yu, S. H.; Lim, D. H.; Jung, N.; Ham, H. C.; Park, H. Y.; Piao, Y.; Yoo, S. J., *Nanoscale* **2014,** *6*, 2131.
60. Tang, Y. J.; Gao, M. R.; Liu, C. H.; Li, S. L.; Jiang, H. L.; Lan, Y. Q.; Han, M.; Yu, S. H., *Angew. Chem. Int. Ed.* **2015,** *54*, 12928.
61. Kahyarian, A.; Brown, B.; Nesic, S., *J. Electrochem. Soc.* **2017,** *164*, H365.
62. Benck, J. D.; Chen, Z.; Kuritzky, L. Y.; Forman, A. J.; Jaramillo, T. F., *ACS Catal.* **2012,** *2*, 1916.
63. Lukowski, M. A.; Daniel, A. S.; Meng, F.; Forticaux, A.; Li, L.; Jin, S., *J. Am. Chem. Soc.* **2013,** *135*, 10274.